The Effects of Refraction and Forward Scattering on Exoplanet Transit Transmission Spectroscopy

Amit Misra

A dissertation
submitted in partial fulfillment of the
requirements for the degree of

Doctor of Philosophy

University of Washington

2014

Reading Committee:

Victoria S. Meadows, Chair

Dave Crisp

Rory Barnes

Program Authorized to Offer Degree:
Astronomy

University of Washington

Abstract

The Effects of Refraction and Forward Scattering on Exoplanet Transit Transmission Spectroscopy

Amit Misra

Chair of the Supervisory Committee:
Professor Victoria S. Meadows
Astronomy

Transit transmission spectroscopy may provide the first glimpse at the atmosphere of an Earth-like exoplanet, and therefore the first chance to detect habitability markers and biosignatures, or signs of life. Within the next 10-15 years, the James Webb Space Telescope and large-aperture ground-based telescopes like the European Extremely Large Telescope (E-ELT) will come on line. JWST and E-ELT will have much greater collecting areas than existing space and ground-based telescopes, respectively, and will therefore allow for lower noise levels to be reached in transit transmission observations. With lower noise levels, it could be possible to characterize the atmospheres of Earth-sized, transiting planets orbiting in their star's habitable zones. Additionally, with that same increase in precision, physical effects that could previously be ignored may need to be considered in the near future. In light of this, I propose that refraction and forward scattering need to be considered when modeling transit transmission spectra, especially when comparing models to observations from future telescopes. I present the first model for transmission spectroscopy that includes the physical effects of refraction and forward scattering, and examine the effects of both on in-transit spectra and transit light curves. The model uses a backwards Monte Carlo ray tracing module coupled with an existing radiative transfer model (SMART). I validate the model against observations of the Earth from satellite data and lunar eclipse observations, and against theoretical and empirical estimates of the Venus scattering footprint. I find that refraction can reduce the detectability of spectral absorption features by setting a maximum tangent pressure that can be probed. This effect of refraction is small for planets whose orbital diameter is less than 12 times the diameter of the stellar disk ($R_*/a > 5^\circ$, i.e., close-in planets). However, for Earth-like planets orbiting Sun-like stars, refraction can severely reduce the detectability of biosignatures and habitability markers. Refraction also leads to changes in the transit light curve. I show that the wavelength-dependence of these changes can be used to obtain altitude-dependent spectra of exoplanets. In addition, a detection of refracted light in the out-of-transit light curve would indicate a lack of optically-thick hazes above the 1 mbar pressure level because light is refracted most at pressures greater than 1 mbar. Forward scattering increases the total flux seen in the in-transit spectrum, relative to models that include only extinction from aerosols. This may be an important effect for modeling planets whose orbital diameter is less than $\sim$6 times the diameter of the stellar disk ($R_*/a > 10^\circ$, i.e., very close-in planets), such as hot Jupiters, but will be negligible for potentially habitable planets. Light can also be forward scattered when the planet is out-of-transit, and a detection of out-of-transit scattered light would be strongly suggestive of aerosols in the exoplanet atmosphere. Furthermore, a quantification of out-of-transit scattered light would allow for upper limits to be placed on the scattering asymmetry parameter, which in turn could be used to constrain the aerosol particle size distribution and composition.

The model described above was used to simulate Earth-like planets to identify two signals as potential habitability markers and biosignatures: absorption from O_2 dimer molecules and transient sulfate aerosols. Dimer molecules could be used to estimate atmospheric pressure, which is an important parameter for determining if liquid water could

be present on the surface of an exoplanet, a requirement for habitability. Absorption from dimer molecules is more strongly dependent on density (and therefore pressure) than absorption from non-dimer molecules, and I show that combining absorption strengths from both types of features may allow limits to be placed on the surface or cloud-top pressure. O_2 dimer molecules could also be biosignatures, and I show that O_2 dimer features may be the most detectable O_2 features in transit transmission for Earth-like exoplanets. The second signal I propose as a habitability marker and biosignature is transient sulfate aerosols. On Earth, explosive volcanism injects SO_2 into the stratosphere, where it forms H_2SO_4 aerosols with lifetimes from months to years. The rapid rise and gradual decrease of aerosols could be indicative of a volcanic eruption on an exoplanet. For Earth, volcanism, and more broadly, geological activity, is important for the origin of life and for maintaining habitability. Therefore, the detection of a transient sulfate aerosol signal would suggest a geologically active planet, and increase the likelihood of that planet being habitable. Furthermore, there exist some scenarios in which O_2 and O_3 can build up abiotically if volcanic outgassing rates are much lower than those on the present-day Earth. Therefore, a co-detection of O_2 or O_3 with a transient aerosol signal may aid in resolving the ambiguity between biotic and abiotic O_2 or O_3.

TABLE OF CONTENTS

LIST OF FIGURES

LIST OF TABLES

ACKNOWLEDGMENTS

This work was made possible by many individuals, especially my adviser Vikki Meadows and Dave Crisp, who were the ones who initially helped me select a PhD project. Their ideas and support helped me to get started on exoplanet transit transmission spectroscopy, and without their expertise and advice none of this would have been possible. Their insistence on validating models not only helped me to develop more accurate models, it also indirectly led to the inclusion of refraction in the model and the chapters on dimer absorption features and exo-volcanism.

I'd also like to thank Shawn-Domagal Goldman for working with me during my first year as a graduate student. His patience, knowledge, and willingness to teach made the transition to exoplanet science for me much easier.

Lastly, I'd like to thank my parents and other family members, who instilled a culture of education in me from the very beginning.

DEDICATION

To Marinda, Luke, and baby Jacy

Chapter 1

INTRODUCTION

The discovery and characterization of exoplanets has been one of the most exciting and rapidly advancing scientific endeavors over the past two decades. Since the discovery of the first exoplanets in the early 1990's (Wolszczan and Frail, 1992; Mayor and Queloz, 1995), over 1500 confirmed planets have been discovered along with 3,000 planet candidates[1]. The first planets discovered were hot, close-in giant planets, as these planets produced the largest observational signal for detection. As technology and observational techniques have improved, it is now possible to discover cooler and smaller planets. Recently Earth-sized planets have been discovered that are in their host star's habitable zone (Anglada-Escudé *et al.*, 2012; Borucki *et al.*, 2013; Quintana *et al.*, 2014), suggesting that they could have liquid water on their surface, and perhaps life.

The discovery of exoplanets has been closely followed by the characterization of exoplanet atmospheres. This has typically been done for transiting planets in primary eclipse (transit) or secondary eclipse. In primary eclipse, the planet is directly between the telescope and the planet's host star. During the eclipse, some of the star's light traverses the limb (or edge) of the exoplanet atmosphere, and can be absorbed or scattered by molecules and particles in the planet's atmosphere. The resulting spectrum (known as a transit transmission spectrum) can be used to characterize the planet's atmosphere (Seager and Sasselov, 2000; Brown, 2001; Hubbard *et al.*, 2001). This technique has been used to identify molecules in the atmospheres of hot ($>$600 K) Jupiter and Neptune-sized planets (Charbonneau *et al.*, 2002; Vidal-Madjar *et al.*, 2003; Pont *et al.*, 2008; Fraine *et al.*, 2014), and

---

[1] http://exoplanets.org

has also been used to infer the presence of high-altitude clouds and hazes for some worlds (Sing *et al.*, 2011, 2013; Kreidberg *et al.*, 2014; Knutson *et al.*, 2014a,b). In secondary eclipse, the difference between the in-eclipse and out-of-eclipse spectrum can reveal the exoplanet's reflected light and thermal emission spectra. Secondary eclipse observations have been used in attempts to detect molecular absorption features (Grillmair *et al.*, 2008), constrain carbon to oxygen ratios (Madhusudhan *et al.*, 2011) and identify temperature inversions (Knutson *et al.*, 2008), in which the atmosphere is hotter at higher altitudes than at lower altitudes. However, some of the these results have been called into question recently, and more work is needed to properly characterize these planets (Line *et al.*, 2014).

Characterizing Earth-like planets is currently not possible with existing telescopes and instruments, but should become more feasible with the development of larger telescopes and more advanced instrumentation. Multiple missions have been proposed for obtaining reflected or thermally emitted spectra of exoplanets, in which the light from the planet is isolated from the light of the host star. Examples of flagship missions include NASA Terrestrial Planet Finder (TPF) coronagraph and interferometer (Des Marais *et al.*, 2002), the Advanced Technology Large Aperture Space Telescope (AT-LAST) (Postman *et al.*, 2008, 2012), and Darwin from the European Space Agency (ESA) (Fridlund, 2000; Cockell *et al.*, 2009). Smaller missions such as Exo-C (a corographic telescope), Exo-S (which uses an external occulter, or starshade), and the Wide Field Infrared Survey Telescope (WFIRST), if launched, would most likely be able to characterize Neptune and Jupiter-sized planets, with possible characterization of Earth-sized planets if very nearby targets can be found (Spergel *et al.*, 2013). While the exact specifications are not yet in place, coronagraph missions have been proposed for characterizing terrestrial planets from the ultraviolet to the near-infrared (Levine *et al.*, 2009), and interferometer missions have been proposed for characterizing the thermal emission spectra of planets (Lawson *et al.*, 2009). Telescopes that could spectroscopically characterize an Earth-like exoplanet would be large ($>$4 m, but likely 8 m or larger) (Postman *et al.*, 2008). Given the cost and technological challenges associated with developing such a telescope, missions that can obtain a direct spectrum of an Earth-like planet are still in planning stages and at least 10 years away, and likely longer.

Transit transmission spectroscopy of potentially habitable planets may provide an opportunity to characterize atmospheres of Earth-like planets sooner, perhaps within the next 10 years (Deming *et al.*, 2009; Rauer *et al.*, 2011; Hedelt *et al.*, 2013; Rodler and López-Morales, 2014). Planets can be characterized more readily via transit transmission spectroscopy than via observations of reflected or thermal emission spectra because the light from the star is not removed in transit transmission spectroscopy, negating the need for a sophisticated coronograph or interferometer. However, the drawbacks of transit transmission spectroscopy are that it can only be used for transiting planets, and that it only reveals information about the atmosphere, not the surface. Currently, only planets that are much hotter and much larger than Earth have been characterized in transit transmission. But with upcoming large-aperture ground and space-based telescopes, it will be possible to obtain spectra with lower noise levels, allowing for the characterization of the atmospheres of transiting Earth-like exoplanets, perhaps within the next decade. Gases such as H_2O and CO_2 are predicted to be detectable with the upcoming James Webb Space Telescope (JWST, projected launch in 2018), and the biosignature gases O_2, O_3 and CH_4 may also be detectable with JWST if hundreds of hours of telescope time are devoted to a single target (Deming *et al.*, 2009; Kaltenegger and Traub, 2009; Belu *et al.*, 2011). Prospects for detectability are more promising with large ground-based telescopes such as the European Extremely Large Telescope (E-ELT, projected first light in early 2020's), which could detect O_2 in the atmosphere of an Earth-like planet orbiting an M dwarf in $\sim$20 hours of in-transit observing time (Rodler and López-Morales, 2014).

As the expected data from transit transmission observations increase in quality, so too must models of transit transmission spectroscopy. The noise levels for current transit transmission observations allow only the largest spectral features to be detected. However, future ground and space-based telescopes will be able to achieve lower noise levels, allowing for additional features to be detected. Furthermore, effects that could be ignored for close-in planets may need to be included in models for planets orbiting further from their host stars, such as habitable zone planets. In light of this, I propose that two physical processes, refraction and multiple forward scattering, have important implications for future transit transmission observations. Refraction strongly affects planets orbiting further away from their host stars than the planets being characterized today (Sidis and Sari, 2010; García Muñoz *et al.*, 2012), and the effect of forward scattering has been predicted to be only moderately strong for the most favorable cases (de Kok and Stam, 2012). Because of their limited applicability to current observations, refraction and forward scattering are ignored by existing models for exoplanet transit transmission spectroscopy, with a few exceptions (de Kok and Stam, 2012; García Muñoz *et al.*, 2012; Bétrémieux and Kaltenegger, 2014). However, I propose that refraction and forward scattering will result in effects that could be detectable with telescopes like JWST and E-ELT. In the following chapters I will describe the first model for transit transmission spectroscopy that includes the effects of both refraction and multiple forward scattering. I examine the effects of these two processes on transit transmission spectra and calculate how they affect the detectability of spectral features. I will also show that refracted and scattered light lead to increases in flux in transit light curves that could be detectable with JWST or E-ELT. Lastly, I will use the model to simulate spectra of Earth-like exoplanet atmospheres and develop new techniques to characterize Earth-like exoplanets, particularly with regards to habitability and biosignatures.

1.1 Transit Transmission Spectroscopy Background

As a planet transits its host star, the atmosphere is backlit and some of the star's light is transmitted through the planetary atmosphere on trajectories similar to the path of light during sunrise and sunset. Light on these paths can be absorbed, scattered and refracted by molecules and particles in the atmosphere, and the resulting spectrum of light is the transit transmission spectrum. Figure 1.1 shows a diagram of a transit event. Prior to ingress (start of transit) and after egress (end of transit), when the planet is not eclipsing the host star, the observer detects all of the star's flux. After ingress and before egress, the opaque part of the planet blocks light at all wavelengths. For wavelengths at which the planetary atmosphere is highly absorptive, the atmosphere blocks more of the star's light, decreasing the total amount of flux observed. The amount of absorption from the atmosphere is typically quantified as the effective absorbing radius of the atmosphere, and is representative of the projected size of the planet that is blocking the star's light at a given wavelength. Because the absorption from the planetary atmosphere can only be inferred when comparing the in-transit and out-of-transit fluxes, transmission spectroscopy is considered an indirect characterization technique, whereas direct characterization techniques (employed by TPF-style missions) block or null out the star's light and directly measure flux from the planet. While it is normally assumed that the planet's flux is negligible in the out-of-transit (before ingress and after egress) spectrum, in Chapters 4 and 5 I will show that refracted and scattered light from the planet can be detected out-of-transit.

One strength of transit transmission spectroscopy is that absorption features in transit transmission are typically more detectable than in secondary eclipse observations of reflected light, and even in a thermal emission spectrum in some cases. Given the absence of flagship coronagraph or interferometer missions and the strength of atmospheric absorption features in transit transmission, it is likely that the first spectrum of an Earth-like exoplanet will be obtained via transit transmission spectroscopy. In transit transmission, the magnitude of the observed absorption signal is:

$$\frac{(R_p + R_{atm})^2}{R_s^2} \tag{1.1}$$

where R_p is the planetary radius, R_{atm} is the effective absorbing radius of the atmosphere,

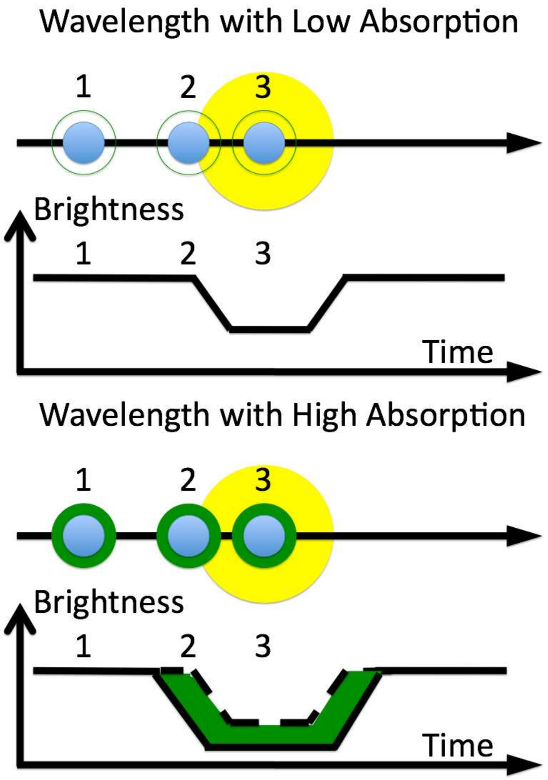

Figure 1.1: Diagram of transit transmission spectroscopy. In the out-of-transit spectrum (label 1), the planet has not yet eclipsed the star, and all of the stellar flux is observed. At ingress (label 2), the star is eclipsed by the solid, or opaque, portion of the planet, leading to a decrease in the observed flux. For wavelengths at which the planetary atmosphere is highly absorptive, the atmosphere absorbs some of the star's light, further decreasing the observed flux. The wavelength-dependent absorption is the transit transmission spectrum, and can be used to characterize the planetary atmosphere.

and R_s is the stellar radius. Assuming $R_p >> R_{atm}$, the fractional absorption from the atmosphere (not counting absorption from the planet as a whole) is:

$$\frac{2R_pR_{atm}}{R_s^2} \tag{1.2}$$

For secondary eclipse, the total amount of light reflected from the planet is the product of the stellar flux per unit area at the planet's orbit, the area of the planet intercepting the light, and the albedo of the planet, which is the fraction of light that is reflected by the planet. The stellar flux per unit area at the planet's orbit is $\frac{L}{4\pi d^2}$, and the area of the planet receiving the stellar flux is πR_p^2, so the total reflected flux is:

$$F = L\frac{\pi R_p^2}{4\pi d^2}A \tag{1.3}$$

where F is the total flux reflected by the planet, L is the stellar luminosity, d is the planet-star distance, and A is the albedo. To convert this into a secondary eclipse signal, Equation 1.3 needs to be divided by the total observable flux from the star (approximated here as a blackbody):

$$F_s = \pi\sigma T_s^4 R_s^2 = L/4 \tag{1.4}$$

where F_s is the stellar flux, σ is the Stefan-Boltzmann constant, T_s is the stellar temperature and R_s is the stellar radius. Dividing Equation 1.3 by Equation 1.4, the magnitude of a secondary eclipse signal is:

$$\frac{F}{F_s} = A\frac{R_p^2}{d^2} \tag{1.5}$$

Absorption features in transit transmission usually have a vertical extent $\geq$1 atmospheric scale height. The scale height of an atmosphere is the vertical distance over which an atmospheric quantity (typically pressure) decreases by a factor of e, or roughly 2.7. Most strong absorption features span no more than a few scale heights because as the pressure decreases, the number of absorbers decreases and the absorption from the atmosphere is reduced. Assuming a relatively small absorption feature with a signal of 1 scale height (which is ∼8 km for the Earth) for R_{atm}, the transit transmission signal for an Earth-like planet orbiting a Sun-like star is 0.2 ppm using Equation 1.2. In contrast, assuming an albedo of 0.3, the signal of the reflected spectrum is 0.0006 ppm based on Equation 1.5, roughly 2.5 orders of magnitude lower. The advantage of transit transmission is smaller for planets orbiting M dwarf stars, but even for an Earth-like planet orbiting near the inner edge of the habitable zone for an M5 star the flux signals are 5 ppm and 0.2 ppm for the transmission spectrum and reflected spectrum, respectively, which is a difference of a factor of ∼20. Figure 1.2 shows the ratio of the transmitted and reflected signals over a range of stellar types for three test cases: Earth, Jupiter, and Venus analogs. For planets with substantially larger radii, smaller scale heights, higher albedos, or close orbits the advantage of transit transmission spectroscopy can be reduced and even eliminated in some cases. For example, reflected light has a stronger signal for a Venus for the smallest stars because of its small scale height, large albedo, and close-in orbit around the small, faint stars. However, for most planets transit transmission spectroscopy will result in a stronger observable signal than a reflected secondary eclipse spectrum. Figure 1.2 shows that transmission spectroscopy is more favorable for all cases for the Earth and Jupiter cases. Secondary eclipse observations of thermally emitted light, while more complicated to calculate, have also been shown to be less favorable than transit transmission observations for most potentially habitable planets (Belu *et al.*, 2011). This means that the first spectrum of an Earth-like exoplanet is likely to be a transit transmission spectrum, highlighting the need to have accurate models that can predict what exoplanets will look like in transit transmission, especially Earth-like exoplanets.

1.2 Refraction

As light travels through a planetary atmosphere, it's path will change in response to a gradient in the index of refraction of the atmosphere. The index of refraction will decrease

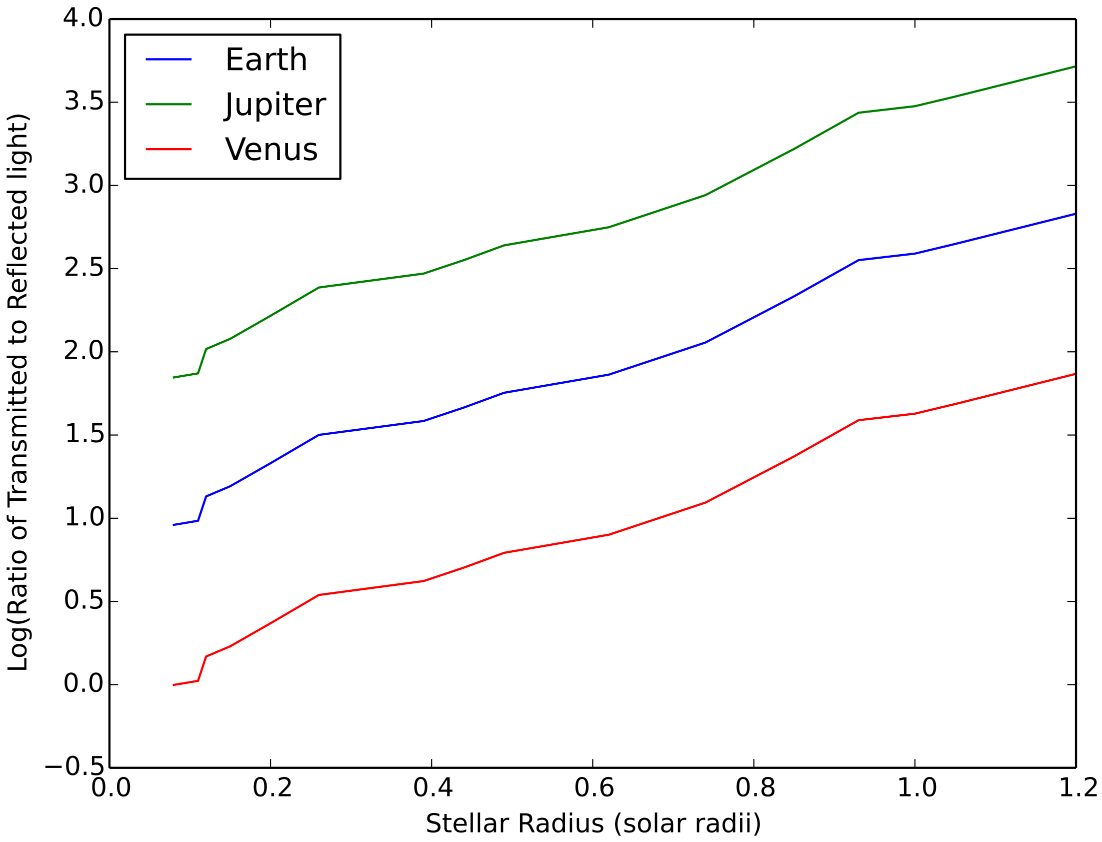

Figure 1.2: The log (base 10) of the ratio of transmitted to reflected light for Earth, Jupiter and Venus analog cases as a function of stellar radius. For each case, the planetary radius and atmospheric scale height are invariant. The planet-star distance for each stellar radius is the distance from the Sun for each planet multiplied by the square root of the stellar luminosity, which very roughly accounts for the fact that smaller stars are fainter, so any given planet must be closer in to its host star to maintain a certain temperature (and therefore atmospheric scale height). For the Earth and Jupiter cases, transmission spectroscopy will always be more favorable, though the advantage diminishes for fainter stars. For the Venus case, reflected light will have a stronger signal for stellar radii <0.1 $R_\odot$. This is because Venus has a small scale height and a high albedo. For most scenarios, though, transit transmission spectroscopy has a stronger signal than reflected light, potentially providing a more favorable technique for characterizing exoplanets.

with altitude as the density decreases. Light is refracted in an atmosphere as a repeated application of Snell's Law, which relates the angles of incidence and refraction for light traveling between two materials with different indices of refraction:

$$\frac{\sin\theta_1}{\sin\theta_2} = n_2/n_1 \tag{1.6}$$

In a planetary atmosphere, there is no discrete boundary for different indices of refraction, but there is a continuous gradient. The index of refraction in a planetary atmosphere can be related to the density using the Gladstone-Dale Relationship:

$$n = 1 + \alpha_0 \rho/\rho_0 \tag{1.7}$$

where n is the index of refraction, ρ is the number density, ρ_0 is the number density at some reference level and α_0 is the refractivity (index of refraction minus 1) of the atmosphere at the reference level.

Refraction has been shown to be an important effect for understanding planets and moons in the solar system in situations that are analogous to transit transmission spectroscopy. In solar and stellar occultation measurements performed in the solar system, a planet's atmosphere is backlit by the Sun or a star. Refraction sets a limit on the altitudes and pressures that can be probed in occultation measurements, and also increases the path lengths through the atmosphere (Baum and Code, 1953; Smith and Hunten, 1990; Elliot and Olkin, 1996). A similar effect is seen in radio occultations. Refraction limits the depth to which a spacecraft's radio beam can penetrate the planet's atmosphere, and yields information about the atmospheric density and thermal structure (Tyler *et al.*, 1982). Ground-based spectra of the moon during lunar eclipses are analogous to transit transmission spectra in that the Moon is illuminated by light that travels through the Earth's atmosphere. However, for the light to reach the lunar surface it must be refracted by the Earth's atmosphere, and thus refraction is necessary for accurately modeling lunar eclipse spectra (García Muñoz *et al.*, 2012). Refraction is also a key process in planetary transits of the Sun, and during the

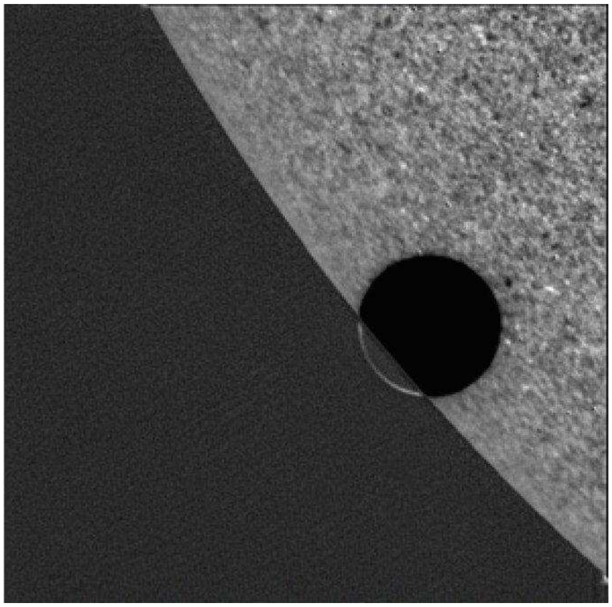

Figure 1.3: Rim of refracted light during the 2004 transit of Venus. Prior to second contact (when the full disk of Venus is on the Sun), light is refracted to telescopes in orbit around the Earth. Similar signals could be seen for transiting exoplanets, as discussed in further detail in Chapters 3 and 4.

2004 transit of Venus, a rim of refracted light could be seen on the trailing side of Venus before it crossed the solar limb, as shown in Figure 1.3 (Pasachoff *et al.*, 2011). While many of these observation types are currently only feasible within the solar system, the principle of refraction will still apply to exoplanet transit transmission observations.

For exoplanets in transit transmission, refraction was initially assumed to have a negligible effect on the altitudes and pressures that could be probed (Seager and Sasselov, 2000; Hubbard *et al.*, 2001). These first calculations of refraction were done for Hot Jupiter planets, for which the small planet-star separation results in minimal refractive effects. García Muñoz *et al.* (2012) were the first to show that refraction can set a limit of <1 bar for planets in the habitable zones of solar type stars, and that this reduces the strength of absorption features. I expand on their work by examining the effect of refraction on the pressures that can be probed over a range of planet and stellar types. In particular, I will show that refraction can severely limit the detectability of biosignature gases for Earth-like planets.

Refraction can also lead to changes in an exoplanet transit light curve because light can be refracted through the planet's atmosphere to a distant observer even when the planet is out-of-transit, as shown in Figure 1.3 for the 2004 Venus transit. This effect was predicted for exoplanets by Sidis and Sari (2010). However, their work focused on hot, close-in planets and also ignored opacity sources that would limit the depths that could be probed in transit transmission. In Chapter 4 I build on this initial exploration by performing a comprehensive study of the detectability of refracted light in the out-of-transit light curve for a number of planet and stellar types with realistic opacity limits.

I will also show that refracted light in a transit light curve could be used to obtain altitude-dependent spectra. Such spectra are regularly obtained via solar and stellar occultation measurements in the solar system and can be used to derive vertical mixing ratio profiles of atmospheric gases (Smith and Hunten, 1990; Elliot and Olkin, 1996). However, these types of observations will not be possible for exoplanets because they require the projected size of the planetary atmosphere to be larger than the projected size of the star. In solar and stellar occultations, the telescope is much closer to the planetary atmosphere than the Sun or background star, and this condition is met, allowing for vertical resolution on the order of a few km or less to be achieved. In exoplanet transits, the exoplanet and star are effectively at the same distance from observers on the Earth, and this condition will not be met. Given the lack of existing techniques to obtain altitude-dependent spectra of exoplanets, I propose that obtaining vertical profiles of gases in exoplanet atmospheres through refraction would provide an additional, powerful technique to enhance our understanding of these atmospheres. For example, on the Earth both O_3 and H_2O are unevenly distributed. O_3 is primarily concentrated in the stratosphere on Earth because it is photochemically generated. Detecting O_3 predominantly in the stratosphere of an exoplanet would strongly suggest that the planet had a temperature inversion in the stratosphere. Vertical profiles of O_3, or any photochemically produced gas, would increase understanding of the photochemistry in an exoplanet atmosphere. H_2O is primarily found in Earth's troposphere (altitudes $<$20 km), and would only reach higher regions of the atmosphere (like the stratosphere) for higher temperature planets, or for planets undergoing a moist or runaway greenhouse process, during which water escapes to space, ultimately making a planet uninhabitable (Kasting, 1988). Therefore, a detection of H_2O at high altitudes in an exoplanet atmosphere would suggest that the planet was not habitable.

1.3 Scattering from Clouds and Hazes

Scattering of light from particles, typically from clouds and hazes, is ubiquitous in solar system atmospheres (e.g. Marley *et al.*, 2013). Here I refer to ‘clouds’ as condensates and ‘hazes’ as photochemically produced particles. On Earth, water clouds have a large impact on our planet's spectrum (e.g. Robinson *et al.*, 2011). Furthermore, aerosols from a variety of sources, such as volcanism, can lead to increases in photon extinction (e.g. Charlson *et al.*, 1992), especially along limb paths such as those inherent to transit transmission spectroscopy. Venus has thick layers of planet-wide H_2SO_4 aerosols (Young, 1973). Mars has thin H_2O clouds (Kieffer *et al.*, 1977), CO_2 clouds (Montmessin *et al.*, 2006), and planet-wide dust storms (Pollack *et al.*, 1979) that can vastly increase its aerosol optical depth, or opacity. In the outer solar system, the giant planets have clouds composed of NH_4, CH_4, and H_2O (West *et al.*, 1986; Lunine, 1993; Baines *et al.*, 2002) and photochemical hydrocarbon hazes (Pollack *et al.*, 1987b). Saturn's moon Titan also has a thick hydrocarbon haze (Smith *et al.*, 1981) and methane clouds (Brown *et al.*, 2010).

Considering how pervasive clouds and hazes are in our solar system, it is not surprising that many exoplanets are thought to be cloudy or hazy. The presence of clouds or hazes in an exoplanet atmosphere is inferred from very weak or no absorption features in transit transmission. For example, HD 189733b shows much weaker Na and K potassium absorption than predicted by cloud and haze-free model spectra (Sing *et al.*, 2011). In extreme cases, some spectra show no absorption features at all, such as GJ 1214b (Bean *et al.*, 2010; Kreidberg *et al.*, 2014), GJ 436b (Knutson *et al.*, 2014a), and HD 97658b (Knutson *et al.*, 2014b). Given their sizes, these worlds likely have extended H_2-rich atmospheres, so the lack of detected absorption features strongly suggests that high-altitude clouds or hazes are blocking out the deepest portions of the atmosphere at which the atmosphere can absorb the most light. However, the mechanisms for creating and maintaining such a high altitude aerosol layer are currently unknown.

Despite the prevalence and recognized importance of clouds and hazes in exoplanet atmospheres, one area that has received little attention is the effect of multiple forward scattering from these types of particles in transit transmission. For particles that are larger than the wavelength of light being scattered, the scattering phase function (the distribution of scattering angles) can be peaked in the forward direction. Forward scattered light could be important in transit transmission spectroscopy because there is a small range of possible scattering angles that will result in a photon staying in the beam to a distant observer, and forward scattered photons may be deflected by a small enough angle that they can still be observed. Currently, most models of transit transmission spectroscopy work under the assumption that any scattering from clouds and hazes can be treated as extinction, such that once the photon is scattered, it is assumed to leave the beam and will never reach a distant observer (e.g., Fortney (2005); Howe and Burrows (2012); Vahidinia *et al.* (2014)). This has shown to be appropriate for Rayleigh scattering (Hubbard *et al.*, 2001), which applies only to small particles that are not highly forward scattering. However, for larger particles that are highly forward scattering, photons can be scattered and still reach a distant observer, even after being scattered multiple times. This effect has been explored by de Kok and Stam (2012). They make a general prediction that forward scattering could lead to a decrease in the model-generated effective absorbing radius of the atmosphere by as much as 1 scale height, but they do not explore how this result depends on the planet's atmospheric composition or planet-star geometry. Thus, the effect of forward scattering on exoplanets that are smaller or cooler than Hot Jupiters has not yet been explored. Scattering in an exoplanet light curve has also not been explored. In particular, light can be scattered by cloud and haze particles even when the planet is not in transit, leading to an increase in flux prior to ingress and subsequent to egress. To explore the effect of forward scattering on decreasing the in-transit effective absorbing radius of a planet and the effect on transit light curves, I have developed a Monte Carlo scattering module that can work in concert with an existing radiative transfer code to generate transit transmission spectra of exoplanets with forward scattering included.

1.4 Implications for Astrobiology

Astrobiology is the study of the origin, evolution, distribution, and future of life in the universe. Two of the goals of astrobiology are to identify habitable environments beyond the Earth and to understand and ultimately observe signatures of life, or biosignatures. Transit transmission observations of Earth-like planets may provide constraints on both habitability and biosignatures, and may reveal spectral signatures that are not detectable in reflected or thermal emission spectra. This is due to the longer path lengths inherent in transit transmission observations enhancing the detectability of signals that are too weak in reflected and thermal emission observations. Furthermore, as discussed previously, the first spectra of an Earth-like exoplanet will likely be transit transmission spectra, highlighting the importance of studying habitability markers and biosignatures in transit transmission spectra.

1.4.1 Habitability Determination

One of the goals of the 2008 NASA Astrobiology Roadmap is to identify habitable environments beyond the Earth (Des Marais *et al.*, 2008). For exoplanets, habitability has typically been defined as the ability of the planet to maintain liquid water on its surface (Kasting *et al.*, 1993; Kopparapu *et al.*, 2013). Whether or not water is in the liquid phase depends on the surface temperature and pressure. Surface temperature can be constrained either by climate modeling or by direct observations. Climate studies to constrain habitability have been performed by a number of authors for exoplanets (Kasting *et al.*, 1993; Selsis *et al.*, 2007; Wordsworth *et al.*, 2010; Yang *et al.*, 2014), and for solar system planets, typically with respect to the question of how to warm the Early Earth and Early Mars (Sagan and Mullen, 1972; Pollack *et al.*, 1987a; Feulner, 2012). These works typically use radiative convective and/or general circulation models to determine surface temperature given the incident flux on the planet, the composition and structure of the planetary atmosphere, and the albedo. If the surface temperature is low enough to avoid a runaway greenhouse (in which the oceans boil and a planet loses its water rapidly) and warm enough to prevent a state of complete ice coverage, the planet is considered habitable. Surface temperature is an atmospheric quantity that can be characterized from thermally emitted radiation and is in principle a measurable atmospheric quantity (Rodgers, 1976), although in practice this could be difficult. For example, while the 8-12 μm window is sufficiently transparent to retrieve the Earth's surface temperature, observations of Venus in this window would yield information only on the cold (-33°) cloud-tops which are indistinguishable from a cool, ice-covered planet (Des Marais *et al.*, 2002).

Surface pressure, on the other hand, has proven much more difficult to constrain, despite its importance for habitability. For example, the triple point of water is at a pressure of 0.006 bars. At surface pressures below this, water is not stable in the liquid phase. For greater pressures, the boiling point of water is sensitive to pressure, with a value of $\sim$40°C at 0.1 bars and ∼175°C at 10 bars. Current methods for estimating pressure are typically only applicable for solar system worlds with known composition, or are dependent on having a cloud and haze-free planet (see Chapter 6 for a more detailed discussion). Because of the importance of surface pressure and the paucity of existing techniques for retrieving this quantity from exoplanet observations, in Chapter 6, I explore a new method to determine atmospheric pressure on exoplanets using dimer molecules that could be applicable to transit transmission observations of Earth-like exoplanets. Absorption from dimer molecules is more strongly dependent on atmospheric density (and therefore pressure) than that of non-dimer molecules, allowing for additional constraints to be placed on atmospheric pressure from dimer absorption than from non-dimer absorption alone. Dimer absorption features are weak in the reflected spectrum of the Earth (Robinson *et al.*, 2011), but have been identified in lunar eclipse spectra (Pallé *et al.*, 2009), which are similar in geometry to transit transmission spectra.

While temperature and pressure are essential for determining if a planet can have liquid water on its surface, geological activity may be important for the origin of life and for maintaining a habitable environment over long periods. For example, a *de novo* genesis of life appears to be reliant on chemical potential and redox gradients that were common in volcanic and hydrothermal settings early in the Earth's history (Sleep *et al.*, 2011; Stüeken *et al.*, 2013). Furthermore, at least some volcanic outgassing is required to replenish the drawdown of CO_2 by silicate weathering and prevent the onset of a snowball-Earth state. On Earth, the carbonate-silicate cycle, a product of plate tectonics, regulates the concentration of CO_2 over time to maintain a stable climate (Walker *et al.*, 1981), and similar climate regulation may be achieved in a stagnant lid regime (Pollack *et al.*, 1987a). Consequently, a means to detect geological activity on a given planet would suggest a greater likelihood of that planet being habitable. In Chapter 7, I explore transient sulfate aerosol signals as an indicator for geological activity. On Earth, subduction-induced volcanism can inject SO_2

into the stratosphere, where it can react to form H_2SO_4 aerosols with lifetimes from months to years. These explosive eruptions lead to transient aerosol layers, which would lead to an increase in effective absorbing radius of the atmosphere in transit transmission, followed by a gradual decrease. The effect of volcanic aerosol layers is small for the Earth's reflected spectrum, resulting in an increase of flux by 6% for the Pinatubo eruption in 1991, which led to the largest increase in stratospheric sulfate aerosols in the past 100 years (Minnis *et al.*, 1993). However, I will show that these aerosol layers can have a much stronger effect on the Earth's transit transmission spectrum.

1.4.2 Directly Detecting Biosignatures in the Atmospheres of Earth-like Planets

With the launch of JWST and construction of upcoming large ground-based telescopes, atmospheric molecules, including biosignature gases, could be detected on a nearby inhabited, transiting, planets within the next decade. Several groups have investigated the detectability of molecules such as H_2O, CO_2, O_2, O_3 and CH_4 for Earth-like exoplanets (Kaltenegger and Traub, 2009; Deming *et al.*, 2009; Belu *et al.*, 2011; Rauer *et al.*, 2011; Hedelt *et al.*, 2013; Rodler and López-Morales, 2014). H_2O and CO_2 are potential habitability markers (Des Marais *et al.*, 2002), and O_2, O_3 and CH_4 are possible biosignature gases. In general, they find that these molecules could be detected in the atmosphere of an Earth-analog planet orbiting in the habitable zone of an M dwarf star in hundreds of hours with JWST and tens of hours with E-ELT. However, these works have neglected the effect of atmospheric refraction on transmission spectra. Refraction limits the detectability of spectral absorption features, and therefore can increase the amount of integration time required to detect molecules. I quantify the effect of refraction on the detectability of spectral absorption features, including biosignatures, for Earth-analog planets in Chapter 3. In particular, I will show that refraction can greatly increase the required integration time to detect molecular absorption features for Earth-like planets orbiting Sun-like stars.

The longer path lengths inherent to transit transmission observations should allow biosignature gases to be detectable in transit transmission even if their absorption is too weak to be detectable in direct beam reflected and thermally emitted light. In Chapter 6, I investigate the O_2-O_2 dimer absorption features at 1.06 and 1.27 μm as potential biosignature gases for Earth-like exoplanets in transit transmission. Another example of a potential biosignature in transit transmission is transient sulfate aerosols, when observed in conjunction with O_2 and O_3. While O_2 and O_3 are considered biosignature gases, one scenario in which they can form abiotically is if volcanic outgassing rates are low (Hu *et al.*, 2012; Domagal-Goldman *et al.*, 2014). Therefore, a co-detection of O_2 or O_3 with transient sulfate aerosols, which are suggestive of active volcanism, would be a more robust biosignature than O_2 or O_3 alone.

1.5 Outline

In Chapter 2, I introduce the transit transmission model and the refraction and scattering ray tracing scheme. I provide a detailed description of the refraction and scattering components (Section 2.1). I discuss the method for performing detectability calculations (Section 2.2). I validate the model against observations of the Earth, describing the input model atmospheres and showing a comparison against satellite observations of the Earth, lunar eclipse spectra, and theoretical and empirical estimates of the Venus scattering footprint (Section 2.3).

Chapters 3, 4, and 5 cover the effects of refraction and scattering on transit transmission spectroscopy. In Chapter 3, I apply the model to Earth-analog exoplanets and examine the effect of the maximum tangent pressure on the detectability of spectral absorption features. I also describe a new technique to obtain altitude-dependent spectra of exoplanets from variations in the wavelength-dependent transit light curve. In Chapter 4, I examine this further and show that a detection of out-of-transit refracted light would be indicative of a haze-free atmosphere over a wide range of planet and stellar types. I examine the effect of forward scattering on transit transmission spectra and transit light curves in Chapter 5 and show that forward scattering can increase the detected flux in the in-transit spectrum and can lead to detectable levels of out-of-transit scattered light.

In Chapters 6 and 7, I apply the transit transmission model to Earth-like exoplanets with an emphasis on constraining habitability and detecting biosignatures. In Chapter 6, I examine the use of dimer molecules as a pressure gauge and the viability of O_2 dimer molecules as biosignatures. In Chapter 7, I explore the concept of transient sulfate aerosols as a tracer for volcanism, as well as how a transient sulfate aerosol signal could be a biosignature with a co-detection with O_2 or O_3. Conclusions from all chapters are presented in Chapter 8.

Chapter 2

MODEL DESCRIPTION AND VALIDATION

In this chapter I describe the transit transmission model with an emphasis on the refraction and scattering components. The model combines a backwards Monte Carlo ray tracing scheme with an existing radiative transfer code to generate transit transmission spectra and transit light curves. I then describe the method used for detectability calculations. Following that, I validate the transit transmission model against observations of the Earth from the ATMOS mission, ground-based lunar eclipse spectra, and theoretical and empirical estimates of the Venus scattering footprint. Portions of this chapter were originally published in collaboration with V. S. Meadows and D. Crisp in the 1 September 2014 issue of the *Astrophysical Journal* (Misra, Meadows, and Crisp, 2014, *ApJ*, Vol. 792, 61) and are reproduced below with permission of the American Astronomical Society.

2.1 Model Description

I have developed a model for transit transmission spectroscopy that includes refraction and multiple, forward scattering. The model uses the normal-incidence optical depths calculated by an existing radiative transfer code and combines them with a Monte Carlo ray tracing model to generate transit transmission spectra. The model can generate time-averaged transit transmission spectra and wavelength-dependent transit light curves. The details of the model are described below.

2.1.1 Radiative Transfer Code

The work presented here builds on an existing radiative transfer model, Spectral Mapping Atmospheric Radiative Transfer (SMART) (Meadows and Crisp, 1996; Crisp, 1997; Robinson *et al.*, 2011). SMART is a spectrum resolving (line-by-line), multi-stream, multiple scattering radiative transfer model that has been used primarily for planetary atmospheres, both for generating spectra and as a key component in climate calculations (Catling *et al.*, 2012). In this work, I use the spectral generation component of SMART to model transit transmission spectra.

The main inputs to SMART of consequence to the transit transmission model consist of a model atmosphere, line-by-line absorption coefficients and aerosol scattering properties. A model atmosphere typically consists of a temperature-pressure profile and profiles for the abundances of absorbing gases in the atmosphere. The absorption coefficients used here were calculated with the code Line-By-Line ABsorption Coefficients (LBLABC, written by Dave Crisp). LBLABC uses line lists and input from the model atmosphere to calculate the wavelength-dependent absorption coefficients for each gas at each layer in the atmosphere. For this work, the line lists are from the HITRAN 2008 and 2012 databases (Rothman *et al.*, 2009, 2013). The required aerosol properties are the aerosol optical depth at each altitude layer at a reference wavelength, the scattering and extinction efficiencies as a function of wavelength, and the scattering phase function at each wavelength and for each altitude layer, either as a full phase function or parameterized as a Henyey-Greenstein phase function. Given the optical depth at each altitude layer at a reference wavelength, the aerosol scattering and extinction optical depths at each wavelength and each altitude can be calculated by multiplying the reference wavelength optical depth by the scattering and extinction efficiencies, normalized to the efficiencies at the reference wavelength.

The transit transmission spectrum for each tangent altitude, or minimum altitude, can be generated by combining the normal-incidence optical depths calculated by SMART and

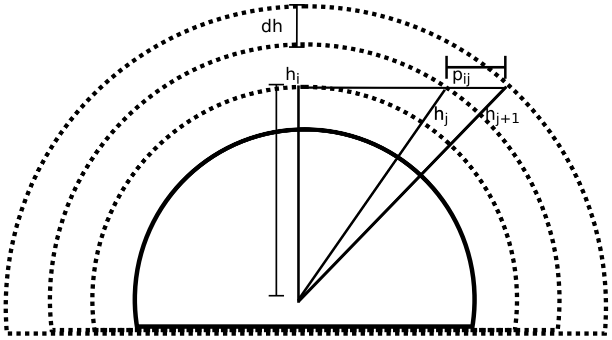

Figure 2.1: Path lengths in the transit transmission geometry. The h_i, h_j, and h_{j+1} altitudes are the same altitudes as in Equation 2.1. The total path is the sum of the p_{ij} values between each pair of altitudes in the model atmosphere. The total path lengths and optical depths for a path in transit transmission are typically 1-2 orders of magnitude larger than the vertical path length and optical depth.

the path lengths through the atmosphere. The path length between two adjacent layers of the atmosphere j and $j+1$ for a path p_{ij} with a tangent altitude of h_i is:

$$p_{ij} = \sqrt{h_{j+1}^2 - h_i^2} - \sqrt{h_j^2 - h_i^2} \tag{2.1}$$

Figure 2.1 shows an example path segment between two altitudes in the atmosphere. The path through one layer (p_{ij}) will generally be much larger than the vertical path, dh, increasing the total optical depth along the path. Fortney (2005) shows that the ratio of the transmission optical depth to the vertical optical depth is:

$$\sqrt{\frac{2\pi R_p}{H}} \tag{2.2}$$

where R_p is the planet radius and H is the pressure scale height in the atmosphere. From this equation, the ratio of the transmission optical depth to the vertical optical depth is $\sim$75 for Earth and $\sim$128 for Jupiter.

The flux through the atmosphere at a given tangent altitude can be calculated via the Beer-Lambert law, which relates the transmittance of light to the optical depth in a material.

The transmittance $F(\lambda)_i$ at a given wavelength λ and an altitude layer i is:

$$F(\lambda)_i = e^{-\sum_j \tau_j * p_{ij}/(h_{j+1}-h_j)} \tag{2.3}$$

where τ_j is the normal incidence (vertical path) optical depth in layer j, p_{ij} is the path length given by Equation 2.1, and $h_{j+1} - h_j$ is the normal-incidence path length for layer j. The total transmission spectrum is the weighted sum of the wavelength-dependent transmittance at each tangent altitude, with the weight equal to the area of the atmospheric annulus at each layer. The area of the annulus depends on the altitude structure of the model atmosphere. The area at each layer A_i is:

$$A_i = \pi[(h_{i+1} + R_P)^2 - (h_i + R_P)^2] \tag{2.4}$$

where R_p is the radius of the planet. The percent of flux transmitted through the entire atmosphere, $F(\lambda)$, is:

$$F(\lambda) = \frac{\sum_i F_{\lambda i} * A_i}{\sum_i A_i} \tag{2.5}$$

where $\sum_i A_i$ is the total projected area of the atmosphere. The flux through the entire atmosphere can be converted to an effective absorbing radius with the following equation:

$$R_{eff}(\lambda) = \sqrt{\pi R_p^2 + (1 - F(\lambda)) * \sum_i A_i} \tag{2.6}$$

$(1 - F(\lambda))$ is the fraction of flux absorbed by the atmosphere, so the sum of the projected area of the planet and the absorption area of the planetary atmosphere is the total absorption from the planet and it's atmosphere. The square root of this value is the total effective absorbing radius of the planet and atmosphere. To get the effective absorbing radius of the atmosphere only, the planetary radius must be subtracted.

2.1.2 Ray Tracing Geometry

The geometry is one of the primary factors in determining the effects of refraction and scattering. The physics of refraction and scattering are symmetric in time, such that the deflections due to refraction and scattering can be modeled in either a forward or backwards ray tracing model. My model adopts a backwards ray tracing scheme, in which light is sent from the distant observer and traced through the atmosphere to the host star. The main advantage of a backwards ray tracing model is that only a very narrow subset of photon trajectories can reach a distant observer from an exoplanet because a distant observer is essentially a point source from the planet at distances on the order of parsecs. In contrast, a relatively large subset of trajectories can reach the planet from the star because the star has an angular radius that is typically on the order of a degree. Choosing the backwards model greatly reduces the number of initial conditions by fixing the starting point for the photons in the model.

2.1.3 Coordinate Systems

The model tracks the photon position and trajectory in three coordinate systems: a global coordinate system, a photon coordinate system, and a refraction coordinate system. A separate photon coordinate system is helpful because the resulting trajectory after a scattering event depends on the photon's initial trajectory, and therefore scattering angles can be calculated from the orientation of the photon and converted into a global frame. The refraction coordinate system is necessary because refraction is a two-dimensional effect in spherically symmetric atmospheres because there is an index of refraction gradient in only one direction (relative to altitude). I've developed the following methodology to track the photon path in each coordinate system and to convert between the coordinate systems. The global coordinate system is oriented so that the z axis points towards the star, with the origin at the center of the planet. The photon position and trajectory at each step along the path are tracked relative to the global frame. The trajectory in the global frame is given by the two angles in spherical coordinates, with θ as the polar angle and ψ as the azimuthal angle. Initially, θ is set to 0.

2.1.3.1 Photon Frame

The photon frame is used to transform new scattering angles to the global reference frame. The change in trajectory due to scattering is relative to the photon's initial trajectory. The photon frame is defined so to that the z-coordinate is in the direction of the photon's initial path. Mathematically, θ_p, the polar angle, is equal to 0 and ψ_p, the azimuthal angle, is set to 0, although it can take any value when θ_p equals 0. After a scattering event, the photon has a trajectory with angles $d\theta_p$ and $d\psi_p$. The unit vector in the photon frame for the new trajectory is:

$$n_p = \begin{pmatrix} \sin d\theta_p \cos d\psi_p & \sin d\theta_p \sin d\psi_p & \cos d\theta_p \end{pmatrix}$$

The new trajectory can be transformed to the global frame through two rotations, one about the z-axis and one about the y-axis.

$$R_z = \begin{pmatrix} \cos\psi & -\sin\psi & 0 \\ \sin\psi & \cos\psi & 0 \\ 0 & 0 & 1 \end{pmatrix}$$

$$R_y = \begin{pmatrix} \cos\theta & 0 & \sin\theta \\ 0 & 1 & 0 \\ -\sin\theta & 0 & \cos\theta \end{pmatrix}$$

In the above equations, θ and ψ are the initial trajectory of the photon in the global frame.

Applying R_z and R_y to n_p yields the following dx, dy and dz coordinates in the global frame:

$$dx = \cos d\psi_p \cos\psi \cos\theta \sin d\theta_p - \sin d\psi_p \sin d\theta_p \sin\psi + \cos d\theta_p \cos\psi \sin\theta \quad (2.7)$$

$$dy = \cos\psi \sin d\psi_p \sin d\theta_p + \cos d\psi_p \cos\theta \sin d\theta_p \sin\psi + \cos d\theta_p \sin\psi \sin\theta \quad (2.8)$$

$$dz = \cos d\theta_p \cos\theta - \cos d\psi_p \sin d\theta_p \sin\theta \quad (2.9)$$

dx, dy and dz can be calculated directly because θ, ψ, $d\theta_p$ and $d\psi_p$ are all known. These can be converted into the new θ and ψ angles in the global frame using the typical spherical coordinates transformations:

$$\theta = \cos^{-1} dz \tag{2.10}$$

$$\psi = \tan^{-1} \frac{dy}{dx} \tag{2.11}$$

2.1.3.2 Refraction Frame

I adopt the two-dimensional coordinate system used by van der Werf (2008) for calculating refraction. Because refraction is calculated in two dimensions and the global coordinate system is in three dimensions, I need a framework to convert between the two coordinate systems. I treat the refraction frame as a projection of the global coordinate system, in which the y axis is the same, and the x-z plane is projected into a new coordinate, which I label xz. The angle of refraction in two dimensions is θ_r, which can be thought of as the local zenith angle. As refraction alters the photon path, θ_r will change, and I need a way to convert changes in θ_r into changes in θ and ψ, the angles that determine the photon in the global coordinate system. In the global coordinate system, the differential position changes are:

$$dx = \sin\theta\cos\psi \tag{2.12}$$

$$dy = \sin\theta\sin\psi \tag{2.13}$$

$$dz = \cos\theta \tag{2.14}$$

Given these values, I can calculate the initial θ_r given θ and ψ value (see Figure 2.2 for reference).

$$\theta_r = \tan^{-1} \frac{\sqrt{dx^2 + dz^2}}{dy} \tag{2.15}$$

As θ_r changes due to refraction at each step along the path through the atmosphere, the spherical coordinate angles need to be updated accordingly. I assume that the relative

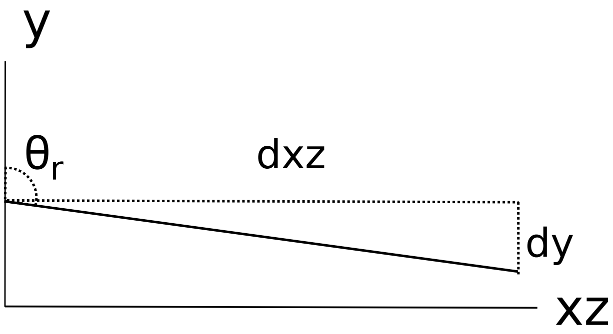

Figure 2.2: Diagram of the refraction coordinate system. This is similar to the global coordinate system in that the *xz* axis is a projection of the *x* and *z* plane to one dimension. This coordinate system is necessary because I need to convert the refraction angle (which is calculated in two dimensions) back to the global coordinate system (in three dimensions)

ratio of dx and dz stays constant because there is no index of refraction gradient in the x-z plane, and thus the relative trajectory in the *x* and *z* directions should always be constant. Mathematically, I let $dx_{new}/dx = dz_{new}/dz = C$, where C is a constant. To calculate the new θ and ψ angles I start by calculating new values for dx, dy and dz:

$$dx_{new}^2 + dy_{new}^2 + dz_{new}^2 = 1 \tag{2.16}$$

$$C^2dx^2 + dy_{new}^2 + C^2dz^2 = 1 \tag{2.17}$$

$$dy_{new} = \sqrt{1 - C^2(dx^2 + dz^2)} \tag{2.18}$$

$$dy_{new} = \sqrt{1 - C^2(dxz^2)} \tag{2.19}$$

where $dxz = \sqrt{dx^2 + dz^2}$.

From Equation 2.15, which defines θ_r in terms of dx, dy, and dz, I can now calculate new values for dx, dy and dz.

$$\tan\theta_r = \frac{\sqrt{dx_{new}^2 + dz_{new}^2}}{dy_{new}} \tag{2.20}$$

$$\tan\theta_r = \frac{C^2dxz^2}{dy_{new}} \tag{2.21}$$

$$\tan\theta_r = \frac{C^2 dxz^2}{1 - C^2 dxz^2} \tag{2.22}$$

The last equation is equivalent to:

$$\sin\theta_r = C dxz \tag{2.23}$$

$$C = \frac{\sin\theta_r}{dxz} \tag{2.24}$$

$$\tag{2.25}$$

θ_r, dx, dz and dxz are all known, so I can now calculate C. From the definition of C, I can calculate new values for dx_{new} and dz_{new}:

$$dx_{new} = C dx \tag{2.26}$$

$$dz_{new} = C dz \tag{2.27}$$

$$\tag{2.28}$$

Lastly, with C known, dy_{new} is:

$$dy_{new} = \sqrt{1 - C^2 dxz^2} \tag{2.29}$$

$$dy_{new} = \sqrt{1 - (\sin\theta_r)^2} \tag{2.30}$$

$$dy_{new} = \cos\theta_r \tag{2.31}$$

With dx_{new}, dy_{new} and dz_{new}, the new θ and ψ values are:

$$\theta = \cos^{-1} dz_{new} \tag{2.32}$$

$$\psi = \tan^{-1}\frac{dy_{new}}{dx_{new}} \tag{2.33}$$

2.1.4 Calculating Refraction

Following van der Werf (2008), four variables are solved at each step: the altitude (h), the complement of the local zenith angle (β), the polar angle measured from the planet's center

(ϕ), and the total deflection due to refraction (ε). The equations that describe these four variables and their relation to each other are:

$$\begin{aligned} dh &= \sin\beta ds && (2.34)\\ d\beta &= \left(\frac{\cos\beta}{R_p+h}+\frac{1}{r}\right) ds && (2.35)\\ d\phi &= \frac{\cos\beta}{R_p+h} ds && (2.36)\\ d\varepsilon &= d\beta - d\phi = \frac{1}{r} ds && (2.37) \end{aligned}$$

where ds is the path step length, R_p is the planetary radius, and $\frac{1}{r}$ is the curvature, which is given by:

$$\frac{1}{r} = \cos\beta \frac{1}{n}\frac{dn}{dh} \tag{2.38}$$

n is the index of refraction, and $\frac{dn}{dh}$ is the index of refraction gradient with respect to altitude. At each step on the path, n and $\frac{dn}{dh}$ are calculated by linearly interpolating between model atmosphere layers. For a full derivation of the equations above, see Appendix A.

I solve the equations above at each step using a fourth-order Runge-Kutta method. I find that for Earth-like atmospheres, path step sizes of 1-10 km are sufficient for an accuracy in the final refraction angles of 99% or greater, when compared to simulations with smaller step sizes. For other planetary atmospheres, a step size of <1 scale height is typically small enough to ensure accurate refraction angles, though smaller path steps are required for the scattering component of the model.

2.1.5 Scattering

Most models for transit transmission spectroscopy treat scattering from particles as a form of extinction, i.e., a scattered photon is assumed to be lost from the beam to a distant observer. However, scattered photons can be scattered multiple times and still reach a distant observer. To simulate the scattering of photons, I've implemented a Monte Carlo scattering code in which the photon scattering locations and scattering trajectories are randomly sampled. At a given wavelength, a large number (typically $>$1000) of photon paths are traced for each altitude in the model atmosphere. While Monte Carlo models often use 10's of thousands to millions of photons, a smaller number is appropriate for simulating transit transmission spectra because I find that only the forward scattered trajectories need to be resolved. Before the photon's path begins, an optical depth that that the photon is allowed to travel is selected randomly:

$$\tau_{rand} = -\log(r) \tag{2.39}$$

where r is a random number sampled uniformly between 0 and 1. This framework allows the scattering location to be random, but constrains the scattering position so that within the first optical depth along the path, $1-e^{-1}$ photons are scattered, and within the second optical depth $1-e^{-2}$ photons are scattered, etc, which is what is predicted from the Beer-Lambert law.

After τ_{rand} is selected, two quantities are tracked along the photon's path: 1) the scattering optical depth 'seen' by the photon and 2) the deflection in the trajectory due to refraction. The scattering optical depth is calculated by multiplying the aerosol extinction due to scattering in each layer by the path step size. The path step is set to 10^{-5} times the maximum path length given in Equation 2.1 (when summed over all values of j). This is the largest step size that ensures that errors in photon trajectory are less than 1% for all tangent altitudes and over a wide range of planetary radii, scale heights and scattering phase functions. Additionally, the step size is $<$1 km and $<$0.001 times the scale height for all cases considered here. Note that the path step size is not mean free scattering path length, instead, it is the length at which the photon's path is sampled.

At any step along the path, if the cumulative scattering optical depth seen by the photon exceeds τ_{rand}, the photon's path is stopped and a scattering event occurs. The model linearly interpolates to find the best estimate for the position at which the optical depth seen by the photon equals τ_{rand}. The new scattering angles are selected with respect to the photon's trajectory. In the photon coordinates, θ_p=0 and the trajectory points in the direction of the photon coordinate z axis. The change in the photon's trajectory (in photon coordinates) are selected randomly from the scattering phase function for $d\theta_p$ and selected from a uniform distribution between 0 and 2π for $d\psi_p$. More specifically, $d\theta_p$ is chosen using inverse transform sampling. First, the normalized cumulative phase function of $P(\cos d\theta_p)d(\cos\theta_p)$ is calculated, and then a random number (r) from the uniform distribution between 0 and 1 is generated. The angle chosen corresponds to the largest value of the cumulative distribution function that is $\leq r$. In essence, r is a percentile, and the angle is picked such that it's cumulative distribution function is at that percentile. The new angles in photon coordinates are $d\theta_p$ and $d\psi_p$. The $d\theta_p$ and $d\psi_p$ in the photon coordinates are then transformed into the global coordinates, as described in Section 2.1.3

After a scattering event, the photon is again sent through the atmosphere, beginning at the point of scattering and with the calculated scattering trajectory. The process described above is repeated until the photon either leaves the atmosphere, reaches the planetary surface (at which point it is assumed to be absorbed) or is scattered the maximum number of times, which has been tuned to 10. Increasing the number of scatterings does not lead to discrepancies in the model results by more than 1% for a wide range of planet-star geometries, planetary atmosphere types and for phase functions with scattering asymmetry parameters up to 0.95. Photons scattered more than 10 times are very unlikely to reach a distant observer because as the number of scatterings increases, the probability of being scattered into the same direction as the initial trajectory decreases.

The transmitted flux for a photon can be calculated by combining the path lengths through the atmosphere (either from Equation 2.1 or calculated from the ray tracing module) with the total absorption optical depth in each altitude layer. The scattering optical depth is not included in the transmittance calculations because it is used to determine the scattering events in the ray tracing module. This Monte Carlo ray tracing method is repeated over a wide range of wavelengths. Because of the computational time associated with ray tracing, and because scattering optical properties vary less with wavelength than those of gas absorption, the ray tracing module is not executed at all wavelengths in the line-by-line model. Instead, ray tracing results at one wavelength are applied for all comparable wavelengths. I determine what constitutes a comparable wavelength as follows. For the first wavelength for which optical properties are calculated by SMART, the model automatically runs the ray tracing module, and the altitude-dependent scattering and aerosol extinction optical properties, and phase function asymmetry parameters are stored for reference. For subsequent wavelengths, if either the optical properties of the aerosols or the phase function asymmetry parameters vary by more than 1% from the reference value, the ray tracing module is run again.

2.1.6 Generating Transit Light Curves

Refracted and scattered light from a planetary atmosphere can be deflected into the path to a distant observer, even when the planet is not in transit. This effect has been explored for in-transit (Hui and Seager, 2002) and out-of-transit refracted light (Sidis and Sari, 2010; García Muñoz *et al.*, 2012; García Muñoz and Mills, 2012), but not for scattered light. In this section I describe how to generate transit light curves for refracted and scattered light given the final trajectories from the ray tracing model.

For each photon, I trace the path back from the distant observer, through the atmosphere, and to the host star. I do this for all altitudes in the model atmosphere and along the annulus of the planetary atmosphere that is backlit by the star. Since I assume a spherically symmetric atmosphere, the model calculations for one model atmosphere are applicable all along the annulus of the planetary atmosphere. Figure 2.3 shows the geometry, projected into two dimensions, used for tracing photon paths back to the star. The transit is oriented so that the planet travels in the x direction and the y coordinate is fixed at b, the impact parameter. Note that this is the same as the global coordinates presented in Section 2.1.3, but with the global z direction pointing into the page in the projected coordinates. Let the angle along the annulus be ϕ, with ϕ=0 at the x-axis in the diagram, though since ϕ is integrated over, its reference point does not factor in to the final result. The final photon trajectory, as calculated by the ray tracing model, is given by θ and ψ.

The total distance traveled in the projected frame, R, can be calculated from θ. In the z coordinate, the photon will travel a distance of D, which is the planet-star distance. The magnitude of the distance traveled in the $x-y$ plane is $D\tan\theta$. It is useful to convert this distance into units of the stellar radius, R$_*$. This leads to the following expression for R:

$$R = \frac{D\tan\theta}{R_*} \tag{2.40}$$

$$R = \frac{\tan\theta}{\tan\alpha} \tag{2.41}$$

where α is the angular radius of the star. ψ is the azimuthal angle and, along with ϕ, determines the direction of the distance R. The geometry can be thought of in polar coordinates with radial coordinate $\frac{\tan\theta}{\tan\alpha}$ and polar angle $\psi+\phi$.

To determine the initial position of the photon relative to the stellar disk, I need to calculate the x and y coordinates for the photon. These are:

$$x = x_0 + R\cos(\psi+\phi) \tag{2.42}$$

$$y = b + R\sin(\psi+\phi) \tag{2.43}$$

with $R = \frac{\tan\theta}{\tan\alpha}$.

The total projected distance from the center of star is:

$$\begin{aligned} d^2 &= x^2 + y^2 \qquad (2.44) \\ d^2 &= x_0^2 - 2x_0 R\cos(\psi+\phi) + R^2\cos(\psi+\phi)^2 + b^2 - \end{aligned}$$

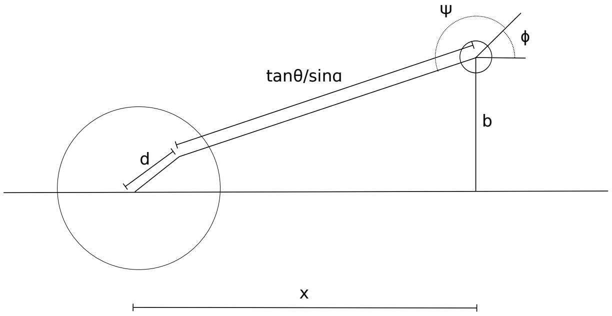

Figure 2.3: Geometry for calculating transit light curves. At each point *x* along the transit and at each point along the annulus of the planetary atmosphere, the trajectories calculated by the ray tracing model are traced through atmosphere and to the host star, or off of the stellar disk for paths that are physically impossible. From the final positions relative to the stellar disk, the total flux from each photon can be calculated. The total flux in the transit light curve at point *x* is the integral over all photon trajectories at each altitude layer in the atmosphere.

$$2bR\sin(\psi+\phi)+R^2\sin(\psi+\phi)^2 \tag{2.45}$$

If $d > 1$, then the path originated beyond the stellar disk, and no flux can be transmitted because the path was physically impossible and merely a consequence of the choice of a backwards Monte Carlo ray tracing model. If $d < 1$, the flux can be calculated using a limb darkening law. If no limb darkening coefficients are given, the default is that 100% of the flux is transmitted for any ray that originates on the stellar disk. The effect of ignoring limb darkening varies based on the type of host star and the wavelength observed at. For a Sun-like star at 0.4 μm, I find that limb darkening can decrease the out-of-transit observed flux by up to 5% when averaged over a half-transit length prior to ingress or subsequent to egress. The discrepancies are are large as 25% in the 1/100th of a transit length prior to ingress or after egress. For longer wavelengths, the discrepancies decrease, with just a 2% difference at wavelengths $>$1 μm averaged over half a transit length prior to ingress and a $\sim$10-15% difference in the 1/100th of a transit length just prior to ingress. For a 3500 K M dwarf star, the out-of-transit flux discrepancies are as great as 7% at 0.4 μm. The discrepancies introduced by ignoring limb darkening are at these levels for wavelengths up to ∼1 μm. For both the Sun-like star and the M dwarf, the in-transit discrepancies are ≤1% when averaged over the entire transit, and can be as large as 10% near ingress or egress.

The equations above are given under the assumption that the planet size is much smaller than the star size. If this is not the case, the x and y terms can be revised to include $R_p \cos(\psi + \phi)$ and $R_p \sin(\phi + \psi)$, respectively. However, even for planet sizes $\sim 1/10^{th}$ the size of the star, the effect of including R_p in the calculations is minimal, with the net result being a slight smoothing of the time-dependence of the flux signal.

2.2 Detectability Analysis

I performed detectability studies to determine the signal to noise ratios (SNRs) obtainable given a telescope and exposure time and to predict the required exposure time to detect spectral features. To estimate the noise in transit transmission spectra and light curves I used online exposure time calculators (ETCs) for JWST and E-ELT. (For more details on JWST, see Gardner *et al.* (2006), and for more details on E-ELT, see Gilmozzi and Spyromilio (2007)). The ETCs estimate the signal-to-noise ratio (SNR_{star}) of the star's flux given a wavelength of observation and the total exposure time. The noise level is, in ppm relative to the stellar flux, $10^6/\mathrm{SNR}_{star}$. The calculations were performed for stellar systems at a distance of 10 pc, except where otherwise noted, with stars ranging from F5V to M9V. The stellar parameters were obtained from Zombeck (1990) for the F, G and K stars and Reid and Hawley (2005) for the M dwarfs. The stellar spectra are Phoenix NextGen spectra (Hauschildt *et al.*, 1999).

The JWST ETC includes background noise from sky, dark, thermal, read-out and zodiacal light noise, though for all cases considered here the noise is dominated by photon noise. The E-ELT ETC includes background noise from continuum (sky-brightness), emission lines, atmospheric absorption and scattering, and thermal emission from the atmosphere and telescope. As with the JWST noise estimates, photon noise is the dominant component. The ETCs do not include noise from detector intrapixel variations (Deming *et al.*, 2009), but, in principle, calibration time could be devoted to mapping the pixels, as has been done with Spitzer Space Telescope Infrared Array Camera (Carey *et al.*, 2012). The assumption of photon-limited noise is optimistic, but noise levels within $\sim$20% of the photon noise limit have been obtained for transit transmission spectra with HST in spatial scan mode, wherein the target star is trailed during each exposure by telescope motion perpendicular to the direction of dispersion (Deming *et al.*, 2013; Wakeford *et al.*, 2013). Therefore, the detectability calculations performed here should be considered accurate to within $\sim$20%.

The total signal is the change in flux, in ppm. For absorption bands, this is the change in flux relative to the continuum. The continuum is assumed to vary linearly with wavelength across the band and is defined automatically by an algorithm that finds the maximum flux (minimum absorption) levels on either side of the band center within a user-input range of possible wavelengths. For signals due to broadband features, the signal is the difference between two spectra, which can be of different transits or spectra at different points within a transit.

The final signal to noise ratio (SNR) at each wavelength is the absorption signal divided by the noise calculated from the ETC, divided by $\sqrt{2}$. The total SNR is the square root of the sum of the squares of the SNRs calculated at all wavelengths. The factor of $\sqrt{2}$ must be included because the total noise will be the sum of the squares of the noise for the in-transit and out-of-transit spectrum. We assume the in-transit and out-of-transit noise levels are equal, so the SNR must be divided by $\sqrt{2}$. In practice, the in-transit and out-of-transit integration times do not need to be equal, so the calculations performed here would have to be adjusted when applied to a specific observation. For signals that are only observable for shorter amounts of time, the noise levels will increase by $\sqrt{\frac{1}{t}}$, where t is the observation time in terms of the total transit time.

2.3 Model Validation

2.3.1 Model Inputs

The model has been validated against observations in the solar system. Two validation experiments were performed that required spectral simulations. The first used solar occultation spectra collected by the Atmospheric Trace Molecule Spectroscopy (ATMOS) Experiment (Gunson *et al.*, 1990). ATMOS was designed to determine the volume mixing ratio profiles of minor and trace gases in the Earth's atmosphere. This was done by obtaining numerous solar occultation spectra through the limb of the Earth's atmosphere at wavelengths between 2 and 17 μm and by using a global retrieval algorithm to simultaneously retrieve volume mixing ratio profiles at all altitudes within each occultation (Irion *et al.*, 2002). The second validation source used is lunar eclipse observations (Pallé *et al.*, 2009). During a lunar eclipse, the sunlight that reaches the moon's surface traverses the Earth's atmosphere on limb trajectories and is refracted, producing a spectrum similar to a transit transmission spectrum.

The model atmospheres used for the validation experiments were customized to simulate the conditions observed at the time the validation data were recorded. To simulate synthetic spectra to match the ATMOS data, we used the ATMOS retrieved altitude-dependent gas mixing ratios and temperature profile (Figures 2.4 and 2.5). We used the average of the retrieved abundances of H_2O, CO_2, O_3, CO, N_2O, CH_4, O_2, NO_2, HNO_3, CFC-11, and CFC-12 for ATMOS occultations taken at latitudes between 40°-50°N. We used N_2-N_2 and N_2-O_2 absorption cross sections to model absorption near 4.3 μm (Lafferty *et al.* (1996); Eddie Schwieterman, personal communication, 2013 May 5.) Figure 2.4 shows the volume mixing ratio profiles for many of the gases included in the model runs as well the temperature profile. Figure 2.5 shows the volume mixing ratio profiles for NO_2, HNO_3, CFC-11 and CFC-12, which are primarily anthropogenic. We generated high resolution spectra over

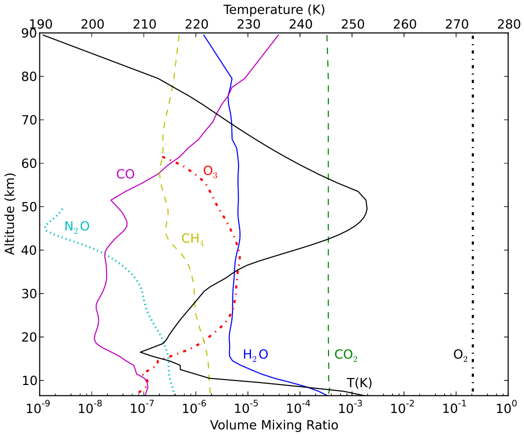

Figure 2.4: Temperature profile and gas volume mixing ratios used to generate model ATMOS spectra. The profiles are the averages of the ATMOS retrievals between 40-50° N.

the entire wavelength range, then convolved them with a triangle slit to a spectral resolving power of R=1000 when comparing the model spectra to the ATMOS data.

The model atmosphere developed for the lunar eclipse validation was based on the mid-latitude summer model atmosphere adopted for the Intercomparison of Radiation Codes in Climate Models (ICRCCM) (McClatchey *et al.*, 1972; Clough *et al.*, 1992). The temperature profile and volume mixing ratio profiles for this model atmosphere are shown in Figure 2.6. To produce an acceptable fit to the lunar eclipse spectra, which predominantly probe latitudes greater than 50°, we decreased the H_2O mixing ratio by a factor of two from the standard ICRCCM atmospheric profile to more accurately depict the expected H_2O mixing ratio profiles at those latitudes. Following the method of García Muñoz *et al.* (2012), we also assume any path with a tangent altitude of 6 km or less is opaque because of clouds. In addition to the vibration-rotation transitions for the the gases shown in Figure 2.6, we also included the “interaction-induced absorption” associated with collision-induced absorption bands and dimers for O_2-O_2 and O_2-N_2. We used the O_2-O_2 cross section from Greenblatt

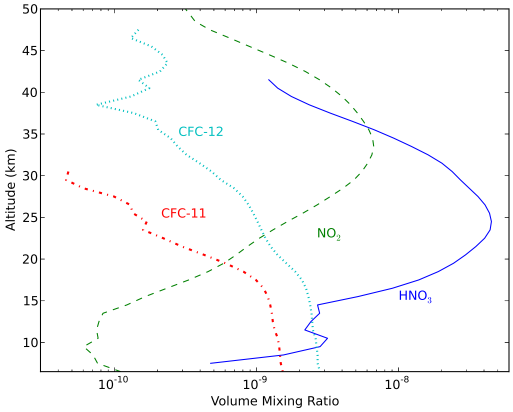

Figure 2.5: Average retrieved gas volume mixing ratios from ATMOS for HNO_3, NO_2, CFC-11 and CFC-12. These gases are predominantly from anthropogenic sources.

et al. (1990) and the O_2-N_2 cross section from Maté *et al.* (1999) to model absorption at 1.06 μm and 1.27 μm. As with the ATMOS spectra, we initially generated high resolution spectra, and then we convolved them with a triangle slit to match the resolving power of the lunar eclipse data (R∼1000).

We also included aerosol extinction in the lunar eclipse model atmosphere by using data from Sioris *et al.* (2010). They use the Atmospheric Chemistry Experiment (ACE) aboard Measurements of Aerosol Extinction in the Stratosphere and Troposphere Retrieved by Occultation (MAESTRO) to determine the amount and size distribution of aerosol particles in the atmosphere. We used their data from September, 2007 to model the lunar eclipse data because by September, 2008, the aerosol levels had dramatically increased due to the Kasatochi eruption in August, 2008. The lunar eclipse occurred 9 days after the eruption, which was not enough time for volcanic aerosols to be detectable (Bourassa *et al.*, 2010). We used a log-normal aerosol size distribution with a mean of 0.5 μm and a variance of 0.28μm^2, which we found to provide the best fit to the data and are consistent with the results from Sioris *et al.* (2010). However, we note that changing the mean to 0.4 μm or 0.6

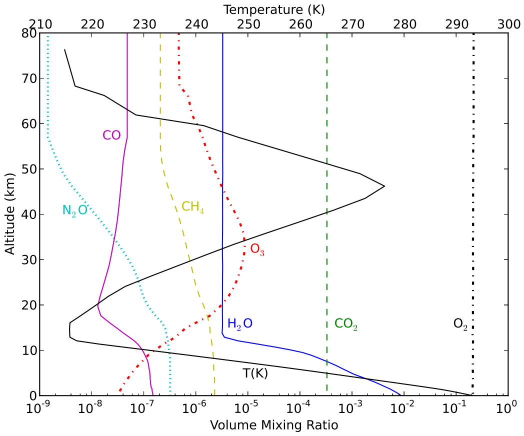

Figure 2.6: Temperature and mixing ratio profiles from the US standard summer northern mid-latitudes model atmosphere. We used this model atmosphere to generate lunar eclipse spectra and Earth-analog spectra. We note that for the lunar eclipse spectra we scaled down the H_2O mixing ratio by a factor of 2.

μm and letting the variance change by over an order of magnitude did not greatly increase our model validation errors. Our aerosol cross sections were calculated using a python version of the code `bhmie` (Bohren and Huffman, 1983)[1].

2.3.2 ATMOS Validation

We used the ATMOS sunset spectra from the ATLAS 3 space shuttle with latitudes between 40° and 50° taken between 1994 November 4-6[2]. The retrieved atmospheric properties were taken from the ATMOS version 3 retrievals described in Irion *et al.* (2002). The average signal to noise varies by spectral filter, with values of 74±11 for Filter 3 (2.9-6.3 μm), 98±35 for Filter 4 (2.1-3.2 μm), 122±40 for Filter 9 (4.1-16.7 μm), and 255±36 for Filter 12 (7.1-16.7 μm). The spectra were measured with a spectral resolution of $\sim$0.01 cm^{-1}

---

[1] Retrieved from Ray Pierrehumbert's 'Principles of Planetary Climate' website

[2] Data available at http://remus.jpl.nasa.gov/atmos/atmos.html

($R{\sim}10^6$ at 1.0 μm), but we applied a triangle filter to the spectra with a resolving power of 1000 when comparing the spectra to our model spectra to better show the systematic broadband differences.

Figure 2.7 shows a comparison of the ATMOS data with our model spectra. ATMOS data were taken over a wider range of altitudes than shown here, and the model can produce spectra at any given altitude, however, these results were shown for simplicity and consistency with previous work (Kaltenegger and Traub, 2009). Multiple data spectra are shown for each altitude. Table 2.1 shows the discrepancies between the ATMOS data and the model spectra. The listed errors are arithmetic means for all spectra shown in Figure 2.7. To quantify the discrepancies between model and data spectra we calculated root mean square (RMS) errors. We define the absolute RMS error as the RMS of the difference between the two spectra. We define the relative RMS error as the RMS of the difference divided by the data. The average and relative RMS errors are 4% and 6% for altitudes greater than 12 km, at which cloud and H_2O variability become important.

2.3.3 Lunar Eclipse Validation

We used the August 2008 lunar eclipse observations by Pallé *et al.* (2009) to validate our model. The data were taken between 20:54 UT and 22:16 UT on 2008 August 16 at the observatory of El Roque de los Muchachos in La Palma Island using the LIRIS instrument on the William Herschel Telescope. The spectral resolution and range were ~1000 and 0.9-1.5 μm for the observations we used for validation. During a lunar eclipse, the sunlight that reaches the moon's surface traverses the Earth's atmosphere on limb trajectories and is refracted, producing a spectrum similar to a transit transmission spectrum. The data are taken at different times throughout the transit with different angles between the Sun, Earth and Moon (the solar elevation angle) (García Muñoz *et al.* (2012), Enric Pallé, personal communication, 2012 April 28). The solar elevation angle (hereafter referred to as *e*, in

Table 2.1: Absolute and relative RMS errors for the model fits to the ATMOS data. The listed errors for each altitude are averaged over all the data sets available for that altitude. The data and model fit very well down to 12 km, at which point clouds and cloud variability increase dramatically.

ATMOS Data Validation Errors		
Height (km)	RMS Error (%)	RMS Fractional Error (%)
100	3.5	3.5
75	3.1	3.1
50	3.1	2.9
40	4.1	2.8
30	4.4	6.0
25	4.4	9.3
20	5.8	12.5
12	18.9	>100
Average ($\geq$ 20km)	4.0	5.7

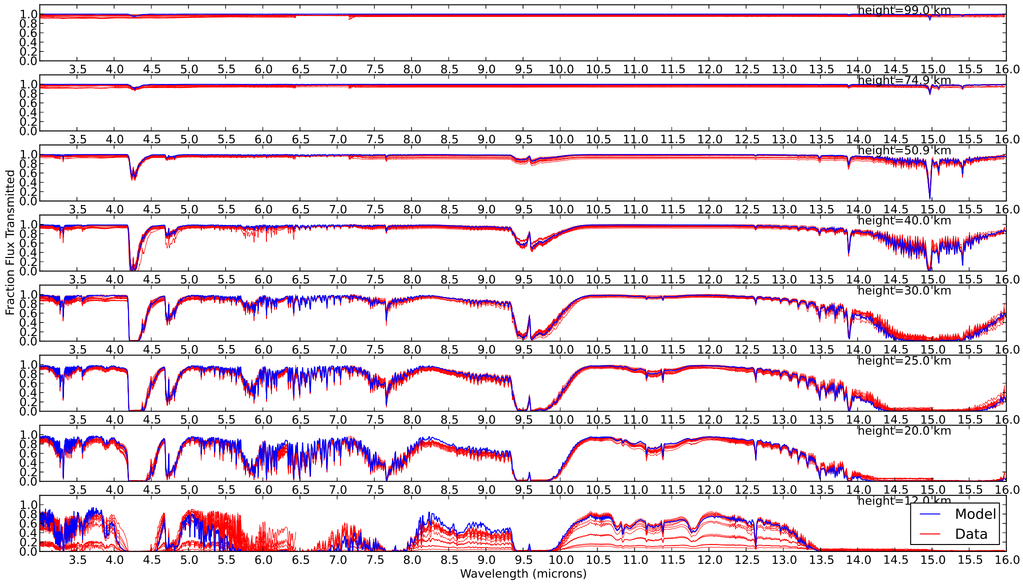

Figure 2.7: Altitude-dependent ATMOS spectra (red) and model spectra (blue). Multiple ATMOS spectra are shown for each wavelength band and altitude. The model and data agree very well except at altitudes of 12 km and below. At these altitudes, clouds become important and vary spatially and temporally, leading to a large amount of variation in the 12 km ATMOS data.

degrees) is the geocentric angle between the direction of incident sunlight and the direction of the moon from the Earth's center. The amount of refraction necessary for light from the Sun to reach the lunar surface is largest at greatest eclipse (at which e is at a minimum) and decreases as the Moon leaves greatest eclipse (as e increases). The change in the necessary angle of refraction leads to variations in the lunar eclipse spectrum as the eclipse progresses, with more flux from progressively greater altitudes in the Earth's atmosphere as e increases.

Figure 2.8 shows a comparison of the Pallé *et al.* (2009) lunar eclipse spectra and our model spectra. Table 2.2 shows the absolute and relative RMS errors between the model and data. The data and model spectra typically agree to within ∼10%. Figure 2.9 shows the altitudes that are probed at selected values of *e* (the angle between the Sun, Earth and the Moon) for the lunar eclipse spectra. The lunar eclipse spectra typically probe altitudes between 2 and 18 km, and only probe altitude between 1 and 11 km of the atmosphere near greatest eclipse.

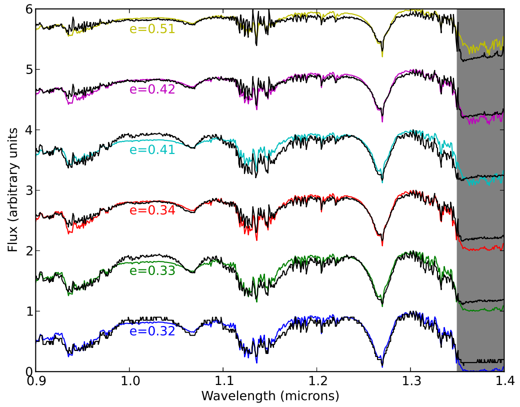

Figure 2.8: Lunar eclipse spectra (black) and our model spectra (colors) at various geometries denoted by the solar elevation angle, *e*, in degrees. The shaded region denotes wavelengths with low photon counts at which the data flux levels should be considered only upper limits. Our model fits the data with errors less than the intrinsic discrepancies in the data due to atmospheric spatial and temporal variability and any observational errors. We consider the fits to the lunar eclipse data to be a validation of the model, especially the refraction portion.

We compared our errors in modeling the lunar eclipse spectra to the inherent variations in the data. The lunar eclipse spectra vary due to changes in the solar elevation angle, *e*. For geometries with similar *e* values, the spectra should be nearly equivalent for a given atmospheric structure and composition. Therefore, in order to quantify the inherent variance in the lunar eclipse data, we calculated the absolute and relative RMS differences between spectra with close *e* values. We compared the following cases: *e*=0.32°, 0.33°, 0.34° and *e*=0.41° and 0.42°, and found that the average absolute and relative differences were 8.2%

Table 2.2: Absolute and fractional errors for the model fits to the Pallé *et al.* (2009) lunar eclipse observations. The intrinsic variability in the data corresponds to an absolute and fractional error of 8.3% and 14.4%, respectively. Our model spectra generally agree to the data within these errors, and on average our errors are less than the intrinsic variability.

Errors on Lunar Eclipse Fits		
e	RMS Error (%)	RMS Fractional Error (%)
0.32	5.8	10.5
0.33	7.1	12.2
0.34	5.1	9.2
0.41	9.0	18.4
0.42	5.0	7.1
0.51	5.2	7.1
Average	6.2	10.8

and 14.2%, respectively. These deviations are likely due to a combination of spatial and temporal variations in cloud coverage, aerosols, or gas mixing ratios and any observational errors. The lunar eclipse observations were taken at different times during the eclipse, such that different portions of the atmosphere were being probed as the Earth rotated and different cloud fields came into view. We used a single model atmosphere, so any spatial variations cannot be accounted for using our method. The average discrepancies of $\sim$8 and $\sim$14% are slightly larger than our errors from our model validation of 7% and 11%, so we consider our fit to the lunar eclipse spectra to a be a validation of the model, especially the refraction portion.

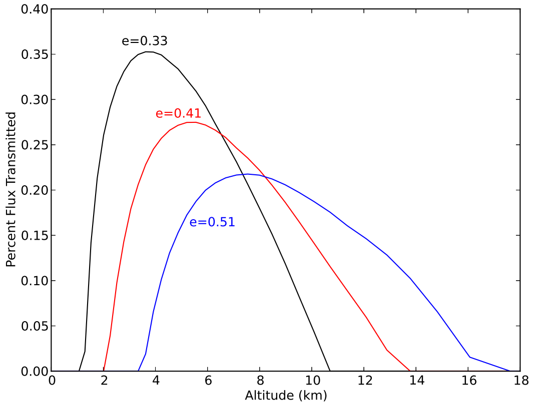

Figure 2.9: Maximum transmitted flux at each altitude for the lunar eclipse spectra at different solar elevation angles (*e*). The results shown here are for the shortest wavelengths, but the wavelength dependence of the transmitted flux at each altitude is small. For the lunar eclipse spectra near greatest eclipse (*e*=0.33), only the lowest 11 km of the atmosphere were probed, and at the furthest point from greatest eclipse (e=0.51) altitudes between 3 and 18 km were probed.

2.3.4 *Venus Scattering Footprint*

To specifically validate the scattering portion of the model, we calculated the scattering footprint of the Venusian atmosphere and compared it to other theoretical calculations and the scattering footprint of Venus Express Visible and Infrared Thermal Imaging Spectrometer (VIRTIS) in the near infrared. In contrast to our other scattering simulations, we modeled upwelling flux rather than flux transmitted on limb trajectories and other model predictions. We allowed up to 1000 scattering events for each photon for the model validation because photons can be scattered hundreds of times and still escape the atmosphere. We used the Crisp (1986) scattering parameters for the Venus cloud layers.

We use the backwards Monte Carlo model to simulate the photons that would reach an orbiting spacecraft or Earth-based observer. We find that the scattering footprint for 1.0 μm photons that escape through the clouds and hazes in the atmosphere from the surface have a standard deviation of 73 km and a full width half maximum 171 km. Within these limits, 70% and 95% of the energy is enclosed, respectively. This roughly agrees with previous theoretical estimates of 90 km (Hashimoto and Imamura, 2001) and 50-100 km (Moroz, 2002) and an estimate of the Venus Express surface resolution, which is $\sim$100 km (Smrekar *et al.*, 2010). Within 100 km, we find that 85% of the energy is enclosed, suggesting that our results are comparable to other estimates of the Venus scattering footprint. We find that photons are scattered $\sim$240 (mean) and $\sim$200 (median) times. 15% of photons emitted from the surface reach the top of the atmosphere, and the others are scattered back to the surface or are absorbed, which agrees with previous estimates from Hashimoto and Imamura (2001).

Chapter 3

THE EFFECTS OF REFRACTION ON TRANSIT TRANSMISSION SPECTROSCOPY: APPLICATION TO EARTH-LIKE EXOPLANETS

In this chapter I investigate the effects of refraction on transit transmission spectra and transit light curves using the model described in Chapter 2 for Earth-like atmospheres over a range of stellar types. In particular, I show that refraction greatly limits the detectability of spectral absorption features for Earth-like planets orbiting Sun-like stars, but has a relatively small effect for Earth-like planets orbiting M dwarfs. Refraction also leads to temporal variations, or changes in the transit light curve. Below, I examine how differences in these variations result in altitude-dependent spectra. I also calculate the detectability of spectral absorption features in the in-transit spectrum with and without refraction to show potential applicability to JWST. I find that absorption features in the altitude-dependent spectra will be difficult to detect with JWST, but that in-transit features from H_2O, CO_2, and possibly even CH_4 and O_2 may be detectable if 100's of hours of telescope time can be devoted to a single target. Portions of this chapter were originally published in collaboration with V. S. Meadows and D. Crisp in the 1 September 2014 issue of the *Astrophysical Journal* (Misra, Meadows, and Crisp, 2014, *ApJ*, Vol. 792, 61) and are reproduced below with permission of the American Astronomical Society.

3.1 Model Input Parameters

We modeled the effects of refraction in the atmospheres of Earth-like planets for a range of stellar types from G2V to M9V. For each star, we placed an Earth analog planet at the flux-equivalent distance, that is, the distance from the star at which it receives the same bolometric flux as the Earth does from the Sun today. We highlighted two test cases for our analysis of the effects of refraction and detectability studies: the Earth analog planet orbiting a Sun-like star and an M5V star. For the solar spectrum, we used a Kurucz model atmosphere (Kurucz, 1979). The other stellar spectra are Phoenix NextGen (Hauschildt *et al.*, 1999) model spectra, which include elemental and molecular lines . In particular, the M5V spectrum has a temperature of 2800 K, a log of surface gravity of 5.0, and solar metallicity.

The model atmosphere developed for simulating Earth-like exoplanets is the ICRCCM model atmosphere, and includes absorption from the gases shown in Figure 2.6 along with O_2-O_2, O_2-N_2 and N_2-N_2 absorption. The exoplanet model atmosphere does not include clouds or aerosol particles. We convolved our high resolution spectra to a resolving power of R=100, applicable to the *JWST* NIRSPEC (Near Infrared Spectrograph) instrument in single prism mode (Köhler *et al.*, 2005).

3.2 Results

3.2.1 Maximum Tangent Pressure for Exoplanets

Planetary atmospheres have index of refraction gradients which leads to the refraction, or deflection, of light. This refraction angle depends on the composition of the atmosphere, the pressure-temperature profile and the radius of the planet. For portions of the atmosphere with sufficiently large deflection angles, there will be no path originating at the host star that traverses the planetary atmosphere and can reach a distant observer, and these portions of the atmosphere will not be able to be probed by transit transmission spectroscopy. We define the maximum tangent pressure as the pressure at which 50% of the flux is transmitted, which is roughly when the deflection angle is greater than the angular radius of the host star as seen from the planet.

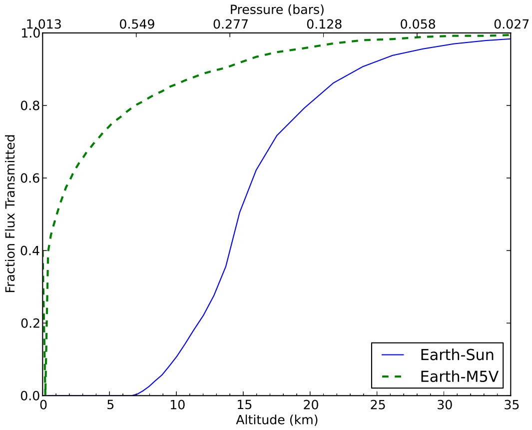

Figure 3.1: Maximum amount of transmitted flux at each altitude for an Earth analog orbiting a Sun-like star and an Earth-analog orbiting an M5V star. The maximum flux is set by refraction and is independent of atmospheric opacity. For the Earth-Sun case, the lowest altitudes cannot be probed and the maximum tangent pressure (defined as the pressure at which 50% of the flux is transmitted) is 0.3 bars. For the Earth-M5V case, almost all altitudes can be probed and the maximum tangent pressure is 0.9 bars.

We explored the effect of the angular size of the star (as seen from the exoplanet) on the maximum tangent pressure cutoff for transit transmission spectra by running three test cases: an Earth analog orbiting a Sun-like star (angular size of .54°), an Earth analog orbiting an M5V star (angular size of 2.2° measured from the exoplanet), and an Earth analog with no refraction (assuming a large enough angular size such that all pressures can be probed), with the resulting spectra shown in Figure 3.2. The maximum transmitted flux at each altitude, which is set by refraction, is shown in Figure 3.1. In the M-dwarf case, transit transmission spectroscopy can probe pressures as great as ∼0.9 bars (with a corresponding altitude of 1 km), while it can only probe up to ∼0.3 bars (14 km altitude) for the Sun-like star case. The difference in maximum tangent pressure for the two cases produces absorption features that are much stronger for the M-dwarf case.

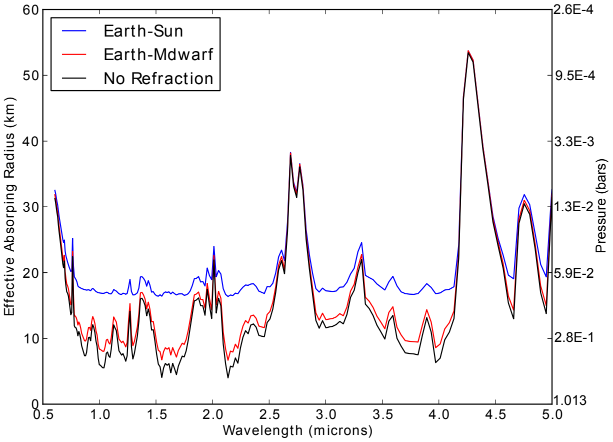

Figure 3.2: Comparison of transit transmission spectra for an Earth analog orbiting a Sun-like star (blue) and an Earth analog orbiting an M dwarf (red), along with an Earth analog with no refractive effects included (black). The *y* axis is the effective absorbing radius of the atmosphere (in km). As shown in Figure 3.1, the maximum tangent pressure that can be probed is ∼0.3 bars for the Earth-Sun analog and ∼0.9 bars for the Earth-M-dwarf system. This limit is set by refraction and leads to differences in the two spectra. Because it is possible to probe higher pressures for the M-dwarf case, the absorption features appear much stronger. Therefore, in general, planets orbiting M dwarfs should show stronger spectral signatures than planets orbiting more massive stars.

3.2.2 Temporal Variations Results

Figures 3.3-3.5 show how differences in the portions of the exoplanet atmosphere that are backlit (i.e., light is transmitted from the host star and through the exoplanet atmosphere to a distant observer) as a transit progresses can lead to temporal variations in a transit transmission spectrum of an exoplanet. These figures show the spectra for an Earth-analog planet orbiting a Sun-like star from half a transit length prior to ingress to center of transit. The colors in each figure correspond to a different stage of the transit. During the earliest stage (purple), only a small portion on the trailing (left) portion of the limb is backlit, as shown in Figure 3.3. The planet is not in transit yet, so most of the atmosphere is not backlit and the portions that are backlit are at altitudes ($\sim$2-15 km) at which the deflection angle is large enough that light from the far (right side) limb of the star is deflected into the beam to a distant observer. Most of the atmosphere is opaque, and therefore the flux transmitted through the atmosphere is small, as shown in Figure 3.4. The altitudes that are probed in this stage (and all other stages) are shown in the left-hand side of Figure 3.5. In the next two stages of the transit (cyan and yellow), the angle of deflection required for light to reach a distant observer is smaller than in the first (purple) stage, so the portions of the atmosphere that are backlit are at progressively greater altitudes ($\sim$5-17 km and 5-30 km, respectively).

After ingress (blue), all altitudes above $\sim$7 km are at least partially backlit and more flux is transmitted through the atmosphere. As shown in the left-hand side of Figure 3.5, the upper atmosphere is entirely backlit, but portions of the lower atmosphere are deflecting light out of the beam to a distant observer. As the planet reaches center of transit (green, then red), more flux can be transmitted at altitudes between 15 and 25 km, and slightly less flux is transmitted at altitudes between 10 and 15 km. The net result of these flux changes is that more flux is transmitted through the atmosphere, as shown in Figure 3.4. We note that at center of transit, no pressures greater than the maximum tangent pressure can be probed. However, prior to ingress (and after egress), it is possible to probe pressures greater than the maximum tangent pressure, and, in fact all the flux transmitted during the first stage (purple) is transmitted for paths with tangent pressures greater than the maximum tangent pressure.

The differences in the spectra as the planet moves through the stages of its transit can be used to obtain vertical sounding, or altitude-dependent spectra of the exoplanet. The right-hand side of Figure 3.5 shows the successive differences in the spectra at each stage of the transit, except for the first (purple) spectrum which is plotted as it would be observed, and can be considered the difference between the spectrum in the first stage and the spectrum well before the planet approaches ingress. We take the difference of the spectra to isolate a specific vertical region of the atmosphere. For example, the spectrum shown in yellow for the third stage is the difference between the spectrum for the third (yellow) and second (cyan) stage of the transit and corresponds to flux transmitted at tangent altitudes between 15 and 25 km. By looking at the differences in the spectra between each stage of the transit, it could be possible to retrieve altitude-dependent mixing ratios for gases in the exoplanet atmosphere.

It is possible to probe below the ‘maximum tangent pressure’ before ingress and after egress, but the pressures and altitudes that can be probed will be limited by the opacity and by critical refraction. Probing greater pressures (and therefore densities) in the atmosphere may be limited by Rayleigh scattering, gas absorption, or extinction from clouds and hazes. Paths will also be limited by critical refraction, in which a ray cannot leave the atmosphere because the index of refraction gradient is too great. This is a fundamental limit to the pressures can be probed, and often limits the depth that solar system radio occultations can probe (e.g., Fjeldbo et al., 1971). For an Earth-like planet, the layer of critical refraction is at a density of $\sim$4 times standard temperature and pressure (STP), which would be 11 km below the 1 bar level for a higher-pressure Earth-like atmosphere. While the long path lengths in transit transmission will likely limit the pressures that can be probed, criti-

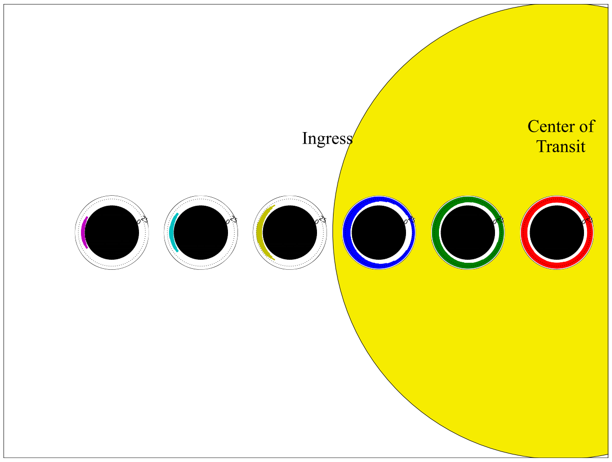

Figure 3.3: Diagram showing which altitudes can be probed at different times during a transit for an Earth-Sun analog. The colored regions correspond to regions of the atmosphere where light is transmitted, and the white regions are portions of the atmosphere that are opaque to a distant observer. The colors correspond to the spectra colors in Figures 3.4 and 3.5. Prior to ingress, only low altitudes in the atmosphere can be probed. As the planet moves from ingress to center of transit, more flux can be transmitted through progressively higher pressures (or lower altitudes) until the maximum tangent pressure is reached.

cal refraction may be the limiting factor for close-in planets (which typically have greater maximum tangent pressures) with very low opacity atmospheres.

Figure 3.6 shows the temporal variations for an Earth analog orbiting an M-dwarf. The variations correlate to differences at lower altitudes but have a greater overall signal. The absorption features are much deeper than for the Earth-Sun case because the flux differences correspond to lower altitudes or greater pressures being probed.

3.2.3 Detectability of Spectral Features

We calculated the S/N of spectral absorption features that could be achieved with the *JWST* NIRSPEC instrument, assuming all transits in the five-year lifetime of *JWST* could be observed. Figure 3.7 shows the noise levels for the Earth-Sun analog, Earth-M5V analog

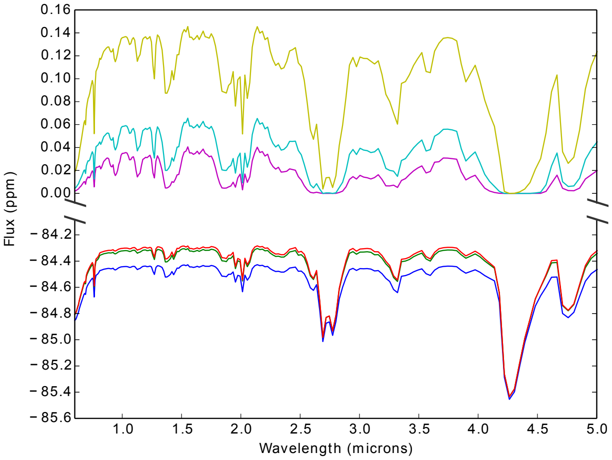

Figure 3.4: Time-averaged spectra for the out-of-transit (top) and in-transit (bottom) time periods illustrated in Figure 3.3 during a transit of an Earth-Sun analog. The spectra are shown in terms of ppm flux differences. The largest variability (besides ingress) is seen between ingress and one third of the way to center-of-transit. The upper scale has been expanded to better display the out-of-transit spectra.

and a flat continuum source. The noise levels vary with wavelength because the stellar fluxes are wavelength-dependent and also because the NIRSPEC sensitivity is wavelength-dependent. Table 3.1 shows the S/N and signal level for a number of spectral features for four test cases: the Earth-Sun analog and Earth-M5V analog, each with and without refraction. Many of the spectral features identified in the transit transmission spectrum of an Earth analog around an M5V star could be detected by *JWST* at the 3σ level or greater, assuming all transits in the 5 year mission lifetime are coadded. Table 3.1 shows that there are H_2O and CO_2 features with S/N ratios greater than seven. Furthermore, O_2 and CH_4, which together are considered a very strong biosignature (Lovelock, 1965), are detectable with S/Ns of $\sim$3 for the 1.27 μm O_2 band and the 2.3 and 3.3 μm CH_4 bands.

Our results generally agree with previous detectability calculations. Deming *et al.* (2009) find S/Ns for the 4.3 μm CO_2 band and H_2O bands between 1.7 and 3.0 μm were near 50 for habitable super-Earths at a distance of 10 pc. These S/N values are a few

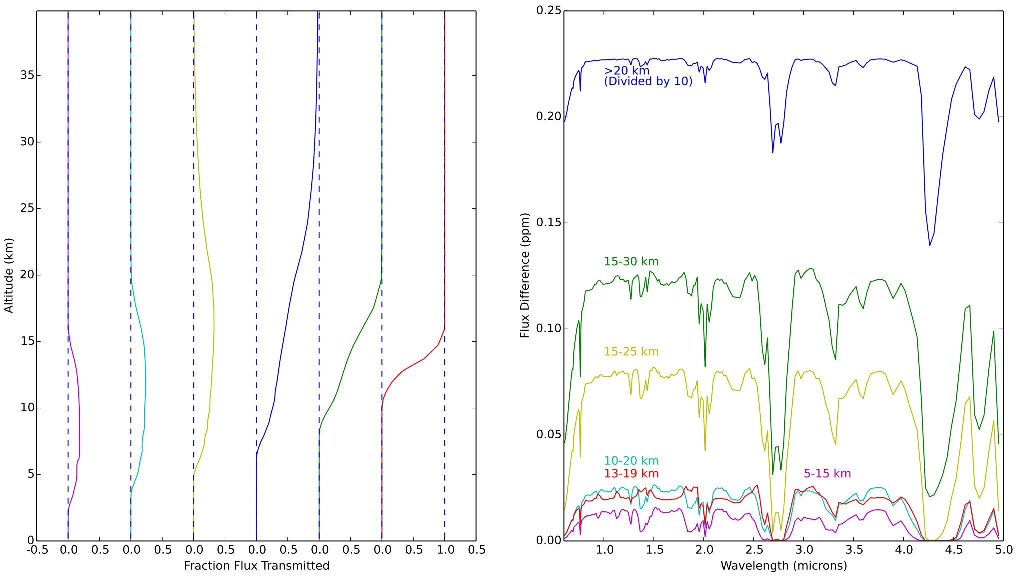

Figure 3.5: Altitude-dependent transmitted flux and spectra for an Earth-like planet orbiting a Sun-like star. Left: altitude-dependent transmitted flux from pre-transit to center of transit as deviations from the dotted line. Right: The purple spectrum is plotted as would be observed, and all other spectra show the spectrum of that stage with the previous stage's spectrum subtracted from it, e.g., the cyan spectrum shows the difference between the spectrum in the cyan and purple stages. The six stages correspond to the stages and colors shown in Figure 3.3. Taking the difference between the spectra at each stage allows us to isolate a specific vertical region of the atmosphere, permitting vertical sounding of the atmosphere.

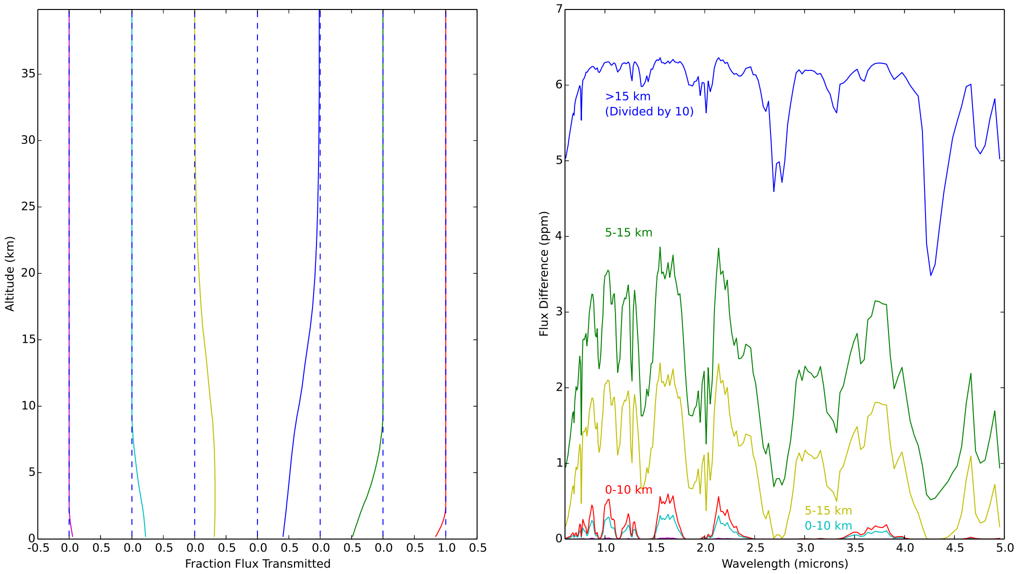

Figure 3.6: Same as Figure 3.5, but for an Earth analog orbiting an M dwarf. The differences in flux occur at higher pressures than for the Earth-Sun case because transit transmission can probe higher pressures for the Earth-M-dwarf case.

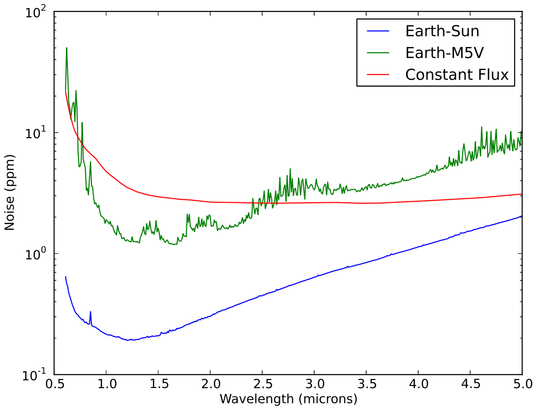

Figure 3.7: Noise estimates (in ppm) for an Earth-Sun analog, an Earth-M5V analog, and a flat continuum source of 5 $\times 10^{-}11$W m^{-2} μm^{-1}. The exposure times are 234,000 s for the Earth-Sun case and 1,000,000 s for the others.

times higher than what we have found, but our calculations were done for an Earth-like atmosphere, while theirs were done for super-Earths with different compositions, some of which had greater amounts of H_2O and CO_2 than the Earth. Kaltenegger and Traub (2009) find much higher S/N values for their Earth-analog calculations, but we note that they do not include accurate noise estimates for *JWST* and do not include a factor of $\sqrt{2}$ in their calculations for the noise added when differencing in-transit and out-of-transit observations. Belu *et al.* (2011) find an S/N of between 5 and 10 for the 4.3 μm CO_2 band for a super-Earth, which is consistent with what we find for a true Earth analog.

Refraction limits the detectability of spectral absorption features for all cases examined here, with a greater effect for Earth-like planets orbiting Sun-like stars. For the Earth-M5V case, refraction leads to a decrease in the predicted S/N by an average of ∼10% for all spectral features and ∼15% for H_2O features. However, for the Earth-Sun case, refraction leads to an average decrease in the S/N by ∼60% for all features and ∼75% for H_2O features. We have further quantified this effect in Figure 3.8, which shows the fractional increase in

Table 3.1: Signal levels (in ppm) and signal to noise ratio (S/N) for molecular absorption features for four different test cases, for the Earth-Sun analog and the Earth-M5V analog, each with and without refraction included. The calculations were done assuming that all possible transits are observed in JWST's 5 year mission lifetime.

		With Refraction				No Refraction			
Absorption Feature		Earth-Sun		Earth-M5V		Earth-Sun		Earth-M5V	
Molecule	λ (μm)	S/N	S	S/N	S	S/N	S	S/N	S
O2	0.69	0.1	0.0	0.0	1.1	0.1	0.0	0.1	1.2
O2	0.76	0.4	0.1	0.4	6.2	0.7	0.3	0.5	6.7
O2-O2	1.06	0.0	0.0	0.9	2.0	0.4	0.1	1.2	2.7
O2	1.27	0.3	0.1	2.9	5.1	0.9	0.2	3.3	5.9
O3	4.70	0.2	0.6	1.6	18.5	0.3	0.8	1.7	19.3
CO2	2.00	0.7	0.3	7.5	19.7	2.1	0.9	8.7	22.8
CO2	2.70	1.5	1.1	7.5	33.7	1.9	1.4	7.8	34.9
CO2	4.30	1.0	1.9	7.4	58.4	1.3	2.4	7.8	61.0
CH4	2.30	0.2	0.1	4.3	12.0	1.0	0.6	5.1	14.6
CH4	3.30	0.3	0.3	3.5	17.2	0.7	0.8	3.8	18.9
H2O	0.90	0.1	0.0	2.0	6.2	1.0	0.3	2.5	7.9
H2O	1.10	0.1	0.0	2.6	5.2	0.9	0.3	3.1	6.3
H2O	1.40	0.6	0.2	6.6	15.6	2.5	0.7	7.9	18.3
H2O	1.90	0.4	0.2	6.6	16.3	2.0	0.8	8.0	19.6
H2O	2.70	0.4	0.3	2.9	12.3	0.8	0.5	3.1	13.2

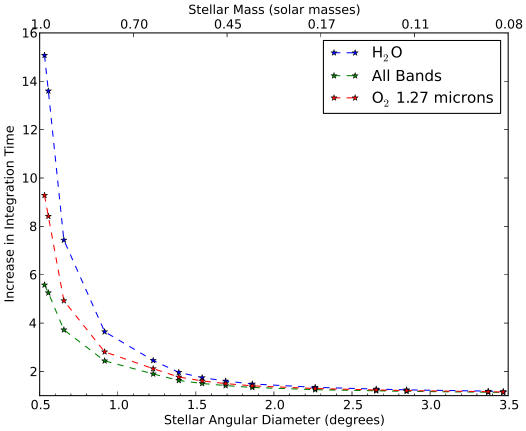

Figure 3.8: Fractional increase in integration time required to achieve the same S/N for absorption features in a refracted spectrum compared with a non-refracted spectrum versus the angular diameter of the star from the Earth analog's perspective. The stellar masses given on the top *x* axis are the mass of the star for a given angular diameter assuming the Earth analog is orbiting at a flux-equivalent distance, or the distance where the top of atmosphere incident flux is 1373 W m^{-2}. Molecules that are concentrated at the lowest altitudes, such as H_2O and dimer molecules, are the most affected by the cutoff set by refraction.

integration time required to obtain the same S/N for spectral features in a refracted spectrum compared to a non-refracted spectrum as a function of the angular diameter of the star from the planet's perspective. We find that molecules that are concentrated at the lowest altitudes, such as H_2O and O_2 dimer molecules, would require the greatest increase in integration time to be detected for the refracted model spectra. Evenly mixed molecules (like CO_2 and O_2) and molecules concentrated in the stratosphere (O_3) typically require lower increases in integration time. For all molecules, planets orbiting M-dwarf stars require the smallest increases in integration time because almost the entire atmosphere can be probed. In contrast, a factor of 16 increase in integration time would be required to detect multiple H_2O absorption features in the spectrum of an Earth-like planet orbiting a Sun-like star because pressures greater than $\sim$0.3 bars cannot be probed due to refraction.

Observations with *JWST* will not have sufficiently low noise to obtain vertical soundings for an Earth-like planet. The S/Ns for even the strongest features in any of the temporally varying spectra are no greater than $\sim$1.7 for the Earth-M5V case and far lower for the Earth-Sun case. However, we find that by integrating over all wavelengths, it may be possible to detect broadband temporal variations due to refraction with S/Ns of 4.6 (out of transit) and 8.1 (in transit) for the Earth-M5V case and 1.5 (out of transit) and 2.3 (in transit) for the Earth-Sun case. The out-of-transit broadband refracted light signal would be an increase in flux just prior to ingress and subsequent to egress in the transit light curve, while the in-transit refracted light signal would be an increase in flux from ingress to center of transit, then a decrease from center of transit to egress. While detecting broadband variations would not reveal anything about the vertical mixing ratio profiles of atmospheric gases, it could potentially be used to estimate the altitudes that can be probed in transit transmission. A more detailed exploration of this concept is presented in Chapter 4.

3.3 Discussion

As described in Section 3.2.1, the maximum tangent pressure that can be probed is greater for larger apparent angular stellar sizes. For the exoplanets whose transit transmission spectra have been recorded to date, the maximum tangent pressures have been large (typically $\geq$ 10 bars) due to the small planet-star distances (and thus large apparent stellar diameters). At these pressures, all atmospheres should be opaque due to collision-induced absorption or pressure broadening, suggesting that all optically thin paths will be largely unaffected by refraction. Therefore, the effect of refraction is small for most observations of very close-in planets, such as hot Jupiters of hot Neptunes.

The maximum tangent pressure can influence how observable a biosignature could be for an exoplanet. As shown in Figure 3.2, Table 3.1 and Figure 3.8, absorption features for a habitable planet orbiting an M dwarf are much stronger than for a habitable planet orbiting a Sun-like star because most of the atmosphere can be probed for an Earth analog orbiting an M dwarf, while only pressures less than 0.3 bars can be probed for an Earth analog orbiting a Sun-like star. This also has implications for potentially habitable planets orbiting white dwarfs. Planets in the habitable zones of white dwarfs could show very strong transit transmission signals (Agol, 2011). Additionally, white dwarfs have similar temperatures to the Sun, and the angular diameter of the white dwarf for a planet in the habitable zone is roughly the angular diameter of the Sun from the Earth's perspective. Loeb and Maoz (2013) find that five hours of *JWST* integration time are required to detect the O_2 *A* band on an Earth-like planet orbiting in the habitable zone of a white dwarf, but because of refraction we calculate that the integration time will increase by as much as a factor of six for detecting the O_2 *A* band for Earth analogs orbiting white dwarfs.

We demonstrate how temporal variations in a transit transmission spectrum can be used to obtain vertical sounding in exoplanet atmospheres (see Figures 3.3-3.5). Vertical sounding in an exoplanet atmosphere can provide a wealth of information relevant to atmospheric structure. Vertical profiles of gas mixing ratios can reveal whether or not a gas is evenly mixed in an atmosphere. Unevenly mixed gases, such as CH_4, O_3, and H_2O in Earth's atmosphere, can provide information about surface fluxes, photochemistry, UV shielding, and the presence of a cold trap, or a layer in the atmosphere at which water condenses and forms clouds. *JWST* will likely not be able to use the techniques described here to obtain vertical sounding of an Earth-like exoplanet at 10 pc, as the S/Ns for these features are all below two (see Section 3.2.3). Therefore, these types of observations will not be possible until noise levels of a few times lower than those shown in Figure 3.7 can be achieved, which would require a larger ground or space-based observatory.

Starspots and other forms of stellar variability could produce temporal variations in a transit transmission spectrum that could mimic the refractive signatures described in Section 3.2.2. As a transiting exoplanet passes over a starspot, the total amount of flux blocked from the planet decreases because starspots tend to be cooler than the stellar photosphere. This leads to a reduction in the occulted flux. Similarly, refraction leads to an increase in flux, or decrease in absorption, as the planet nears center of transit. For the out-of-transit variations, a starspot setting on the stellar limb could potentially lead to an increase in flux just prior to ingress or just subsequent to egress, which would mimic the signal predicted from our refraction model. For either the in-transit or out-of-transit variations, the wavelength dependence of the variations could be used to distinguish between refraction and stellar variability because variations due to refraction will exhibit spectral absorption features from the planetary atmosphere (see Figures 3.4 and 3.5B). In comparison, starspot spectra are similar to blackbodies with effective temperatures lower than that of the rest of the stellar photosphere. Therefore, the wavelength dependence of the temporal variations could be used to distinguish between stellar variability and a signal due to refraction, potentially even with observations in two broadband filters if necessary.

Refractive effects will also be more repeatable than those of stellar variability. Starspots have limited lifetimes and will rotate in and out of view. The rotation periods of planet-hosting stars are on the order of days, and longer for M dwarfs (McQuillan *et al.*, 2013; Nielsen *et al.*, 2013). For the cases considered here, the transit duration is on the order of hours and the transit periods are typically tens of days for planets orbiting M dwarfs and hundreds of days for planets orbiting earlier-type stars. Because the transit duration is generally much shorter than the stellar rotation period, the starspot pattern on a star will be relatively static over the course of a transit and will unlikely be able to produce temporal variations similar to out-of-transit variations due to refraction. Furthermore, the starspot pattern on a star will be different for each transit, making it improbable that temporal variations due to stellar variability would be seen over multiple transits. On the other hand, variations due to refraction should be constant between transits, such that the repeatability of the variations could aid in distinguishing between stellar variability and refractive effects.

Chapter 4

DISCRIMINATING BETWEEN CLOUDY, HAZY AND CLEAR SKY EXOPLANETS USING REFRACTION

Planets with high-altitude clouds or hazes have been shown to be common and very difficult to characterize in transit transmission spectroscopy. It is currently difficult to know a priori whether or not a planet will be hazy or haze-free, such that a significant amount of telescope time must be devoted to a target planet before even a rough determination can be made concerning hazes. In this chapter, I present a way to distinguish between hazy and haze-free (and potentially cloudy and cloud-free) planets using refraction. Refraction leads to an increase in flux prior to ingress and subsequent to egress. I show that a detection of refracted light in the out-of-transit light curve is indicative of a haze-free atmosphere. I find that this effect could be detectable with $<$10 hr of JWST time for Jovian planets and $<$10 hr of E-ELT time for Earth-sized planets for planetary equilibrium temperatures roughly between 200 and 500 K. This technique could provide a relatively rapid means to characterize an exoplanet as hazy or haze-free and therefore identify targets most favorable for extended follow-up observations. Portions of this chapter were originally published in collaboration with V. S. Meadows in the 1 November 2014 issue of the *Astrophysical Journal Letters* (Misra and Meadows, 2014, *ApJL*), Vol. 795, L14 and are reproduced below with permission of the American Astronomical Society.

4.1 Introduction

Hazy transiting planets have been shown to be difficult to characterize, even in extended transit transmission observations (Kreidberg *et al.*, 2014). Therefore, it would be beneficial to have a method to distinguish between hazy and haze-free planets before significant amounts of telescope time are used to obtain a flat, featureless spectrum. Benneke and Seager (2013) propose that measurements of absorption wing steepness, or a comparison of the depths of multiple absorption bands, could be used to distinguish between cloudy/hazy and clear sky planets. Since both methods require relatively detailed characterization of absorption features, these techniques may not discriminate between a hazy and haze-free planet before considerable amounts of telescope time are used. In contrast, the refractive signal could be detected in the absence of absorption features, and the signal could be binned over a wide range of wavelengths, increasing detectability. While refraction can set a mid-transit maximum transit pressure (or minimum tangent altitude) that can be probed by transit transmission spectroscopy (García Muñoz *et al.*, 2012; Bétrémieux and Kaltenegger, 2014) refraction provides the deepest probe of an atmosphere pre- and post-transit (see Chapter 3) when it also generates a refractive halo around the exoplanet, increasing the observed flux (Sidis and Sari, 2010; García Muñoz *et al.*, 2012; García Muñoz and Mills, 2012). Sidis and Sari (2010) derive analytic expressions for the halo brightness for both transparent atmospheres and atmospheres with extinction from Rayleigh scattering. García Muñoz *et al.* (2012) and García Muñoz and Mills (2012) examine the concept further by generating spectra of refracted light for the Earth and for Venus.

Here, I expand on previous work by showing that a detection of refracted light in a transit light curve pre-ingress and post-egress would preclude hazy atmospheres, because hazes tend to obscure the layers of the atmosphere that refract light to a distant observer. I show that this signal could be more readily detectable than spectral absorption features in some cases and could be valuable for selecting targets for more extended follow-up observations.

4.2 Methods

We quantified the signal of refracted light as the difference in the average value of the transit light curve between two stages of the transit event. We chose a quarter of a transit length as the time bin to maximize the signal-to-noise ratio (S/N) for the majority of cases we examined. As can be seen in Figure 4.1, most of the refracted flux is seen in the quarter of a transit prior to ingress, so dividing the transit into longer stages would reduce the time-averaged signal. Stages with shorter durations could increase the time-averaged signal, but would have greater noise levels because of the shorter integration time. Refracted light brightness is more strongly peaked just outside of transit for planets with equilibrium temperatures (T_{eq}, see Borucki *et al.* (2011) for definition) $>$600 K, but we find that even for these cases adopting a time bin of 5% of the transit length results in poorer S/N for T_{eq} $<$600 K and an increase in S/N by only a factor of $\sim$2 for planets with greater temperatures

We used a suite of planetary atmospheres to calculate the refracted light signal. These are shown in Table 4.1. We have selected a combination of solar system analogs as well possible super-Earth and mini-Neptune atmospheres to cover a wide range of potential planetary atmospheres. We assumed the H_2-dominated atmospheres have a solar H/He ratio (90% H, 10% He) for simplicity, but the small change in the refractive index for different H/He ratios should have a negligible effect on our results. For the super-Earth and mini-Neptune planets, we ran our models on four test cases to span the most likely bulk atmospheric compositions: 100% N_2, solar composition, 100% H_2O, and 100% CO_2.

Out-of-transit refracted light must be deflected by a large enough angle to be directed into the beam to a distant observer. The characteristic angle of deflection (in radians) is $\sim R_*/d$, (where R_* is the stellar radius and d is the planet-star distance) which is also half the angular size of the star, as seen by the planet. For example, half a transit length prior to ingress on the trailing side of the planet, light originating at the near and far limbs of the star would have to be refracted by R_*/d and $3R_*/d$ respectively, to reach a distant observer. More

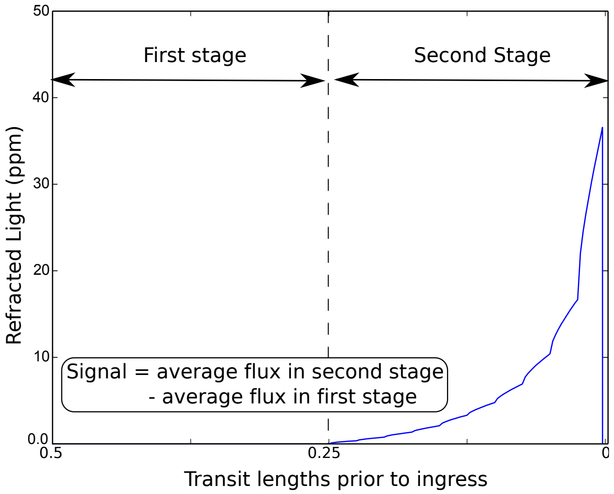

Figure 4.1: Pre-transit light curve for a 300 K Saturn-analog orbiting a Sun-like star from half a transit length prior to ingress up until ingress. Refraction leads to an increase in flux prior to ingress (and subsequent to egress by symmetry). This particular case gives the greatest peak brightness for all cases orbiting Sun-like stars. We define the signal of refracted light as the average flux level in stage 2 (just prior to ingress) minus the average flux level in stage 1.

than half a transit length prior to ingress, the required refraction angles would increase, and closer to ingress they would decrease.

Based on the qualitative description given above, the brightness of the refracted light signal depends on the angles of refraction at each altitude in an atmosphere and the planet-star geometry. The deflection of light by a planetary atmosphere can be calculated by our model from the atmospheric scale height, the planetary radius (R_p), and the index of refraction of the atmosphere. For each test case, R_p and the refractive index are given. The scale height is determined from the surface gravity, mean molecular weight of the atmosphere, and T_{eq}. Surface gravity is given for each test case, and the mean molecular weight is determined by the composition. We ran our model simulations over a grid of isothermal atmospheres with T_{eq} from 100 to 1000 K, covering a wide range of atmospheric scale heights. We chose to use isothermal atmospheres for simplicity after testing other temperature profiles with realistic tropospheric lapse rates and stratospheric temperature inversions and finding no significant difference in our results. The planet-star geometry is determined by R_p, R_*, the impact parameter (b), and d. The impact parameter is the sky-projected distance at conjunction, in units of stellar radius (Winn, 2011). To cover the full range of planet-star geometries, we ran our simulations over a range of values for b, planetary albedo, and stellar types from M9 to F5, constraining the stellar radius and luminosity.

Because the model simulations presented in this chapter do not explicitly calculate the effect of cloud and aerosol opacity, we simulated the effect of a cloud or haze layer by truncating the depth of the measurable atmosphere at a characteristic pressure layer. To determine appropriate pressure cutoff layers for the three main aerosol cases under consideration, we used our modeling results and examples of clouds and hazes in our own solar system to select pressure cutoffs at 1 bar (clear sky case), 0.1 bars (cloudy case), and 1 mbar (hazy case). We chose 1 bar as our clear sky pressure cutoff because at pressures $\geq$1

Table 4.1: Planetary Atmosphere Test Cases

Planet Type	Radius (km)	Composition	Refractive Index at STP	Surface Gravity (m s^{-2})
Earth	6371	N_2	1.00029	9.8
Super-Earth	12742	N_2	1.00029	9.8
Mini-Neptune	12742	H_2	1.00012	9.8
H_2O Super-Earth	12742	H_2O	1.00026	9.8
CO_2 Super-Earth	12742	CO_2	1.00044	9.8
Neptune	24622	H_2	1.00012	11.1
Saturn	58232	H_2	1.00012	10.44
Jupiter	69911	H_2	1.00012	24.8

bar, our modeling indicates that atmospheres within the range of compositions under consideration are optically thick near 1 μm (the central wavelength for our transit simulations) when only Rayleigh scattering is included. For the pressure cutoff for cloudy atmospheres we chose 0.1 bars, which is a characteristic lower pressure limit for the tropopause for atmospheres of a range of different compositions (Robinson and Catling, 2014), and the majority of clouds are found within a planet's troposphere. Lastly, we chose 1 mbar as the hazy pressure cutoff because hazes are typically generated via photochemistry in the upper atmosphere at pressures near 1 mbar. For example, at 1 μm Venus is optically thick (τ=1) in transit transmission at 90 km ($\sim$0.1 mbar) (Ehrenreich *et al.*, 2012) and Titan is optically thick at $\sim$240 km ($<$0.5 mbar) (Bellucci *et al.*, 2009). Because hazes form at pressures $<$1 mbar in both a warm CO_2-dominated atmosphere and a cold N_2-dominated atmosphere, we chose 1 mbar as a reasonable cutoff for hazes over the parameter space we explore here.

4.3 Results

Table 4.2 shows the ppm flux change, the required integration time, the number of transits and the total time (from first transit to last) for detecting refracted light for each test case over the suite of parameters. The results shown here are for an albedo of 0.15, but results for other albedos are available online[1]. Our results indicate that Saturn analog planets exhibit the most detectable refracted light of any of the cases because Saturn has a radius close to Jupiter's radius and a lower surface gravity, which increases the atmospheric scale height at a given temperature. The amplitude of the refracted light signal (as defined in Section 4.2) is no larger than half a scale height for all cases we have explored here. The maximum flux amplitude for planets orbiting Sun-like stars is 10 ppm for a 300 K Saturn analog. The other H_2 cases have maximum amplitudes of 6, 4, and 2 ppm for the Jupiter, Neptune, and Mini-Neptune cases, respectively. The greatest ppm signals are for planets orbiting around M9V stars, for which the signals can increase by nearly two orders of magnitude to 950 ppm for a 200 K Saturn analog.

Figure 4.2(a) shows the JWST out-of-transit integration time required to detect refracted light for the four H_2-dominated atmospheres: Jupiter, Saturn, Neptune analogs, and the "mini-Neptune", all without clouds or hazes. For many of the Saturn and Jupiter-analog cases, refracted light could be detected in $<$10 hr of JWST time. This integration time can be achieved in 1 transit for Jupiter and Saturn-analog planets with T_{eq} $<$600 K orbiting F, G, and K stars, and in $<$5 transits for T_{eq} $<$400 K orbiting M dwarfs. For cases in which multiple transits are required, the total time from first transit to last is $<$1 year, and typically $<$6 months. Figure 4.2(a) shows our results for an impact parameter (b) of 0.0, with observing times required increasing by 1% for b=0.2, 10% for b=0.6, and 30% for b=0.9.

Figure 4.2(b) shows the E-ELT integration time required to detect refracted light for

---

[1] `http://iopscience.iop.org/2041-8205/795/1/L14/fulltext/apjl502896t2_mrt.txt`

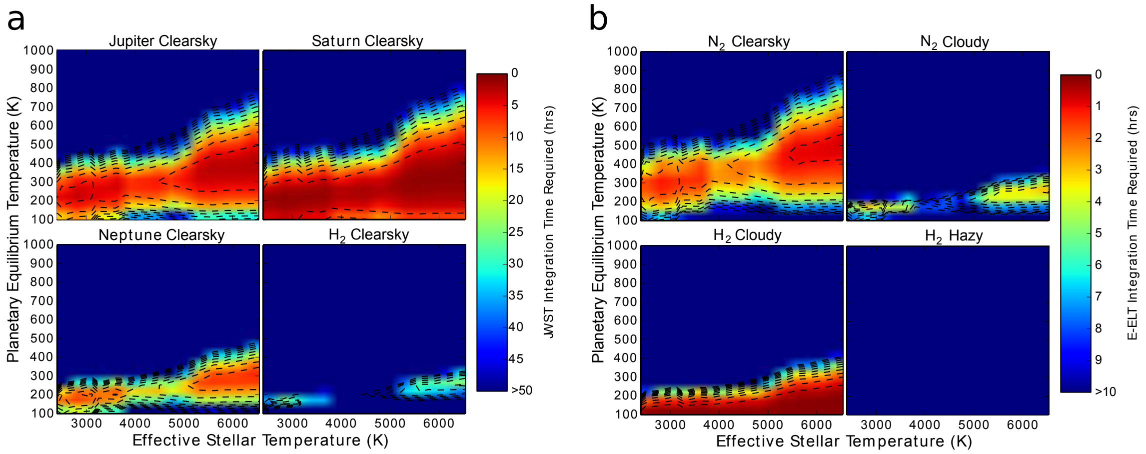

Figure 4.2: (a) JWST integration time required to detect refracted light for H_2-dominated atmospheres. The results assume that observations are made at 1 μm with R=100, for a planet at a distance of 10 pc. The planets with the most detectable refracted light signal are those with $T_{eq} < 600$ K for solar-type stars and < 400 K for M dwarfs. For many Jupiter and Saturn-analog cases, refracted light could be detected with <10 hours of JWST time. (b) E-ELT integration time required to detect refracted light for N_2 and H_2 atmospheres, assuming that 50 wavelength bins can be summed over at R=100. Refracted light is most detectable for the non-hazy atmospheres, and therefore could be used to distinguish between hazy and non-hazy worlds.

super-Earth and mini-Neptune atmospheres with b=0.0. We calculated the signal levels for N_2, H_2O, CO_2, and H_2 atmospheres, but only a comparison of N_2 and H_2 atmospheres is shown here. We find that refracted light could be detectable in <10 hr of E-ELT time for many of the clear sky atmospheres, and even some cloudy atmospheres. In contrast, detecting refracted light for a hazy exoplanet would require >100 hr for all the planetary atmospheres we considered. Here we have assumed that it is possible to bin over at least 50 spectral resolution elements. The justification for this is found in Figure 4.3, which shows the wavelength-dependent refracted light signal for 2 $R_\oplus$ planet with an Earth-like atmosphere. A larger change in effective radius at a given wavelength means a stronger flux from refraction prior to ingress or after egress. Between 0.8 and 1.35 μm - shortward of a major H_2O absorption feature and where Rayleigh scattering opacities are small - there are $\sim$50 spectral resolution elements that could be summed. For Earth-analog atmospheres, there is a relatively large flux difference at all these wavelengths. Therefore, we consider binning over multiple spectral resolution elements to decrease the integration time to be a valid approach, at least for N_2-dominated planets like Earth.

The greatest amplitude of refracted flux for the N_2 Super-Earth cases around a Sun-like star is 0.12 ppm for a 400 K planet. For the cloudy case, the maximum amplitude is 0.06 ppm at 200 K. The cloudy H_2 cases have amplitudes between 0.2 and 1.0 ppm, but only for the very cold ($<$200 K) cases. The amplitudes for the hazy H_2 cases are all below 0.025 ppm, and below 0.005 ppm for $T_{eq} >$150 K. The number of transits required to detect refracted light with E-ELT is 1 for clear sky N_2 Super-Earths with $T_{eq} <$800 K orbiting F, G, and K stars, and $<$3 for $T_{eq} <$500 K for those orbiting M dwarfs. As with the Jupiter and Saturn analogs, 3 transits is, from the first transit to last, much less than a year and typically $<$3 months. Cloudy atmospheres with $T_{eq} <$250 K could exhibit detectable refracted light signals, but hazy atmospheres have largely undetectable refracted light signals except for some very cold (T_{eq}=100 K) cases.

4.4 Discussion

The detection of refracted light is easier in haze-free atmospheres, where the transmitted flux can penetrate to pressure levels where refraction is stronger (see Figure 4.2(b)). However, discriminating between cloudy and hazy worlds could be more challenging. For example, for a 600 K N_2 Super-Earth orbiting a Sun-like star (and for the majority of parameter space), a null detection of refracted light would be consistent with either a cloudy or hazy atmosphere, with no apparent way to differentiate between the two. On the other hand, for a 250 K N_2 Super-Earth orbiting a Sun-like star, both the clear sky and cloudy cases are consistent with a detection of refracted light. To clarify these results, one would

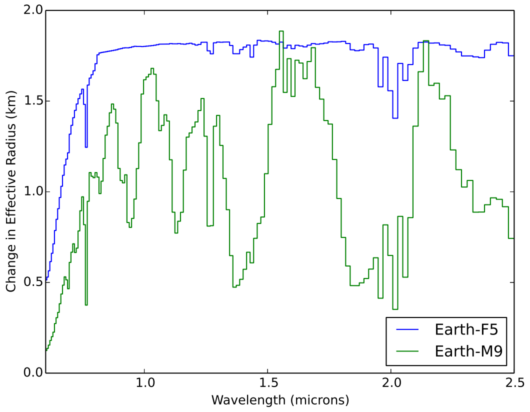

Figure 4.3: Wavelength-dependent changes in the out-of-transit light curve for a 2 $R_\oplus$ Super-Earth with an Earth-like atmosphere, represented as the change in effective radius (km). The spectra shown are the differences in the spectra between Stage 2 and Stage 1 of the transit (see Figure 4.1). This figure shows that the refracted light signal could be detected over a wide wavelength range, and that it should be possible to bin over multiple spectral resolution elements to reduce the integration time needed to detect refracted light.

need to quantify the refracted light, which would require more observing time. Overall, a detection of refracted light is indicative of a non-hazy atmosphere and, for some regions of parameter space, quantifying the refracted light flux could aid in uniquely discriminating between cloudy, hazy, and clear sky atmospheres.

The refracted light brightness is strongest for planets with $T_{eq} < 400$ K for planets orbiting M dwarfs and < 600 K for planets orbiting F, G and K stars. We find that refracted light is undetectable for very high temperature planets. For hot, close-in planets, the planet-star distance (*d*) is small, such that the characteristic deflection angle R_*/d is large, and that large refraction angles are required to produce a strong refracted light signal. For $T_{eq} >800$ K, angles this large would require probing pressures greater than 1 bar, where most atmospheres should be opaque, meaning that atmospheric opacity results in low refracted light signals. For the coldest ($T_{eq} <150$ K) planets, *d* is large and the refraction angles for clear sky atmospheres are often much larger than R_*/d. This results in more refracted light being observed further away from ingress and egress, increasing the average flux in Stage 1 relative to Stage 2 and reducing the overall detectability (see Figure 4.1).

In the near future, E-ELT could be used to identify non-hazy potentially habitable planets, which have $180 < T_{eq} < 260$ K (Kopparapu *et al.* (2013), Ravi Kopparapu, private communication). As shown in Table 4.2 and Figure 4.2, refracted light could be detectable with one transit with E-ELT, or <5 hr of out-of-transit E-ELT time for potentially habitable N_2 dominated Super-Earths orbiting F, G, and K stars. For planets orbiting M dwarfs, the required number of transits is typically less than two, with a total integration time of <5 hr. Hedelt *et al.* (2013) estimate that it could take up to 10 transits to detect H_2O and CO_2 for Earth-like planets orbiting F, G, and K stars with E-ELT using filter photometry, and Rodler and López-Morales (2014) find that it would take >20 hr of E-ELT time to detect O_2 for Earth-like planets orbiting M dwarfs using high-resolution ($R > 10{,}000$) spectroscopy. These estimates are larger than the amount of out-of-transit E-ELT time necessary to detect refracted light for potentially habitable planets. Therefore, because refracted light could be more detectable than spectral absorption features, looking for refracted light to distinguish between hazy and non-hazy exoplanets could be a useful tool in selecting exoplanets for extended follow-up observations.

Table 4.2: E-ELT results were calculated assuming 50 spectral resolution elements could be binned over. Results shown here are for most favorable cases orbiting Sun-like stars. Full table can be found at: `http://iopscience.iop.org/2041-8205/795/1/L14/fulltext/apjl502896t2_mrt.txt`

Planet Type	T_{eq} (K)	T_* (K)	Atm. Type	Albedo	Flux (ppm)	Int. Time (h)	E-ELT Transits	Tot. Time (yr)	Int. Time (h)	JWST Transits	Tot. Time (yr)
Earth	400	5780	clear sky	0.15	0.13	4.77	1.0	0.3	999.00	781.2	231.9
Super-Earth	450	5780	clear sky	0.15	0.29	0.91	1.0	0.2	999.00	166.9	34.8
Mini-Neptune	250	5780	clear sky	0.15	1.98	0.02	1.0	1.2	27.65	2.0	2.4
H_2O Super-Earth	400	5780	clear sky	0.15	0.41	0.45	1.0	0.3	640.78	73.9	21.9
CO_2 Super-Earth	600	5780	clear sky	0.15	0.22	1.60	1.0	0.1	999.00	393.7	34.6
Neptune	250	5780	clear sky	0.15	3.79	0.01	1.0	1.2	7.58	1.0	1.2
Saturn	300	5780	clear sky	0.15	10.98	0.01	1.0	0.7	0.90	1.0	0.7
Jupiter	350	5780	clear sky	0.15	6.39	0.01	1.0	0.4	2.66	1.0	0.4

Chapter 5

THE EFFECTS OF MULTIPLE, DIRECTIONAL SCATTERING ON TRANSIT TRANSMISSION SPECTROSCOPY

In this chapter, I examine the effects of forward scattering on transit transmission spectra and transit light curves. Forward scattered light can increase the observed flux in the transmission spectrum, altering the scattering continuum. Light can also be scattered before ingress and after egress, and could be detectable in transit light curves. A detection of out-of-transit scattered light would suggest the presence of highly forward scattering aerosols in the planet's atmosphere, and could be a powerful diagnostic tool for characterizing exoplanet atmospheres. Portions of this chapter will be submitted to *The Astrophysical Journal* in collaboration with V. S. Meadows.

5.1 Introduction

Most transit transmission spectroscopy models include extinction from clouds and hazes (e.g., Fortney (2005); Howe and Burrows (2012); Vahidinia *et al*. (2014)), but to date, few have included the effects of multiple scattering. Typically, scattering is treated only as extinction; that is, when a photon is scattered it is assumed to be removed from the beam that would reach a distant observer. However, multiple scattering concentrated in the forward direction could be important, as photons that are forward scattered will not deviate significantly from the initial trajectory and could still reach a distant observer. de Kok and Stam (2012) look at multiple scattering in transit transmission, examining case studies of HD 189733b in transit transmission and Titan in occultation measurements. Here we build upon this previous work by exploring the general effects of scattering for exoplanets over a range of stellar types and planet-star distances.

We show that scattering increases the total flux observed from the planet (when compared to treating scattering as extinction), with greater increases in flux for planets orbiting near to their parent star. We also explore the effect of scattering on transit light curves. Scattering has been proposed as an explanation for the light curve of KIC 12557548b, in which there is an increase in flux prior to ingress (Rappaport *et al.*, 2012; Croll *et al.*, 2014). Although KIC 12557548b is thought to be a disintegrating planet because of its proximity to its host star, scattering could be detectable in the light curves of planets orbiting further from their host stars. As discussed in Chapter 4, refraction can also lead to increases in flux in out-of-transit light curves. We first present the effect of forward scattering on transit light curves. Then, at the end of this chapter, we compare the effects of scattering and refraction on transit light curves and show how to discriminate between the two.

5.2 Model Atmospheres

We simulated spectra with and without the effect of forward scattering for Wasp-12 b and Venus. We ignore refraction at first to isolate the effect of forward scattering, and then compare the relative effects of scattering and refraction at the end of this chapter. Wasp-12 b presents an ideal opportunity for making predictions for forward scattered light because it is very close to its host star (resulting in a large scale height and therefore large transmission signal) and there is evidence of possible aerosols in its atmosphere from its moderately high albedo (Cowan *et al.*, 2012), and spectral absorption features that are much weaker than what would be predicted for a cloud- and haze-free H_2 atmosphere (Stevenson *et al.*, 2014). For simplicity, we generated spectra for Wasp-12 b with only aerosol absorption from Al_2O_3 and Fe_2O_3, which are candidate condensates for high-temperature planets like Wasp-12 b (Sing *et al.*, 2013). The scattering properties were calculated using a Mie scattering code (Bohren and Huffman, 1983), with publicly available optical constants for Al_2O_3

(Koike *et al.*, 1995) and Fe_2O_3 [1] used in our spectral simulations.

Venus presents another good test case for forward scattering because it has 5 aerosol particle layers, many of which are highly forward scattering in the visible and near-infrared. For Venus, accurate atmospheric data are available so we generated a spectrum with gas absorption, Rayleigh scattering, and aerosol absorption. We used temperature and gas mixing ratio profiles from two sources, one for altitudes $<$95 km (Bezard *et al.*, 1990) and another for greater altitudes. Including high-altitude atmospheric information is necessary because previous studies have shown that the effective absorbing radius of Venus can be as great as $\sim$120 km in the 4.3 μm CO_2 band (García Muñoz *et al.*, 2012; Ehrenreich *et al.*, 2012), which is greater than the extent of the Bezard *et al.* (1990) atmospheric sounding data. Therefore, we included the temperature profile and CO_2 mixing ratio profile from Gronoff *et al.* (2008), which is applicable to the upper atmosphere. All other gas mixing ratios were assumed to be negligible above 95 km. The absorption features that require atmospheric information above 95 km are all due to CO_2, so this assumption should not greatly affect the spectrum. To model the aerosol opacity, single scattering albedo, and scattering phase function we adopted the cloud and haze parameterization from Crisp (1986), which is based on Pioneer Venus orbiter and entry probe data. The scattering phase functions were calculated using optical constants for H_2SO_4 from Palmer and Williams (1975) and a Mie scattering code (Bohren and Huffman, 1983).

We also modeled the effect of forward scattering on transmission spectra and transit light curves over a grid of planetary radii, planetary atmospheric scale heights, angular stellar sizes and asymmetry parameters. The angular radius of the star (as seen by the planet) determines the range of angles a photon can be scattered by and still reach a distant observer, to first order. The asymmetry parameter was used to calculate the Henyey-Greenstein phase function (Henyey and Greenstein, 1941). The Henyey-Greenstein phase

---

[1] http://www.astro.uni-jena.de/Laboratory/OCDB/oxsul.html

function is an analytic phase function that depends on the asymmetry parameter, g. While a useful approximation when simulating a wide range of cases as done here, we find that these phase functions underestimate the forward scattering peak of the phase function for particles whose size is greater than $\sim$3 times the wavelength of incident light. When constraints can be placed on the aerosol composition, as above for Wasp-12 b and Venus, Mie scattering would be a more accurate method for calculating scattering phase functions. The planet radius and scale height determine the average path lengths taken through the atmosphere, and thus the optical depth in each layer. Additionally, the scattered light signal is proportional to the atmospheric scale height.

The model results were used to estimate the detectability of scattered light for hypothetical planets at 10 pc. For a given planetary equilibrium temperature and stellar effective temperature we determined the atmospheric scale height given the planet's surface gravity and composition, which are specified for each test case (see Chapter 4 for details on test cases). The scale heights of the atmospheres were calculated assuming a fixed albedo of 0.3, which is appropriate for the Earth with clouds but would need to be adjusted depending on expected cloud or haze type.

The scale heights of the clouds and hazes in the isothermal atmospheres were fixed to the pressure scale height. The haze scale height is roughly equal to the pressure scale height for H_2SO_4 in the upper atmosphere of Venus (Crisp, 1986) and is slightly greater than the pressure scale height in Titan's atmosphere (Bellucci *et al.*, 2009). For clouds that condense out, the haze scale height is often between $\sim$0.2 and 0.6 times the pressure scale height, depending on the droplet sedimentation (Ackerman and Marley, 2001). Therefore, while we assume the aerosol scale height is equal to the pressure scale height here for simplicity, when applying the results shown below to observations of a specific exoplanet multiple scale heights would need to be considered.

5.3 Results

5.3.1 Forward scattered light in transit transmission

We calculated the amount of forward scattered light for planets with planetary radii from half an Earth radius to a Jupiter radius and for atmospheric scale heights from 1 km to 1000 km. This range of planetary radii and scale heights covers exoplanets from 2000 K Hot Jupiters to cold, Mars-sized objects. For each pair of planetary radii and scale height, we ran our model with Henyey-Greenstein phase functions with scattering asymmetry parameters from 0.1 to 0.95. We also ran models for stellar angular radii (as seen from the exoplanet) up to 20 degrees (or $\frac{a}{R_*} > 2.7$), which is the largest angular radius for any known exoplanet (Wright *et al.*, 2011).Additionally, the Roche limit is $2.44 \times R_*$ (assuming equal stellar and planetary densities) resulting in an angular radius of 22.3 degrees, which is likely the absolute upper limit for the angular radius of the star.

Figure 5.3.1 shows the results of our forward scattering calculations for two test cases: an Earth-radius planet with a scale height of 50 km and a Jupiter radius planet with a scale height of 400 km. These cases correspond to a 1000 K, H_2O-dominated atmosphere and a 1000 K, H_2-dominated atmosphere, assuming Earth-like surface gravity. We find that the most favorable cases for showing the effect of forward scattering are for planets that are very close to their host stars, which will tend to be hot planets. The results show that for highly forward scattering particles (larger g values), there can be a decrease in the effective absorbing radius of the planetary atmosphere of $\sim$1 scale height, compared to models that only include extinction from aerosols. While we show results only for two radius-scale height pairs, we find similar results for all of parameter space.

We examined the effect of forward scattering on the spectrum of the hot Jupiter Wasp-12 b. As previously noted, the lack of strong spectral absorption features and a high albedo suggest that Wasp-12 b may have an optically thick aerosol layer, as investigated previously

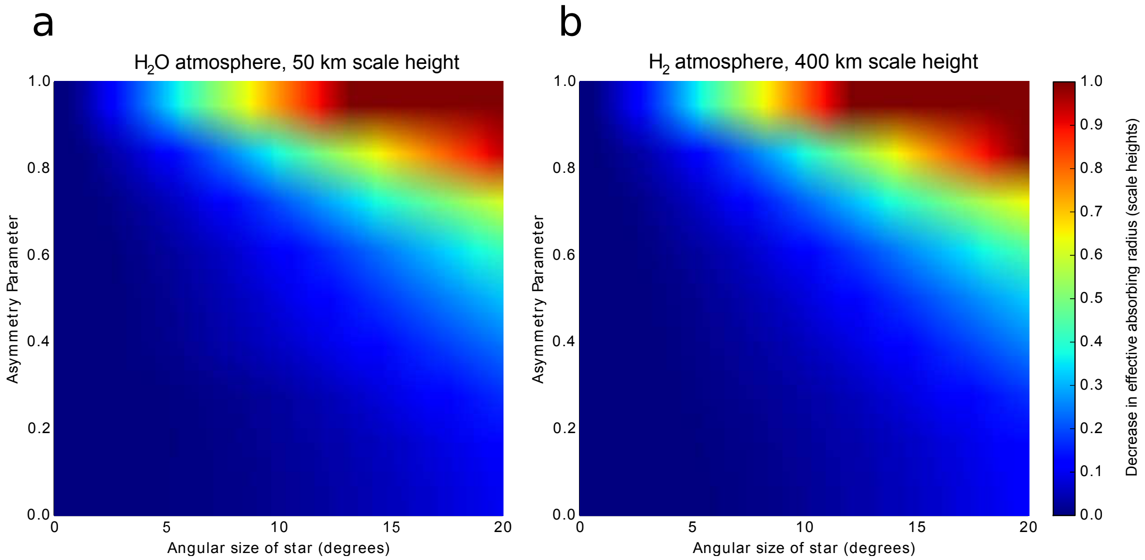

Figure 5.1: Decrease in effective absorbing radius (in terms of scale heights) when including forward scattering compared to treating scattering as extinction for **a)** a planet with the Earth's radius and a scale height of 50 km and **b)** a planet with Jupiter's radius and a scale height of 400 km. 50 and 400 km correspond to the atmospheric scale heights for a 1000 K H_2O-dominated atmosphere and a 1000 K H_2-dominated atmosphere, respectively, both with Earth-like surface gravities. For comparison, Wasp-12 b has a surface gravity within 10% of Earth's. These results were calculated assuming a single scattering albedo of 1. We find similar results for all planetary radii and scale heights tested.

by Sing *et al.* (2013). Furthermore, Wasp-12 b has the smallest $\frac{a}{R_*}$ of any Jupiter-sized planet, so forward scattering could have a larger effect on the spectrum for this world than for other hot Jupiters. Following the methodology of Sing *et al.* (2013), we generated spectra for atmospheres with Al_2O_3 and Fe_2O_3 aerosols, assuming spherical particles. We ran our models with log-normal particle size distributions with a range of mean particle sizes from 0.1 to 5.0 μm and variances from 0.01 to 0.3 μm^2. A subset of the resulting spectra are shown in Figure 5.2, along with the observed data. Small particle sizes ($<$0.2 μm) provide the best fits to the data, consistent with findings from Sing *et al.* (2013). The effect of forward scattering is large for particle sizes $>1\mu$m, for which the model fits tend to be poorer. The maximum difference between the spectra with and without the effect of forward scattering is $\sim$0.002 in terms of radius ratio, which corresponds to a flux difference of $\sim$50 ppm.

Forward scattering may have an effect on the transit transmission spectra of terrestrial planets orbiting brown dwarfs. Brown dwarfs have been considered as planet hosts and potential targets for transit transmission spectroscopy of exoplanets (Belu *et al.*, 2013). The habitable zone for brown dwarfs are expected to be very close-in, and even within the Roche limit for old, low-mass brown dwarfs (Andreeshchev and Scalo, 2004; Bolmont *et al.*, 2011). We chose to examine a Venus-analog because tidal Venuses are expected to be common around brown dwarfs (Barnes and Heller, 2013), and because Venus has forward-scattering haze layers in its upper atmosphere. Figure 5.3 shows spectra for Venus-analog planets for two test cases and a case which did not include the effect of forward scattering. The first was for a planet orbiting at 0.01 AU (near the inner edge of the habitable zone for a young, 40 M_{jup} brown dwarf, angular primary size of $\sim$2.5°). The second was for a planet at the most optimistic Roche limit, assuming the highest predicted terrestrial planet density of 7.5 $\frac{g}{cm^3}$ (Rogers, 2014; Weiss and Marcy, 2014) and a brown dwarf mass of 10 M_{jup}, which is the lowest mass brown dwarf considered by multiple previous authors

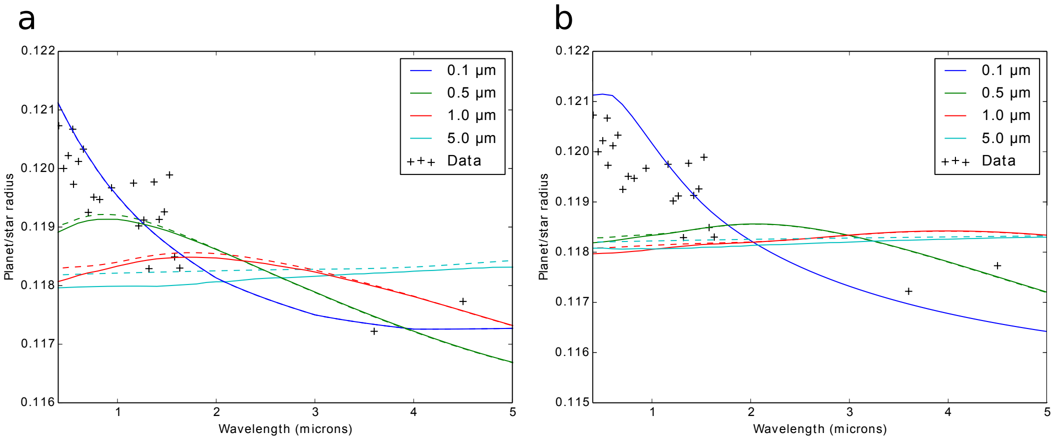

Figure 5.2: Spectra of Wasp-12 b with **a)** Al_2O_3 and **b)** Fe_2O_3 aerosols included with mean particle sizes ranging from 0.1 μm to 5.0 μm. The solid lines are for spectra with forward scattering included, and the dashed lines are for spectra with scattering treated as extinction, that is, without the effect of forward scattering. While the spectrum of Wasp-12 b is best fit by small (0.1 μm) particles for which the effect of forward scattering is negligible, forward scattering can lead to a decrease in the planet/star radius ratio by $\sim$0.002, which for Wasp-12 b corresponds to a flux difference of $\sim$50 ppm. Therefore, if large aerosol particles are present in hot Jupiter atmospheres, the effect of scattering may need to be considered to accurately fit the observed spectrum.

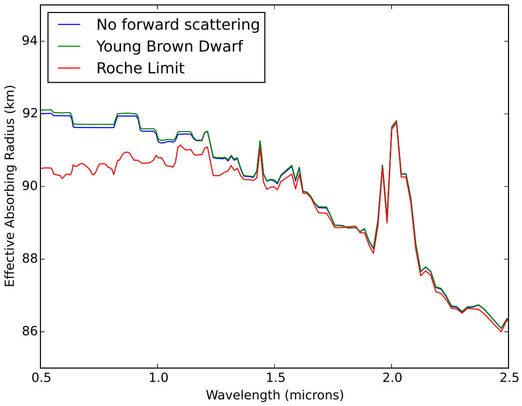

Figure 5.3: Forward scattering spectra of Venus around a young brown dwarf, a Venus analog at the Roche limit of a 10 M_{jup} brown dwarf, and a case without the effect of forward scattering. Forward scattering can have an effect up to 0.5 scale heights for Venus-analog orbiting near the Roche limit of a brown dwarf.

(Andreeshchev and Scalo, 2004; Bolmont *et al.*, 2011). The angular radius of the brown dwarf for the Roche limit case is ~20°. This corresponds to a distance from the brown dwarf of ~0.0013 AU. This would be interior to the habitable zone for a young (age <Gyr) brown dwarf but within the habitable zone of an older brown dwarf. Figure 5.3 shows the results for these cases. The Roche-limit Venus analog shows a decrease in effective absorbing radius of 2 km, or half a scale height, at wavelengths <0.9 μm, where the forward scattering is largest. Therefore, accurately modeling the continuum aerosol slope in the visible for a Venus-analog orbiting a brown dwarf could require including the effect of forward scattering in some cases.

5.3.2 Out-of-transit Scattered Light

Figure 5.4 shows the predicted out-of-transit flux signals (in terms of scale heights) for a 1000 K, Earth-radius planet with a pure H_2O atmosphere (scale height of 50 km) and a 1000

K, Jupiter-radius planet with a pure H_2 atmosphere (scale height of 400 km), the same two cases shown in Figure 5.3.1. The maximum out-of-transit flux signal is $\sim$0.4 scale heights. While results are only shown for two cases, we find similar results over a wide range of planetary radii and atmospheric scale heights.

We also quantified the detectability of out-of-transit scattered light for a given planetary equilibrium temperature, stellar effective temperature and planet type for an exoplanet at 10 pc. The scattering model can generate scattering light curves in terms of ppm flux differences, which, when combined with noise estimates from the JWST and E-ELT ETC's, allows us to estimate the required integration time to obtain a S/N$>$3. Figure 5.5 shows results for the detectability of scattered light for Jupiter-analog exoplanets with JWST and for H_2O-dominated Earth-radius exoplanets with E-ELT. Following the methodology presented in Chapter 4, we assumed that it was possible to bin over 50 spectral resolution elements for the Earth-radii cases, because for an Earth-like planet there are $\sim$50 spectral resolution elements between the Rayleigh scattering tail and strong H_2O features in which the atmosphere is relatively transparent, potentially allowing for wavelength-binning. We find that out-of-transit scattered light could be detectable in $<$10 hours for planets with equilibrium temperatures $>$700 K for planets orbiting M dwarfs and with temperatures $>$1500 K for planets orbiting Sun-like stars.

We also calculated the detectability of scattered light for Wasp-12 b assuming an aerosol scale height of 765 km for a range of asymmetry parameters. The greatest ppm flux difference for the out-of-transit flux are 25 ppm for g=0.8 and 46 ppm for g=0.9. While the detection of a signal of this magnitude is currently not possible, we find that a 25 ppm signal could be detectable with 30 hrs of JWST time. For this specific case, the data are consistent with small particles that are not highly forward scattering, but this technique could in principle be used to provide evidence for clouds and hazes for other exoplanet atmospheres. For example, Wasp-18 b and Wasp-33 b are two other promising targets for detecting out-

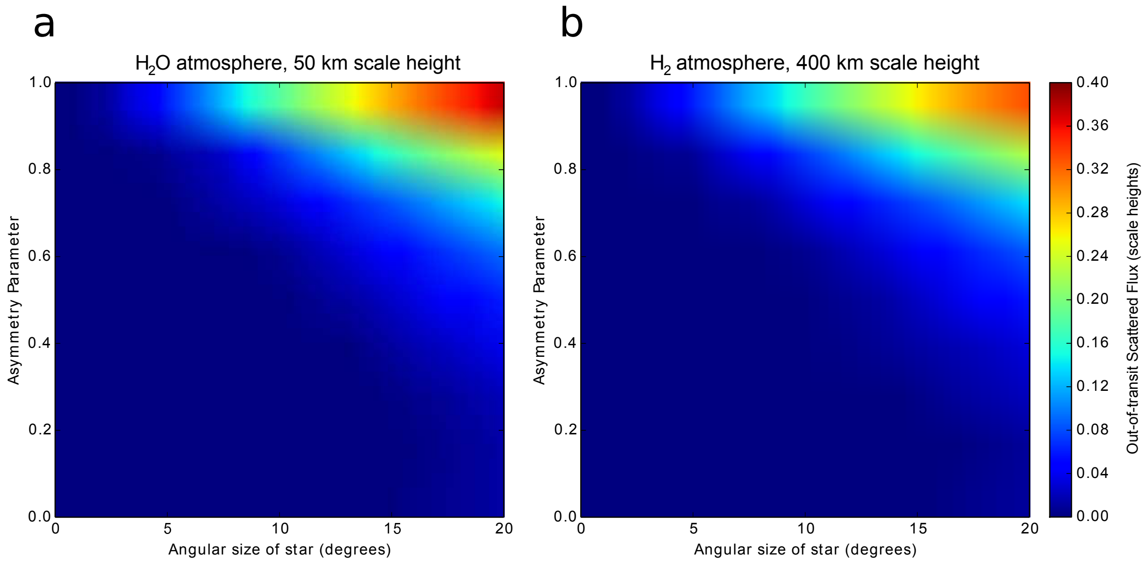

Figure 5.4: Out-of-transit scattered flux for a given asymmetry parameter and stellar angular radius from the planet's perspective. The results shown here are for **a)** an Earth-radius planet with a scale height of 50 km and **b)** a Jupiter-radius planet with a scale height of 400 km. For reference, 50 and 400 km are roughly the scale heights for a 1000 K planet with an H_2O-dominated atmosphere and a 1000 K planet with an H_2-dominated atmosphere, respectively, assuming Earth's surface gravity. The out-of-transit scattered light signal can be as great as $\sim$0.4 scale heights. We find similar results for other cases considered here.

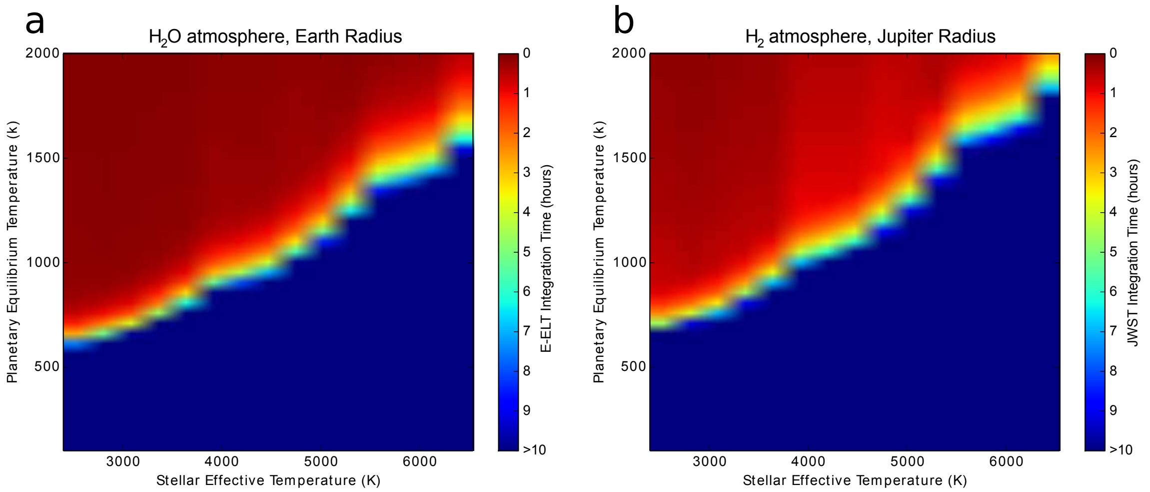

Figure 5.5: Integration time required to detect out-of-transit scattered light for **a)** an Earth-radius, H_2O-dominated planet with E-ELT and **b)** a Jupiter-radius, H_2-dominated planet with JWST at 10 pc, assuming a scattering asymmetry parameter of 0.8. For the E-ELT results, we've assumed that 50 spectral resolution elements can be binned, while the JWST results are for one spectral resolution element. We show results here for two cases, but we find similar results for all planet types considered here. Scattered light could be detected in $<$10 hrs for many planets with temperatures $>$700 K for planets orbiting M dwarfs and $>$1500 K for planets orbiting Sun-like stars. A detection of scattered light would strongly suggest the presence of forward scattering aerosols in the exoplanet atmosphere and could also be used to constrain aerosol particle sizes and composition.

of-transit scattered light. These two planets have $\frac{a}{R_*}$ values of 3.57 and 3.81, respectively, which corresponds to an angular radius of $\sim$15° for both cases. For this angular radius, the out-of-transit flux would be equivalent to the flux through 0.15 scale heights for g=0.8 and 0.25 for g=0.9. The scale height on the terminator is unknown for these two exoplanets, but assuming a scale height of 500 km, this corresponds to signals $\sim$15-18 ppm (g=0.8) and $\sim$25-30 ppm (g=0.9). For Wasp-33 b, the brighter of the two stars, this could be detected in $\sim$13 hrs (g=0.8) or $\sim$5 hrs (g=0.9) with JWST.

5.4 Discussion

5.4.1 Discriminating Between Refracted and Scattered Light

It should be possible to discriminate between the effects of refraction and forward scattering based on the stellar and planetary temperatures. In Chapter 3 we showed that the maximum tangent pressure set by refraction limits the detectability of spectral absorption features more for Earth-like planets orbiting Sun-like star than for Earth-like planets orbiting M dwarfs. In general, this effect is strongest for planets with maximum tangent pressures $<$1 bars because most atmospheres should be opaque at pressures $>$1 bar due to Rayleigh scattering, gas absorption or aerosol opacity. We find that maximum tangent pressures are $<$1 bar for $a/R_* > 11.5$ (or angular radius of the star $> 5°$ as seen by the exoplanet). For an Earth-like atmosphere, the maximum tangent pressure is at 1 bar for $a/R_* >50$, which corresponds to angular sizes of $\sim$1° and greater. In contrast, the increase in flux from scattered flux is greatest for $a/R_* < 6$, or angular stellar radii $>$10°. Therefore, the in-transit effects of refraction and scattering should be important only in their respective spheres of parameter space: refraction for cooler planets orbiting further away from their stars and scattering for hot, close-in planets.

A similar delineation between refraction and scattering is evident in the out-of-transit flux signals. In Chapter 4, we showed that refracted light could be detectable over a range of planet and star types, but only for relatively cool planets with equilibrium temperatures $<$400 K and $<$600 K for planets orbiting M dwarfs and Sun-like stars, respectively. Scattered light is most detectable for planets with temperatures $>$700 K for planets orbiting M dwarfs and temperatures $>$1000-1500 K for planets orbiting F, G, and K stars. This roughly corresponds to refracted light being detectable for angular stellar sizes $< 5^\circ$ and scattered light for angular sizes $> 10^\circ$. Therefore, for a given stellar type and the estimated planetary temperature, either refraction or scattering are expected to be important, but not both.

The reason for this delineation between refraction and scattering effects is because deflection angles due to refraction are dependent on the atmospheric densities probed, while deflection angles due to scattering are (to first order) independent of density and depend only on the scattering phase function. We find that the out-of-transit flux signals are greatest when the deflection angles (due either to refraction of scattering) are roughly equal to or less than the angular size of the star, as seen by the exoplanet. For a given atmospheric composition and atmospheric temperature profile, the refraction angles increase as greater pressures or densities are probed. As the apparent angular size of the star increases (as the planet is placed close to the star), greater refraction angles would be needed to have a large out-of-transit signal, and greater pressures would need to be probed. At high enough pressures, the atmosphere will be opaque and eventually the critical refraction angle will be reached. Therefore, there will be a cutoff in terms of a/R$_*$ for which smaller a/R$_*$ values (closer-in planets) will have greatly reduced refracted light signals. This is seen in Figure 4.2 from Chapter 4. For scattering, the deflection angles are determined by the scattering phase function, which is dependent only on the aerosol properties in a given layer. Therefore, the limit to the out-of-transit scattered light signal will be the angular size of the star as seen by the exoplanet. For large a/R$_*$ values (further out planets), there will be a narrow range of scattering angles for which a photon can be deflected to a distant observer, and the scattering signal should be small. For smaller a/R$_*$ values (closer-in planets), there will be a larger range of angles that will result in a photon being deflected to a distant observer, and the out-of-transit scattered light signal should be larger. Qualitatively, this matches the results from this chapter and from Chapter 4, in that scattered light is only detectable for hot, close-in planets, and refracted light is only detectable for cooler planets.

5.4.2 Implications for Detecting Out-of-transit Scattered Light

The detectability of out-of-transit scattered light is strongly dependent on the asymmetry parameter, which is a measure of how forward-scattering the scattering phase function is. For isotropic scatterers, scattered light should not be detectable for any combination stellar and planetary temperature examined here. This matches the results of Brown (2001), who examined the detectability of Rayleigh scattering pre-ingress and post-egress. Because scattering from isotropic scatterers is negligible, a detection of scattered light would imply some degree of forward scattering, which would likely be from some cloud or haze particles in the atmosphere. Therefore, a detection of scattered light would be indicative of clouds and hazes in the atmosphere.

The wavelength-dependence of out-of-transit scattered light could also aid in setting upper limits on the phase function asymmetry parameter at each wavelength. Since particles with sizes much greater than the incident wavelength of light tend to be more highly forward scattering (i.e., larger asymmetry parameter), scattered light could place upper limits on the particle sizes in an exoplanet atmosphere. Because gas absorption or extinction associated with scattering could reduce the scattered light signal, these measurements could only provide upper limits on the forward scattering peak of the scattering phase function. For the E-ELT results shown in Figure 5.5, a detection of scattered light would likely only be able to put a broad constraints on the degree of forward scattering (i.e., the asymmetry parameter) over the wavelength range because the signal has been binned over 50 spectral resolution elements. However, for the JWST results for Jovian planets, which are calculated at a single spectral resolution element at R=100, it may be possible to retrieve upper limits for the asymmetry parameter as a function of wavelength, which could be a powerful tool in characterizing the aerosol particle sizes and composition.

Chapter 6

BIOSIGNATURE AND HABITABILITY MARKERS IN TRANSIT TRANSMISSION SPECTROSCOPY: USING DIMERS TO MEASURE BIOSIGNATURES AND ATMOSPHERIC PRESSURE FOR TERRESTRIAL EXOPLANETS

In this chapter, I describe a method to estimate atmospheric pressure in an exoplanet atmosphere using absorption features from dimer molecules, focusing specifically on O_2 dimer molecules in Earth-like atmospheres. Atmospheric pressure is important for determining the phase state of surface water, and is therefore an essential parameter for determining habitability. Absorption features from dimer molecules are more strongly dependent on density (and therefore pressure) than absorption features from non-dimer molecules, and I show that it is possible to constrain atmospheric pressure if the absorption strengths of dimer and non-dimer absorption features can be quantified. Estimating pressure with dimer molecules should be possible for non-O_2 molecules, but O_2 dimer absorption features have the added benefit that they are biosignatures, and could potentially be the strongest biosignatures for an Earth-like planet in transit transmission. Portions of this chapter were originally published in collaboration with V. S. Meadows, M. Claire and D. Crisp in the February 2014 edition of *Astrobiology* (Misra et. al. 2014, *Astrobiology*, Vol. 14, pp. 67-86, ©2014 Mary Ann Liebert, Inc. Reprinted with permission from *Astrobiology*, 2014, published by Mary Ann Liebert, Inc., New Rochelle, NY.

6.1 Introduction

Atmospheric pressure is a fundamental parameter for characterizing the environment and habitability of an extrasolar planet. Water's stability on a planetary surface as a liquid depends on both the surface temperature and pressure. While the freezing point of water is not strongly dependent on pressure, pressure does affect water's boiling and sublimation points. Thus, a reliable estimate of the surface pressure is an important part of the measurement suite required to determine the habitability of an exoplanet.

Despite the importance of atmospheric pressure, current proposed methods for measuring pressure using remote-sensing techniques that could be applicable to exoplanet atmospheres are challenging. The existing techniques include the use of Rayleigh scattering (Kasting and Traub, 2010) or the widths of individual absorption lines (Kaplan *et al.*, 1964; Gray, 1966) or absorption bands (Ignatiev *et al.*, 2009; Chamberlain *et al.*, 2006; Spiga *et al.*, 2007; Chamberlain *et al.*, 2013). The presence and location of a blue Rayleigh scattering tail in a spectrum can provide information about the existence and pressure of an atmosphere. However, strong blue absorbers in the atmosphere (e.g. O_3, SO_2, NO_2 and many others) or surface features can mask this tail (Crow *et al.*, 2011). Furthermore, the Rayleigh scattering tail is most prominent shortward of 0.6 μm, below the short wavelength cutoff of the James Webb Space Telescope (JWST) (Gardner *et al.*, 2006). Lastly, planets around M dwarfs are likely to be the first to be characterized (Deming *et al.*, 2009), and M dwarfs have relatively less visible-flux to Rayleigh scatter than solar-type stars. The Rayleigh tail would be more difficult to detect and characterize for planets orbiting stars of this stellar class.

It is also possible to use the widths of absorption features to estimate pressure. Pressure increases the widths of vibration rotation lines of gases. This method has been successful for the Earth using high-resolution spectra of the O_2 A band (Barton and Scott, 1986; Mitchell and O'Brien, 1987; Crisp *et al.*, 2012), for Mars using CO_2 features near 2 μm

(Gray, 1966; Chamberlain *et al.*, 2006; Forget *et al.*, 2007; Spiga *et al.*, 2007) and the cloud tops of Venus using the 1.6 μm CO_2 band (Ignatiev *et al.*, 2009). This method provides unambiguous results when the spectral resolution is sufficiently high to resolve the profiles of individual spectral lines. It can also be used at lower spectral resolution, but requires prior knowledge of the mixing ratio of the absorbing gas.

Here we explore the feasibility of a new method to directly measure the pressure of an Earth-like atmosphere that combines the absorption features of dimers with those of monomer vibration-rotation bands to yield estimates of the atmospheric pressures even when the mixing ratio of the monomer is uncertain. Previous pressure estimates using dimer absorption have been made for the cloud tops of Earth, but these techniques have required prior knowledge of the gas mixing ratio profile (Acarreta *et al.*, 2004). Dimers are bound or quasi-bound states between two molecules driven together by molecular interactions. For example, the O_2-O_2 or O_4 dimer consists of two O_2 molecules temporarily bound to each other by Van der Waals forces. This dimer has its own rotational and vibrational modes, and produces spectral features distinct from its constituent O_2 monomers. Additionally, absorption from dimer molecules is more sensitive to pressure than that of monomers. The optical depth (how much absorption occurs) for dimers and monomers can be expressed by the following equations:

$$d\tau_{monomer} = \sigma\rho dl = \sigma P/T dl \tag{6.1}$$

$$d\tau_{dimer} = k\rho^2 dl = kP^2/T^2 dl \tag{6.2}$$

where $d\tau_{monomer}$ and $d\tau_{dimer}$ are the monomer and dimer differential optical depths, σ is the monomer cross section, ρ is the number density of the gas, k is the dimer cross section, P is the pressure, T is the temperature, and dl is the path length. While the monomer (e.g. O_2) optical depth is directly proportional to pressure, the optical depth of the dimer (e.g. O_2-O_2) is dependent on the square of the density (and hence square of the pressure). This difference in pressure dependence allows for estimating atmospheric pressure by comparing the dimer and monomer absorption features.

For an oxygen-rich, Earth-like atmosphere, the best combination of bands to use for pressure determination at near infrared wavelengths (>0.6 μm) would be the (O_2) A band at 0.76 μm, and the 1.06 μm O_4 dimer band. The 0.76 μm O_2 A band is the strongest O_2 feature in the visible-near-infrared spectral region, and is found in a relatively clean region of the spectrum between two water vapor bands. We have chosen the dimer feature at 1.06 μm as the likely best option for detectability, due to its combination of band strength and its location in a relatively uncluttered region of the planetary spectrum. Other O_4 features overlap with water features (dimer feature between 5.5 and 7 μm) or O_2 vibration-rotation bands (0.63 μm, 0.76 μm and 1.27 μm dimer features) or are weaker than the 1.06 μm dimer feature (0.477 μm and 0.57 μm dimer features). Nevertheless, some other features, in particular the strong 1.27 μm feature, could be used if the 1.06 μm dimer feature is not detectable.

In the proposed technique, the O_2 0.76 μm (monomer) band is used to provide an estimate of the atmospheric concentration of O_2, and combined with the O_4 1.06 μm (dimer) band to constrain the atmospheric pressure. This method can be used with either transmission spectroscopy, or directly-detected reflection or emission spectra, and serves as a complement to pressure determination techniques such as Rayleigh scattering, which only work in the visible. Although the proof of concept is shown here with oxygen, this technique is not limited to the oxygen dimer in an Earth-like atmosphere in the visible to near-infrared. The same technique is applicable to pairs of monomer and dimer absorption features across a wider range of planetary atmospheric composition and spectral wavelength range.

6.2 Methods

The transit transmission spectra were generated using the model described in Chapter 2. The effect of refraction was included for the spectra below, but the effect of forward scattering was not because the atmospheres used in this chapter do not include clouds or hazes. Additionally, as shown in Chapter 5, the effect of forward scattering is expected to be negligible for planets in the habitable zone of any main sequence star. Since this chapter deals specifically with Earth-like exoplanet near the inner edge of the habitable zone, forward scattering should not have a significant effect.

6.2.1 Model Inputs

6.2.1.1 Direct Imaging (Reflected) Spectroscopy Model

The reflected spectra were generated using the standard version of SMART, which can include multiple scattering from clouds and aerosols. However, to maintain consistency with the transmission spectrum model, clouds were not included in this study. The reflected spectra were generated assuming a surface with a constant albedo of 0.16, which is the average albedo of the cloud-free Earth (Pierrehumbert, 2010). We also assumed the surface is a Lambertian scatterer. Other surface types could have introduced an error into any quantitative estimates in this paper, unless explicitly included in a retrieval attempt. Figure 6.1 shows the wavelength-dependence of a variety of surface types from the ASTER (Advanced Spaceborne Thermal Emission and Reflection Radiometer) spectral library (Baldridge *et al.*, 2009) and the USGS (United States Geological Survey) digital spectral library (Clark *et al.*, 2007). Surface albedos are nearly constant in the bands considered here, though, for example, snow fluctuates by $\sim$20% within the 1.06 μm dimer band. We modeled a test case with SMART with the snow surface to determine the error different surfaces can introduce. We found a difference of 15% between the seawater and snow cases when measuring the equivalent width (defined in Section 6.2.2) of the 1.06 μm dimer band. This difference was significantly less than the difference in measured equivalent widths for the cases considered in this paper. Therefore, we have considered any discrepancies due to variations in surface albedo to be minimal for the present work.

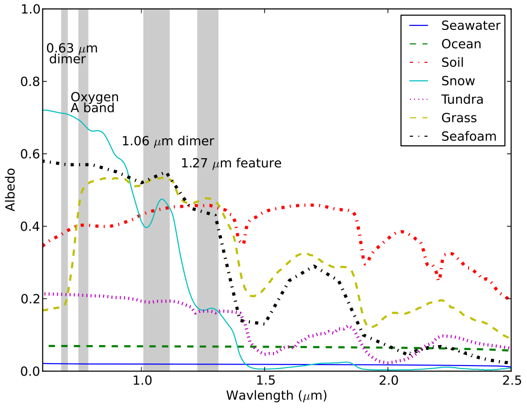

Figure 6.1: Wavelength-dependent albedos for a variety of common terrestrial surface types. The shaded regions correspond to O_2 monomer and dimer bands. For any absorption band, as long as the albedo does not vary widely within the band's wavelength range, it should be possible to measure an accurate equivalent width for each feature. The maximum surface albedo variation within each band is no more than ∼20%. Therefore we do not consider surface albedo variations important for this work.

6.2.1.2 Model Atmospheres

The cloud-free model atmospheres were generated by a one-dimensional (altitude) photochemical code with an extensive history in early Earth (Zerkle *et al.*, 2012), modern Earth (Catling *et al.*, 2010) and exoplanet (Domagal-Goldman *et al.*, 2011) research. The planetary radius and surface gravity used were the radius of the Earth (6371 km) and surface gravity of the Earth (9.87 m/s^2). The vertical grid consists of 200 plane-parallel layers that are each 0.5 km thick in altitude, in which radiative transfer, atmospheric transport, and photochemical production and loss are solved simultaneously, subject to upper (stellar flux, atmospheric escape) and lower (volcanos and biology) boundary conditions. The model calculates the mixing ratios of each species in each layer by solving the coupled mass-continuity/flux equations with the reverse Euler method (appropriate for stiff systems) and a variable time-stepping algorithm. Dimer concentrations were computed using estimations from quantum mechanical calculations. First, we fit the temperature dependence of the equilibrium constant for O_2-dimer formation using the following equations:

$$Kp = (p(O_2)_2/(pO_2)^2)/atm^{-1} \tag{6.3}$$

$$Kp(T) = 2428 * T^{(-3.518)} \tag{6.4}$$

where $p(O_2)_2$ and pO_2 are the dimer and monomer partial pressures (in atm) and T is the temperature (Uhlk *et al.*, 1993). Note that Kp is in units of inverse pressure. The dimer mixing ratio was then computed as:

$$p(O_2)_2 = Kp(T) * (pO_2)^2 * P \tag{6.5}$$

where P is the pressure in atmospheres. The choice of quantum parameters in our fit of equation 6.4 ensures that our calculation is a lower limit to the dimer concentrations, an assumption which matches modern atmospheric data well (Slanina *et al.*, 1994).

The model atmospheres used in this study started with boundary conditions that reproduce Earth's modern atmospheric chemistry. We then replaced the solar spectrum with the M dwarf spectrum described in 6.2.1.3 and decreased the surface albedo to 0.16 to account for cloud-free conditions. This "modified Earth around an M dwarf" model was then perturbed to examine changes to both total pressure and oxygen concentrations. Total atmospheric pressures of 0.1, 0.5, 1.0, 3.0, 5.0 and 10.0 bar were examined. At each of these total pressures, lower boundary conditions on O_2 mixing ratios were set at 0.1, 0.5, 1.0 and 2.0 times Earths present level. This corresponds to oxygen mixing ratios from 2% to 42%, which is roughly the range of oxygen concentrations experienced throughout the past 2.5 Gyr of Earths history (Kump, 2008). Boundary conditions for all other species were held fixed at modern values. Figure 6.2 shows the pressure-temperature profile and volume mixing ratio profiles for the 1.0 times the present atmospheric level (PAL) O_2 cases for spectrally active gases in the wavelength region examined here. Stable steady-state solutions were analyzed in all but the three cases with the highest O_2 surface partial pressures.

For those three cases, we extrapolated from our converged results at lower O_2 mixing ratios by increasing O_2 concentrations, scaling the dimer concentrations with the square of the O_2 mixing ratio, and keeping all other gas mixing ratios constant.

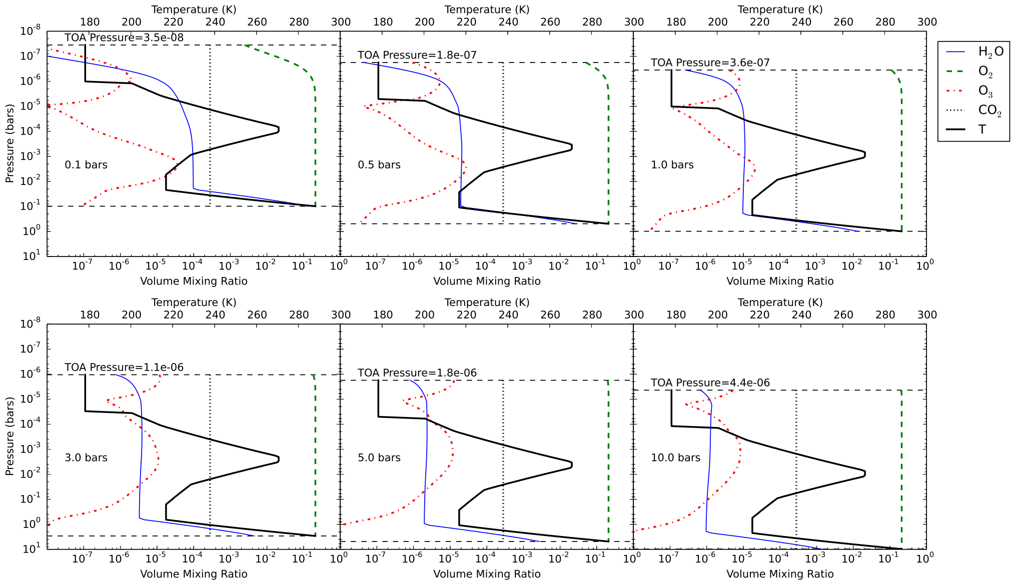

Figure 6.2: Pressure-temperature profiles and volume mixing ratio profiles for model atmospheres with total pressures varying from 0.1 to 10 bars at 1.0x PAL O_2. The black dashed lines represent the surface and top of atmosphere pressures. We use the modern Earth temperature-altitude profile in all cases and calculate the pressures assuming hydrostatic equilibrium. The remainder of the atmosphere is N_2 for all cases.

For all tests presented here, we assumed Earth-like temperature and water vapor profiles, precluding the need for costly climate simulations. More specifically, we took the modern Earth temperature profile as a function of altitude, and computed the corresponding pressure levels assuming hydrostatic equilibrium. This simplification provides a useful baseline, but limits the range of validity of these results somewhat because the gas absorption cross sections and number densities depend on these atmospheric properties. The impact of this assumption is assessed in Section 6.3.4. For pressure/temperature regions corresponding to Earth's mesosphere, we adopted a temperature of 180 K which likely overestimates the temperature in these regions. Dimer absorption preferentially occurs in higher pressure regions and so is insensitive to assumed conditions in the tenuous upper atmosphere. Our model grid was capped at 100 km altitude ensuring optically thin conditions for nearly all species, and made allowances for CO_2 and N_2 photolysis above the upper boundary. We used the modern measured eddy-diffusion profile to simulate convective motion for all atmospheres regardless of pressure. While this simplification would affect the prediction of trace gas concentrations, all species analyzed here are either well-mixed (CO_2, O_2, N_2) or short-lived (dimers) so are not sensitive to changes in turbulent mixing.

6.2.1.3 Stellar Properties

In this chapter we have assumed that the planet orbits an M5V star, or an M dwarf with stellar radius of 0.20 $R_\odot$ and a luminosity of 0.0022 $L_\odot$ (Reid and Hawley, 2005). The planet was placed at a distance of 0.047 AU, so that the total integrated incoming stellar flux was equal to the total flux the Earth receives from the Sun today. An M5 dwarf was chosen for these tests because there is a high probability that the terrestrial planets which will be the most easily characterized in the near future will be orbiting this class of star (Deming *et al.*, 2009). Additionally, transit transmission spectroscopy can probe pressures up to the $\sim$1 bar level in an atmosphere for an Earth analog around an M dwarf while for the Earth around the Sun, it can only probe pressures as great as $\sim$0.3 bars (see Chapter 3 for details). At these pressures and lower, the 1.06 μm dimer feature is very weak, even at 200% PAL O_2. Thus, using Earth-like atmospheres around an M dwarf instead of around the Sun provides a better demonstration of the pressure-dependence of dimer features.

To simulate the spectrum of the star, we used a Phoenix NextGen synthetic spectrum

(Hauschildt *et al.*, 1999) for all wavelengths greater than $\sim$300 nm. For the shorter wavelengths we used the UV spectrum of AD Leo (Segura *et al.*, 2005). The Phoenix spectrum was normalized so that the total integrated flux was equal to 1373 W/m^2, which is the integrated flux the Earth receives from the Sun. The AD Leo spectrum from Segura *et al.* (2005) was left unchanged, as it was already normalized to equal the amount of flux a planet near the inner edge of the habitable zone would receive.

6.2.1.4 Spectral Resolution

I have used a spectral resolving power of 100 to provide relevance to the James Webb Space Telescope (JWST), which will provide new opportunities for characterizing the atmospheres of transiting exoplanets (Lafreniere *et al.*, 2013). Once the JWST is launched, the Near-Infrared Spectrograph (NIRSPEC) will provide spectra with a spectral resolving power ($R=\frac{\lambda}{\Delta\lambda}$) of $\simeq$100 between 0.6 and 5.0 μm in single prism mode (Köhler *et al.*, 2005). We examine the effect of varying the spectral resolution in Sections 6.3.6 and 6.4.3.

6.2.2 Absorption Strength Measurements

To make a quantitative estimate of absorption strengths we measured equivalent widths for the reflected spectra and measured parts per million (ppm) differences in flux for the transmission spectra. The equivalent width is the width, in units of wavelength, of a rectangle measured from the continuum to the level of zero flux with the same total area as the spectral band. Equivalent widths were calculated using the following equation:

$$W = \int (1 - F_\lambda / F_0) d\lambda \tag{6.6}$$

where W is the equivalent width, F_λ is the flux at each wavelength λ, and F_0 is the continuum flux at each wavelength. To obtain the equivalent widths, we first measured the area of the spectral band below the continuum. For each absorption band, we define the continuum by hand. For the O_2 A band, the continuum was assumed to be linear with wavelength, and for the 1.06 μm feature the continuum was assumed to be constant with wavelength because in several of the cases the continuum at the longer wavelengths was difficult to define due to H_2O absorption.

6.2.3 Detectability Calculations

In addition to the detectability studies for the transit transmission spectra (described in detail in Chapter 2), we performed detectability studies for the direct imaging reflected spectra that could be relevant to proposed direct imaging planet detection and characterization missions. For these calculations, we did not use an instrument simulator because the exact specifications for these missions are not currently defined. For each absorption band, we calculated two S/Ns, one for detecting the spectral feature (S/N_D) and one for measuring the flux at the center of the band to a precision of 3σ (S/N_P). We calculated two S/Ns because obtaining information about pressure from a spectral feature requires more than detection; it also requires a quantitative estimate of the strength of that spectral feature. To calculate S/N_D, we divided the reflected flux by the stellar flux, defined a continuum and calculated the signal as the difference between the continuum and the normalized reflected flux. We assumed the noise is constant over the entire absorption band, and then calculated the noise level required to detect the spectral feature with a S/N_{band} of 3 in the absorption band. The final S/N_D is the mean of the continuum reflected flux level divided by the calculated noise. To calculate S/N_P, we selected the wavelength within the band with the lowest radiance. We set the value of a second noise level as the lowest radiance divided by 3. S/N_P is the continuum flux level divided by the noise required to obtain a S/N of 3 at the lowest radiance in the absorption band.

6.3 Results

6.3.1 Transit Transmission Spectra

I have generated transit transmission spectra and direct imaging spectra for atmospheres with O_2 concentrations of 10%, 50%, 100% and 200% of the PAL and pressures of 0.1, 0.5, 1, 3, 5 and 10 bars. Figure 6.3 shows the resulting transit transmission spectra for 100% PAL O_2. Transmission spectra of atmospheres with pressures $\geq$1 bar are nearly identical for a given O_2 concentration because refraction limits the depth of penetration to $<$1 bar. The dimer feature is weak for pressures of 0.1 and 0.5 bars.

Figures 6.4, 6.5, and 6.6 show the resulting transit transmission spectra for O_2 concentrations of 10%, 50% and 200% PAL. The 1.06 μm dimer feature is very weak at all pressures for O_2 concentrations at 10% PAL and weak for 50% PAL O_2, while it is very strong for pressures above 0.1 bars at 200% PAL O_2.

6.3.2 Reflected Spectra

Figure 6.7 shows the reflected spectra for modern O_2 mixing ratios in atmospheres with a range of total pressure from 0.1 to 10 bars. The 0.5 and 5.0 bar cases are omitted from the plots to increase clarity, but are still included in the equivalent width and S/N calculations. The 1.06 μm dimer feature is extremely weak for the present-day atmosphere, but in contrast to its behavior in the transmission spectra, it is a very prominent feature for the 3, 5 and 10 bar atmospheres.

Figures 6.8, 6.9 and 6.10 show the reflected spectra at pressures between 0.1 and 10 bars for 10%, 50%, and 200% PAL of O_2, respectively. In the 10% PAL case, the O_2 dimer feature at 1.06 μm is very weak because the total amount of O_2 is very low, even for a 10 bar atmosphere. The 1.06 μm dimer feature is stronger in the 3, 5 and 10 bar cases for atmospheres with 50% PAL O_2. Finally for the 200% O_2 atmospheres, the 1.06 μm dimer feature is one of the strongest spectral features, even in the 1 bar atmosphere.

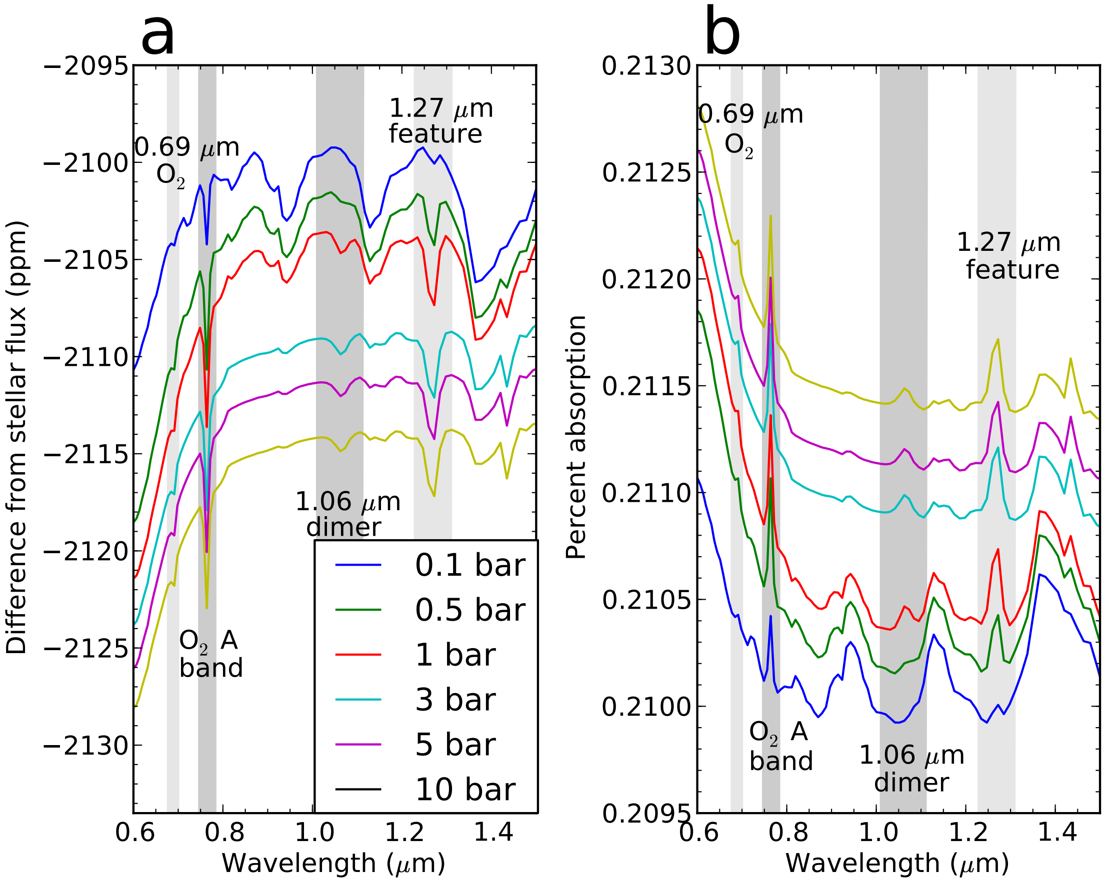

Figure 6.3: Transmission spectra of an Earth-like atmosphere with different total atmospheric pressures. **(a)** Difference in flux from the stellar flux. **(b)** Percent of stellar flux absorbed by the atmosphere. The 1.06 μm dimer feature is strong only in the spectra corresponding to atmospheres with surface pressures greater than ∼0.5 bar. The spectra for atmospheres with pressure ≥1 bar are nearly identical except for an offset because there is a fundamental limit on which heights in an atmosphere can be probed using transmission spectroscopy. For an Earth-like atmosphere around the M5V star used here, only the top 0.9 bars can be probed for all atmospheres at all wavelengths. For the temperature profiles assumed here, this pressure corresponds to an altitude of ∼1 km above the surface for a 1 bar atmosphere, and 19 km above the surface for a 10 bar atmosphere

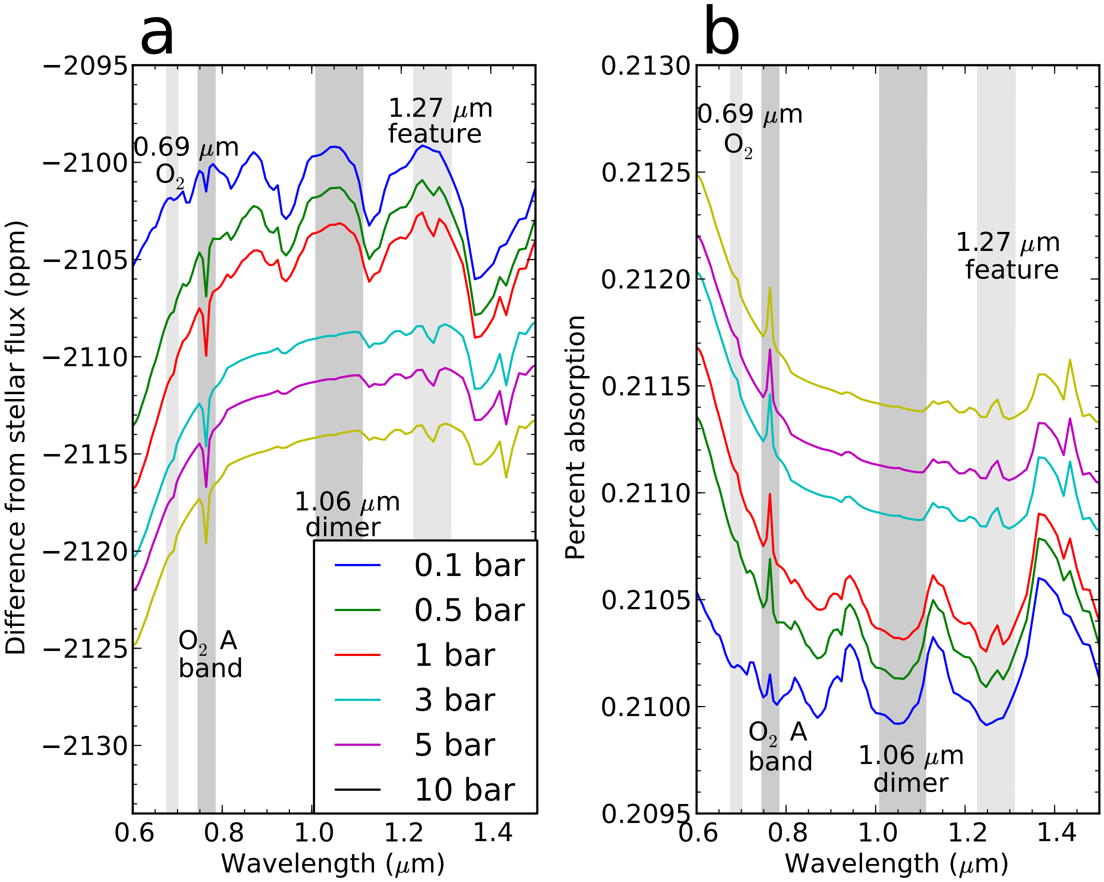

Figure 6.4: Same as Figure 6.3 but for 10% of the present day level of O_2. The dimer features do not appear at all because the O_2 concentration is too low.

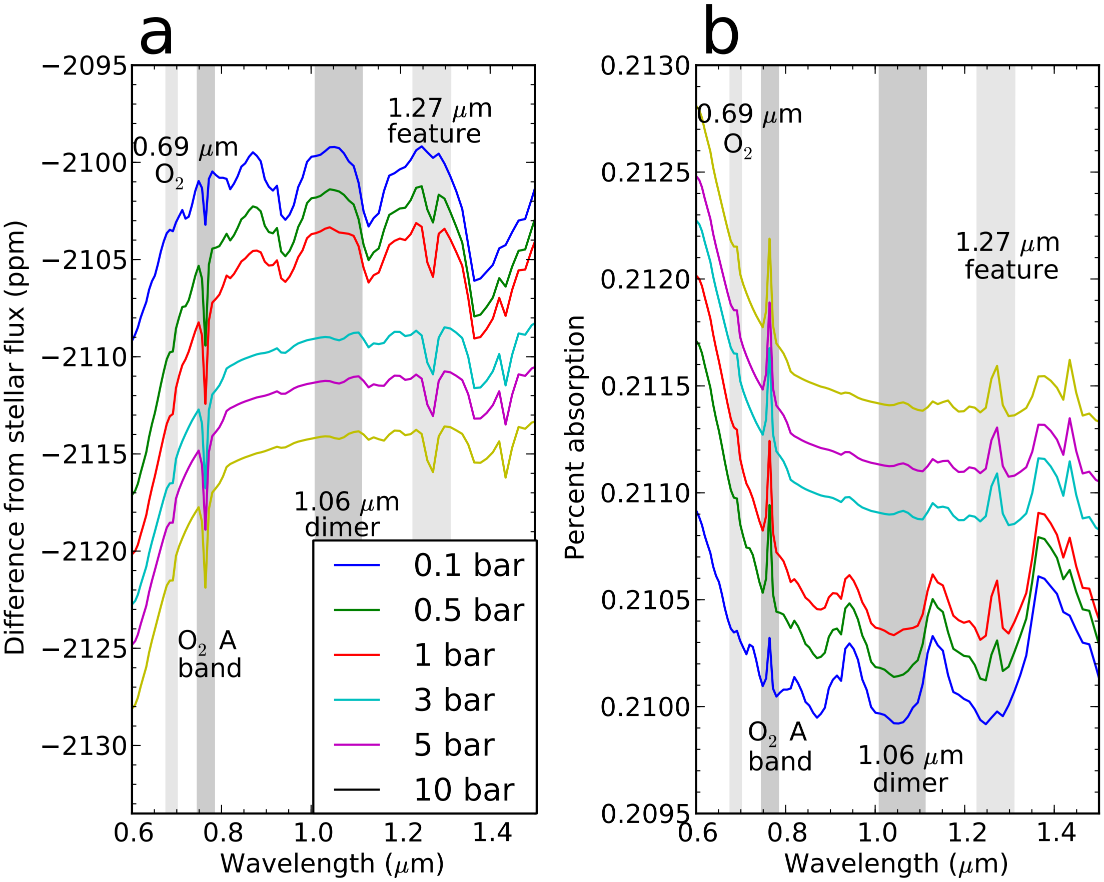

Figure 6.5: Same as Figure 6.3 but for 50% of the present day level of O_2. The 1.06 μm dimer feature is very weak, and is still weak for the highest surface pressure atmospheres.

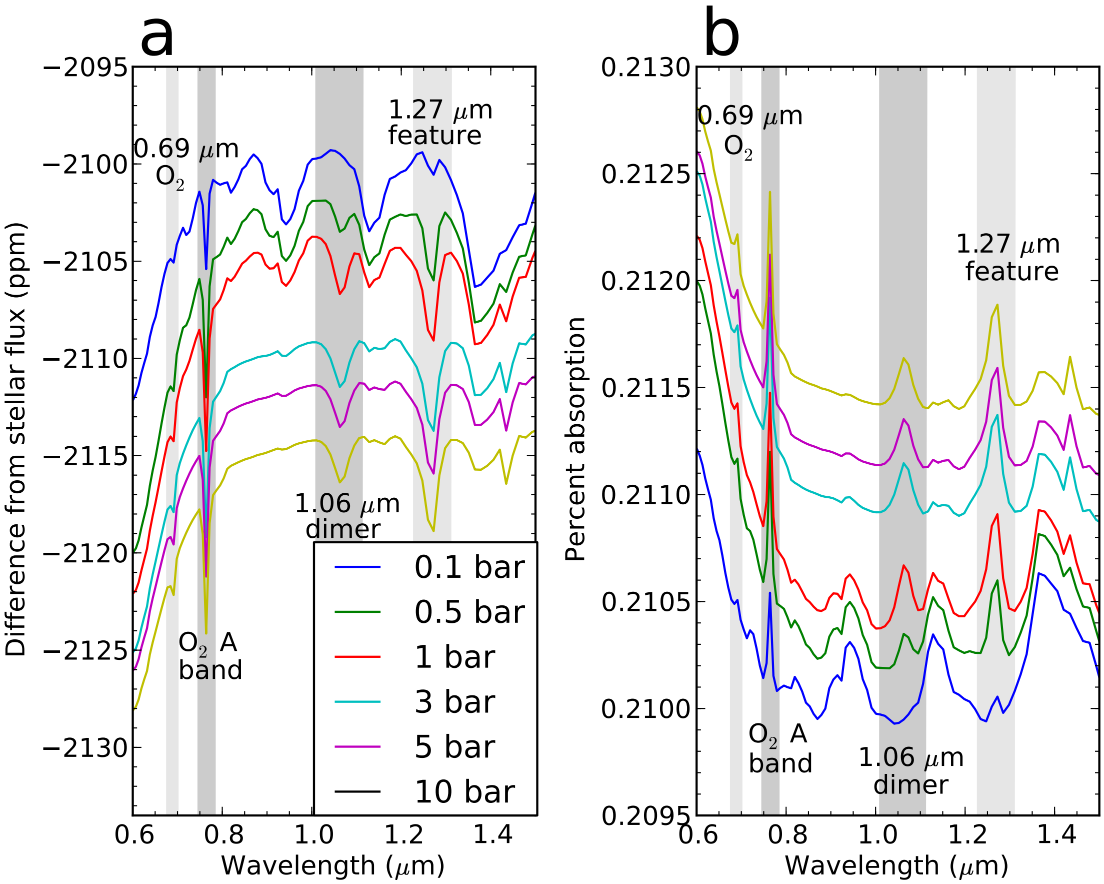

Figure 6.6: Same as Figure 6.3 but for 200% of the present day level of O_2. The 1.06 μm dimer feature is very strong in every case except for the 0.1 bar atmosphere.

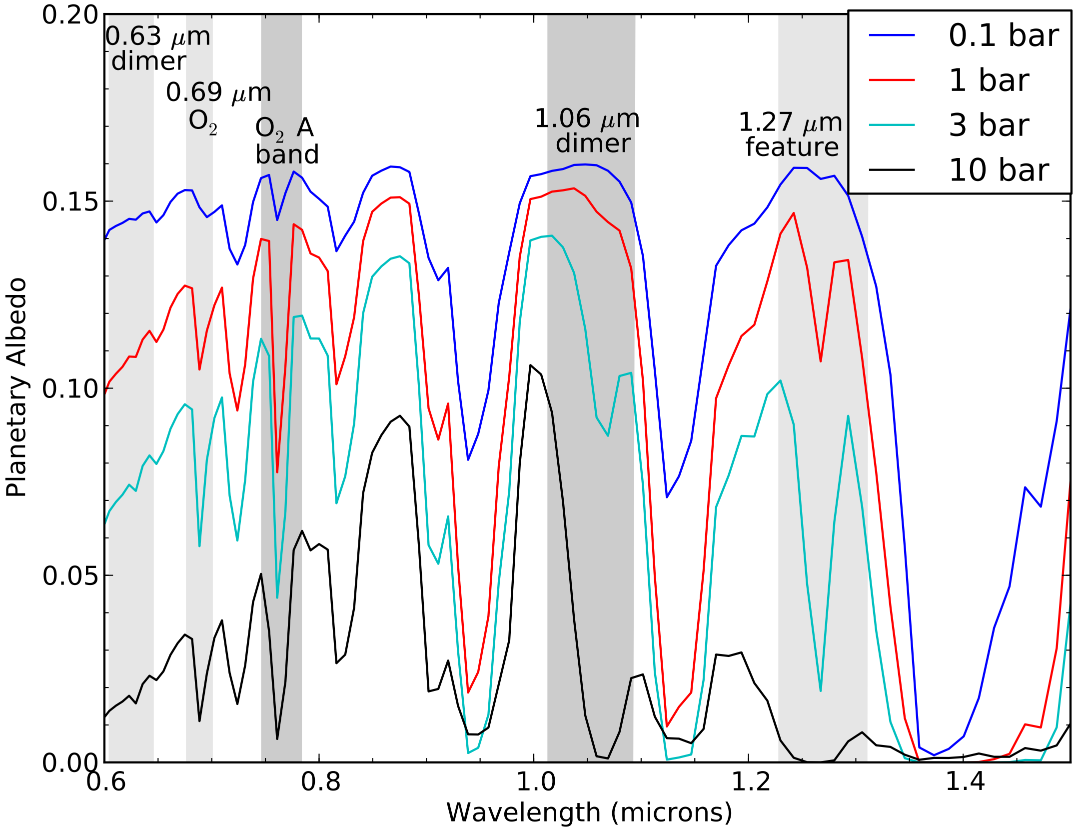

Figure 6.7: Reflected spectra for Earth-like atmospheres with 100% PAL O_2 but with different total atmospheric pressures. In the reflected spectrum there is no fundamental limit to which pressures can be probed in an atmosphere. Assuming a cloud-free case, it is possible to probe the surface layers of the atmosphere. The 1.06 μm dimer feature is fairly weak in the present day Earth's atmosphere, but it is a very strong feature in atmospheres with greater pressures. The 1.27 μm feature is very strong in most of the spectra.

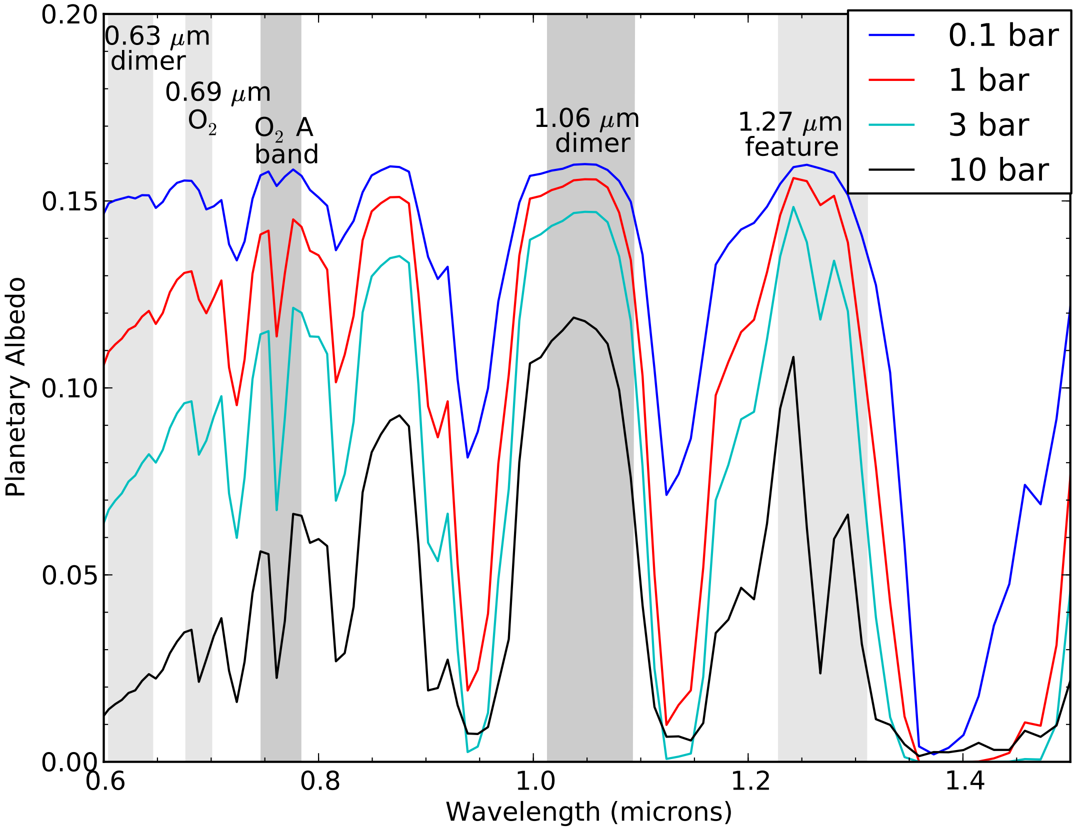

Figure 6.8: Same as Figure 6.7 but for an O_2 concentration of 10% PAL. For this amount of O_2, the 1.06 μm dimer feature is very weak. However, the 1.27 μm feature is still quite strong.

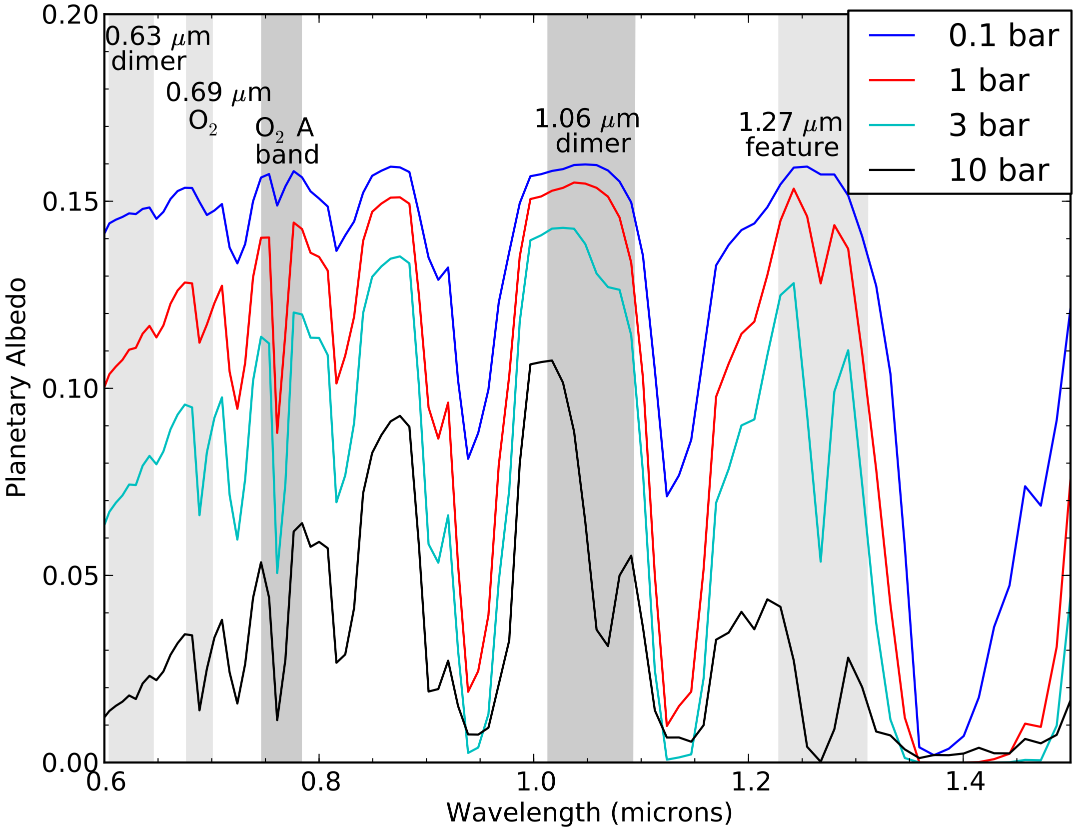

Figure 6.9: Same as Figure 6.7 but for an O_2 concentration of 50% PAL. The 1.06 μm dimer feature is strong at pressures $\geq$3 bars.

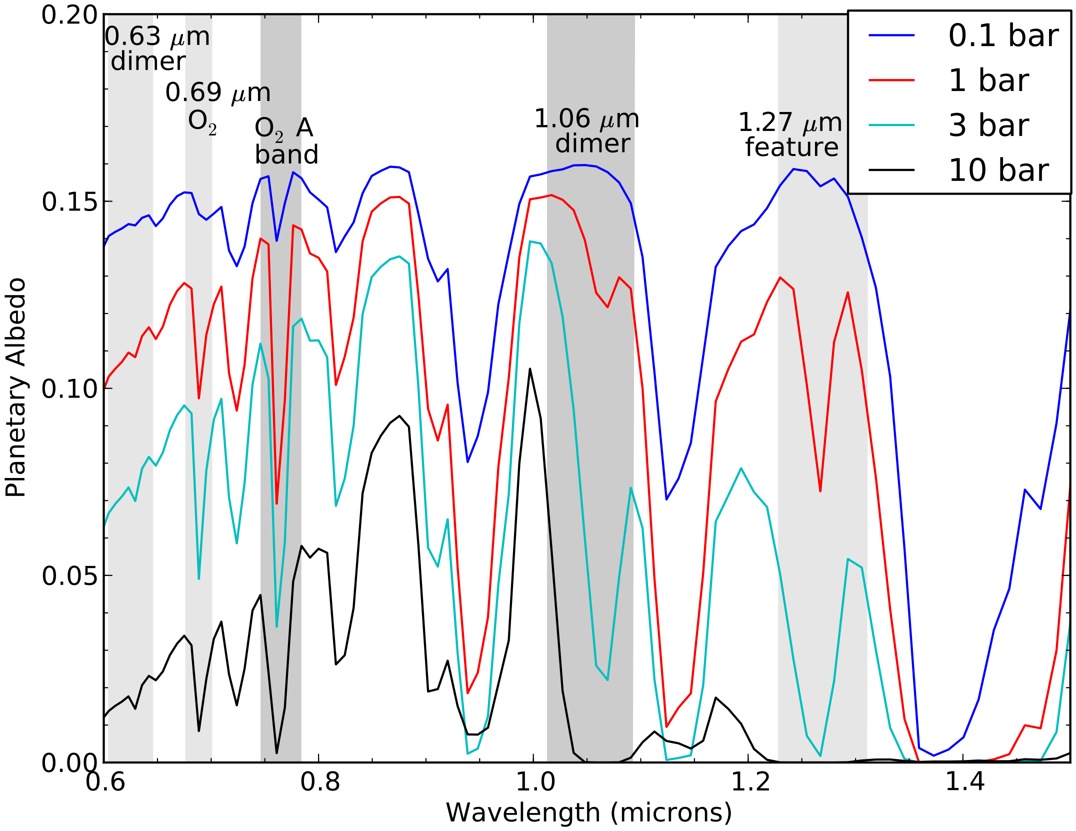

Figure 6.10: Same as Figure 6.7 but for an O_2 concentration of 200% PAL. The dimer features are much stronger with more O_2 in the atmosphere, as expected.

6.3.3 Quantitative Absorption Measurements

Figure 6.11 shows the flux change for the transmission spectra and equivalent widths for reflected spectra at different pressures and O_2 concentrations for the O_2 A band and the 1.06 μm dimer feature. For a given O_2 concentration the transit transmission flux differences for the O_2 A band are roughly constant for pressures $\geq$1 bar due to refraction. The 1.06 μm dimer feature flux differences increase slightly with pressure but are also constant for pressures $\geq$1 bar for a given O_2 concentration. The dimer feature does not appear in transmission for cases with 10% PAL O_2.

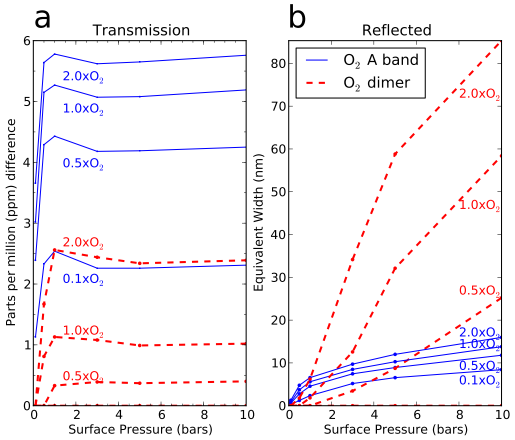

Figure 6.11: **(a)** Flux differences (in ppm) for transit transmission spectra and **(b)** equivalent widths (in nm) for reflected spectra for the O_2 A band and the 1.06 μm dimer feature at various pressures and O_2 concentrations. In transmission, for the Earth-like planet orbiting an M5V star considered here, only the top 0.9 bars can be probed, so that the dimer and A band equivalent widths are roughly constant with pressure above 1.0 bars for a given O_2 concentration. In the reflected spectra, the dimer equivalent widths are extremely sensitive to pressure.

For the direct imaging (reflected) spectra, both the O_2 A band and 1.06 μm dimer feature equivalent widths increase with pressure and increased O_2 concentrations. However, the dimer feature equivalent widths are much more sensitive to pressure. At higher pressures the dimer feature is strong except for cases with 10% PAL O_2, in which the 1.06 μm dimer feature is too weak to quantify.

Figures 6.12-6.14 show the relationships between the quantitative absorption measurements described above and atmospheric quantities including the O_2 mixing ratio and the O_2 partial pressure at the surface. The ppm flux difference measured in transit transmission for the O_2 A band could be used to constrain the O_2 mixing ratio, as shown in Figure 6.12b. The O_2 partial pressure at the surface can be estimated using the ratio between the 1.06 μm dimer and O_2 A band absorption measurements. These ratios are shown in Figure 6.12a using ppm flux differences, and in Figure 6.13 using equivalent widths. The O_2 mixing ratio and O_2 partial pressure at the surface can be combined to provide a unique estimate of the surface pressure of the planet. A more detailed description of the pressure measurement technique is given in Section 6.4.1.

6.3.4 Sensitivity Tests

To quantify the errors introduced by assuming the modern day temperature profile, we generated spectra to test the sensitivity of our models to changes in the temperature profile and in changes to the water vapor profiles. We compared our 1.0 bar, 1.0x PAL O_2 spectra to a spectrum generated using the same volume mixing ratio profiles but with an isothermal atmosphere at 250 K. We also compared our 1.0 bar, 1.0x PAL O_2 transit transmission spectrum to spectra generated with atmospheres with 0.1 and 10.0 times the H_2O levels. We perform a similar comparison for the 1.0 bar, 2.0x PAL O_2 reflected spectrum.

Figure 6.15 shows the sensitivity of the spectra to the temperature profile, with our Earth-like profile and an isothermal approximation profile compared. Both the transit transmission and reflected spectra show little sensitivity to the temperature profile. The 1.06 μm dimer band also shows little sensitivity to the temperature profile, despite the dependence of the dimer optical depth on the square of the temperature because the isothermal temperature profile approximates the average temperature of the troposphere, where the majority of dimer absorption occurs.

Figures 6.16, 6.17 and 6.18 show the results for the H_2O sensitivity tests. The O_2 A band equivalent widths and ppm flux differences are not strongly affected by changes in the H_2O profiles. However, changes in the H_2O mixing ratios affect the continuum flux in the wings of the 1.06 micron dimer feature, complicating measurements of the equivalent width of this feature. For the transit transmission spectra, the change in the total ppm flux difference (across the entire band) is less than 20% between the 0.1 and 10.0x H_2O cases. For the reflected spectra, the change in the equivalent width of the 1.06 μm dimer feature is less than 20%. For the reflected spectra, the equivalent widths can be much greater than that for the 1.0 bar, 2.0x O_2 case. For these greater equivalent widths, the effect of increasing or decreasing H_2O levels will diminish as the difference from the continuum flux (affected by H_2O) and the flux within the absorption band will increase.

6.3.5 Detectability of Spectral Features

Table 6.1 shows the S/Ns for observations by JWST for the O_2 A band, 1.06 μm feature and the 1.27 μm feature for the range of pressures and O_2 concentrations considered here for an Earth analog at a distance of 5 pc. The S/N are calculated assuming that every transit of an Earth analog orbiting an M5V star is observed over JWST's 5 year mission lifetime. In transit transmission, the O_2 A band S/Ns are no greater than 1.1. The 1.06μm dimer feature is detectable at a S/N of >3 for many of the 2.0x PAL O_2 cases. The 1.27 μm feature is the most detectable O_2 feature in this wavelength range, with S/Ns greater than 5 for many of the 1.0x PAL O_2 cases and greater than 7 for many of the 2.0x PAL O_2 cases. JWST will not be able to detect O_2 species for Earth-like exoplanets in secondary eclipse in the visible and near-infrared, as shown by the secondary eclipse S/N levels. Even for the highest pressure cases, the S/Ns are no greater than $\sim$0.2.

Table 6.2 shows the S/Ns necessary to detect and characterize the O_2 A band, 1.06 μm band and the 1.27 μm feature for the range of pressures and O_2 concentrations considered here for the direct imaging reflected spectra at R=100. The S/Ns in Table 6.2 would be relevant to a direct imaging characterization mission. While these S/Ns were calculated for an Earth analog orbiting an M5V star, the results should be independent of stellar spectral type because we divided out the stellar flux in our calculations. The O_2 A band, 1.06 μm dimer feature and 1.27 μm feature are detectable at an average S/N_D of 14, 9 and 14, respectively, for the cases when the features are strong enough to identify in the model spectra. The average required S/N_P to use the features for pressure estimation are 11, 31 and 34.

6.3.6 Effect of Spectral Resolving Power

I examined the effect of spectral resolving power on the detectability of spectral features by generating transit transmission spectra for the 1.0 bar, 1.0x PAL O_2 case with spectral resolving powers of 500, 200, 100, 80, 60, 40, 30 and 20. Figure 6.19 shows the spectra for each of these cases. We also measured the S/N of each feature at each resolving power. The S/Ns were calculated assuming a noise profile equivalent to the JWST NIRSPEC noise profile, but with the noise level at each wavelength divided by $(100/R)^2$, so that the noise at each wavelength decreased as the resolving power decreased. Figure 6.20 shows how the total S/N in each absorption band changes with resolving power. In general, the S/Ns drop off rapidly as resolving power decreases for $R<60$.

I also generated direct imaging reflected spectra for the 1.0 bar, 2.0x PAL O_2 case at resolving powers of 500, 200, 100, 80, 60, 40, 30 and 20, as shown in Figure 6.21. Figures 6.22 and 6.23 show how the S/N for detection and precision vary with resolving power for the O_2 A band, 1.06 μm dimer feature and the 1.27 μm feature. The S/N required to detect each feature increases as resolving power decreases. At R=20, the S/Ns are not shown because no spectral features could be identified, and at R=30 only the O_2 A band was identified. The S/N required to quantify the flux at the center of each spectral feature decreases as resolving power decreases, because the lowest radiance level increases as the spectral resolving power decreases.

6.4 Discussion

The 1.06 μm dimer feature is prominent in transit transmission for atmospheres with $\geq$50% PAL O_2 and surface pressures $\geq$0.5 bars. It is a prominent feature in the reflected spectra for atmospheres with $\geq$50% PAL O_2 and surface pressure $\geq$3 bars. For the reflected spectra, the dimer feature equivalent width is highly dependent on surface pressure when compared to the O_2 A band and therefore the dimer feature can be used to constrain pressure. Here we discuss how to do this for the cases investigated here.

6.4.1 Pressure Measurement Technique

Figure 6.11 confirms that dimer absorption features are more strongly dependent on pressure than monomer features. Therefore dimer features can be combined with monomer features to determine pressure, even if the mixing ratio of the absorbing gas is not known. With only transit transmission spectroscopy, it is impossible to probe pressures over $\sim$1 bar for the cases examined here, but it may be possible to constrain the O_2 mixing ratio and set a lower bound for pressure. In reflected spectra, it is possible to determine the surface partial pressure of O_2 and set a lower bound for pressure using the 1.06 μm dimer feature as an on/off pressure gauge. With both a transit transmission spectrum and a reflected spectrum, it should be possible to determine total atmospheric surface pressure for an Earth-like exoplanet.

6.4.1.1 *Transmission Spectra Pressure Measurement*

Transmission spectroscopy provides only a lower bound on the atmospheric pressure because refraction provides a fundamental limit to which pressures can be probed using this technique. For the spectra presented here, a lower limit of $\sim$1 bar can be set for the high pressure atmospheres. For a given O_2 concentration a unique estimate of the pressure can be retrieved from the ratio between the ppm flux differences of the 1.06 μm dimer feature and the O_2 A band. Figure 6.12a shows the relationship between this ratio and the total amount of O_2 above 0.9 bars, which is the highest pressure that can be probed in this particular case. There is a clear trend between this ratio and the amount of O_2 in the atmosphere. When combined with an O_2 mixing ratio this relationship can provide a quantitative estimate of a lower level of the surface or cloud-top pressure.

The O_2 mixing ratio can be estimated from the flux difference of the O_2 A band in transmission. Figure 6.12b shows the relationship between the O_2 mixing ratio (which is constant throughout the atmosphere) and the O_2 A band flux difference. For pressure $\geq$0.1 bars the O_2 flux difference is roughly constant for a given O_2 concentration, meaning that a measurement of the O_2 A band flux difference should correlate with the O_2 mixing ratio.

6.4.1.2 *Reflected Spectra Pressure Measurement*

Reflected spectra alone can provide an estimate of the surface partial pressure of O_2 by examination of the ratio of the 1.06 μm dimer equivalent width and the O_2 A band equivalent width. Figure 6.13 shows the relationship between this ratio and the surface partial pressure of O_2. The strength of the 1.06 μm dimer feature could also be used as an on/off gauge to set a lower bound for pressure. Determining total atmospheric pressure with only a reflected spectrum is difficult due to degeneracies between the O_2 concentration and total atmospheric pressure, as shown in Figure 6.14. For large equivalent widths of the dimer feature, the pressure will certainly be above 1 bar. However, it is difficult to differentiate between atmospheres with the same O_2 surface partial pressure. Nevertheless, it appears that it is possible to set a lower limit on pressure by measuring the 1.06 μm dimer feature equivalent width. For example, a 1.06 μm dimer feature equivalent width greater than $\sim$10 nm would imply a surface pressure $>$1 bar.

6.4.1.3 Pressure Measurement with both transit transmission and reflected spectra

If both a transit transmission spectrum and a reflected spectrum are available, it should be possible to directly measure the total atmospheric surface pressure in the absence of clouds. Transit transmission spectroscopy can provide an estimate of the O_2 mixing ratio as described previously. A reflected spectrum can theoretically probe to the reflecting surface and therefore can be used to constrain the O_2 partial pressure at the surface. By combining the O_2 mixing ratio and O_2 partial pressure we can determine the total pressure at the reflecting surface, which could either be a reflective cloud layer or the physical surface of the planet.

6.4.2 Relevance to Planet Characterization

The methods described here could be used in the near future by the JWST NIRSPEC instrument, which will potentially be able to characterize transiting planets between 0.6 and 5.0 μm. The O_2 A band will likely not be detectable for a nearby Earth-analog with JWST. Although this feature is strong in the spectrum, the sensitivity of NIRSPEC is poor at shorter wavelengths. The 1.06 μm dimer feature is detectable at the 3σ level in transit transmission for cases with 2.0x PAL O_2 and high surface pressures. Thus, the detection of the 1.06 μm dimer feature would imply a surface or cloud-top pressure greater than or equal to 1.0 bars. For cases in which the 1.06 μm dimer feature is not detectable, the 1.27 μm feature could be used to constrain the pressure. This feature is not as strongly dependent on pressure as the 1.06 μm dimer feature, but it is more detectable in all cases explored here.

TPF or a similar direct imaging mission will be required to characterize the reflected spectra of nearby Earth analogs in the visible and near-infrared. The S/N values for secondary eclipse using JWST are all less than 1, so JWST will not be able to characterize the reflected spectra of Earth-analogs in secondary eclipse. Table 6.2 shows the necessary S/Ns to detect and characterize spectral features for a direct imaging planet characterization mission. While the S/Ns were calculated for an Earth analog orbiting an M5V star, the results should be largely independent of spectral type because we have divided the reflected flux by the stellar flux in our calculations. The required S/N values suggest that a S/N of >10 would be necessary to detect and quantify the O_2 A band, 1.06 μm dimer feature and 1.27 μm feature for a true Earth analog. However, because continuum brightness changes with pressure, a different S/N criteria would be necessary for higher pressure atmospheres. For example, the continuum brightness near the O_2 A band is three times lower for the 10.0 bar cases than it is for the 0.1 bar cases. For most cases, a S/N of >7 would likely be sufficient to set a lower limit on the surface pressure using the 1.06 μm dimer feature.

Clouds and aerosols will also affect the detectability of absorption features. In transit transmission, clouds can effectively mask the highest pressures of the atmospheres at which dimer absorption is most prominent. However, in partially cloudy atmospheres some of the paths will probe pressures as high as the maximum tangent pressure, and thus the planetary transmission spectrum could show evidence of dimer absorption. Furthermore, absorption in the 1.27 μm dimer band can be detected with S/N>1 in even some 0.1 bar cases, meaning that there could be a detectable dimer absorption signal for even a completely cloud-covered planet if the cloud deck pressure was $\geq$0.1 bars. For reflected spectra, clouds will truncate paths before they reach the surface and limit the dimer absorption for those paths. However, for partially cloudy atmospheres, dimer absorption could be detectable in the paths that do reach the surface. Additionally, because cloud albedos are typically greater than surface albedos, the presence of clouds will increase the continuum brightness levels and the brightness in the center of absorption bands. The increase in brightness has been shown to decrease the required S/N to detect and characterize O_2 monomer absorption in cloudy atmospheres when compared to cloud-free cases (Evans *et al.*, 2011), though the effect of cloud albedo on the detectability of dimer absorption features has not been heretofore examined. Therefore, while clouds will impact the detectability of dimer features, using dimers to determine pressure and as biosignatures may still be feasible for cloudy atmospheres.

6.4.3 Detectability at Different Resolving Powers

Figures 6.20 shows the S/Ns for spectral features at varying resolving powers for transit transmission spectra of a 1.0 bar, 1.0x PAL O_2 atmosphere. The S/Ns for each band are greatest at the highest resolving powers, and then gradually decrease until R$\sim$60 or 80, at which the S/Ns decrease strongly. This dramatic decrease with resolving power occurs because at the lowest resolving powers, the absorption bands are indistinguishable from the continuum. Additionally, the highest flux levels in the continuum cannot be resolved at lower spectral resolving powers, decreasing the total signal. This effect can be seen most easily for the spectra with R=20, in which no absorption features can be identified.

Figures 6.22 and 6.23 show the S/Ns for the direct imaging reflected spectra. In contrast to Figure 6.20, these two figures show the required S/N to detect and characterize an absorption band, not the S/N that could be obtained with JWST. The required S/N to detect spectral features increases as resolving power decreases. However, this effect would be mitigated because the expected noise at each wavelength should decrease as resolving power decreases. The S/N required to quantify each absorption band decreases as resolving power decreases because the lowest radiance level increases. At R$<$40, however, spectral features are very difficult to identify, making these resolving powers unsuitable for detecting and characterizing O_2-related absorption features.

6.4.4 O_2 Dimer Biosignatures

In addition to their utility as pressure probes, the 1.06 μm dimer feature and 1.27 μm feature could potentially be detectable biosignatures for nearby Earth-like planets. The O_2 A band has long been considered the most viable O_2 biosignature, but it is unlikely to be the most detectable biosignature for an Earth-like planet in transit transmission. As initially described in (Pallé *et al.*, 2009), lunar eclipse observations show that the 1.06 μm and 1.27 μm dimer features are more detectable than O_2 monomer features like the A band, which is corroborated by our model spectra and detectability calculations. The 1.27 μm O_2 feature has been examined as a potential biosignature for ground-based telescopes by Kawahara *et al.* (2012), but to our knowledge detectability studies of neither the 1.06 μm dimer feature nor the 1.27 μm feature have been undertaken for JWST. Our results show that the 1.27 μm feature would be detectable with a S/N of 5 for a cloud-free Earth-analog at 5 pc. Therefore, we conclude that O_2 features, especially the 1.06 μm dimer feature and the 1.27 μm feature, could be detectable biosignatures for oxygenic photosynthesis with JWST.

6.4.5 Challenges to Observations

Clouds and aerosols will make estimating pressure using dimer features more difficult. A direct imaging observation of a partially cloud-covered planet will be able to probe to the surface for a fraction of the paths, such that the dimer feature will be weaker than for a cloud-free planet. Cloud and aerosol extinction can also be wavelength dependent, which may complicate using equivalent widths or ppm flux differences to determine pressure. Nevertheless dimer features can still provide a lower bound for pressure if clouds and aerosols cannot be explicitly included in the retrieval method.

Higher H_2O or CO_2 abundances in an atmosphere could also make this method more challenging. Higher H_2O abundances will make it more difficult to define a continuum for the 1.06 μm dimer feature, as shown in Figures 6.17 and 6.18. However, as discussed in

Section 6.3.4, the magnitude of this error should typically be less than 20% for most cases in which the 1.06 μm dimer feature could be detectable. CO_2 has an absorption feature near 1.06 μm (Segura *et al.*, 2007), which could make using the 1.06 μm dimer feature difficult. This could be overcome by modeling out absorption from H_2O and CO_2 or by using other dimer features to supplement information from the 1.06 μm dimer feature, such as the 1.27 μm dimer feature.

Lastly, not knowing the mixing ratio of O_2 will make estimating pressure difficult when only a reflected spectrum is available. This is similar to the problem in using the absorption widths of rotation-vibration features to constrain pressure. However, the 1.06 μm dimer feature is more sensitive to pressure than a monomer feature, and therefore can provide a better estimate of pressure than a monomer feature alone. Furthermore, monomer features cannot be used as an on/off pressure gauge, while dimer features can.

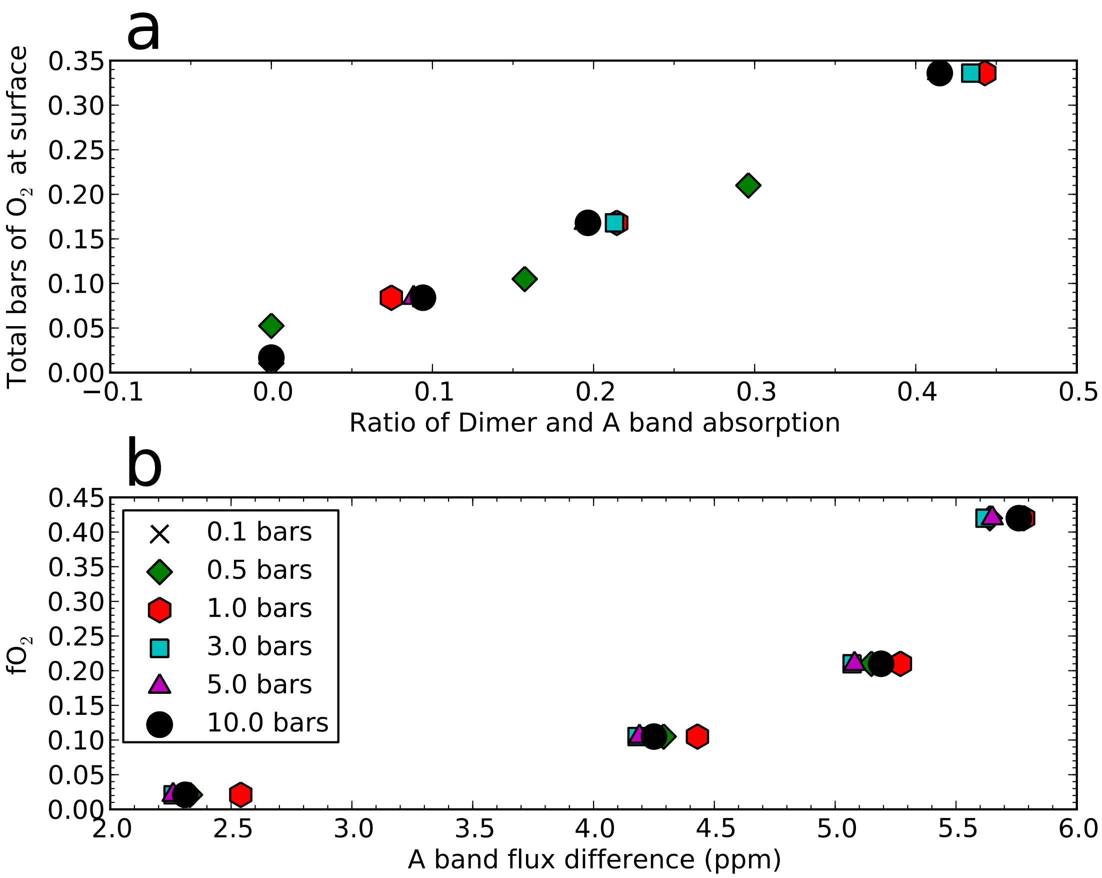

Figure 6.12: **(a)** O_2 partial pressure at maximum tangent pressure vs. the ratio of the dimer feature and O_2 A band flux difference ratio. The ratio can be used to determine the O_2 partial pressure. **(b)** fO_2 (or O_2 mixing ratio) vs A band flux difference. The A band flux difference is roughly constant for a given O_2 mixing ratio. The combination of the O_2 partial pressure and the O_2 mixing ratio allows for the surface (or cloud-top) pressure to be estimated.

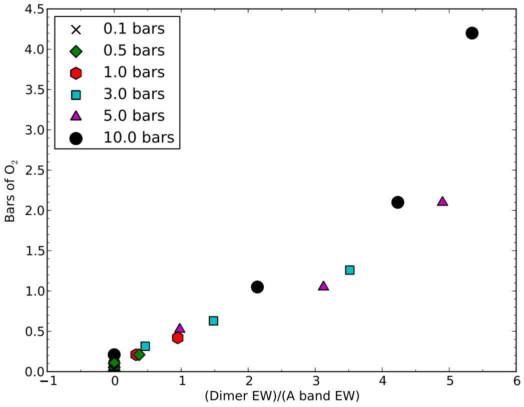

Figure 6.13: The total atmospheric O_2 is shown as a function of the ratio of the 1.06 μm dimer feature equivalent width to the O_2 A band equivalent width for the reflected spectrum. There is a trend between this ratio and the total amount of O_2. This could be used as a way to estimate the pressure if a transmission spectrum is not available.

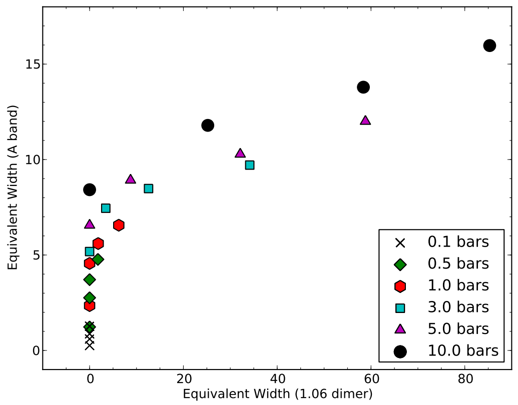

Figure 6.14: Atmospheric pressure as a function of the dimer and A band equivalent widths in the reflected spectrum for atmospheres with total pressures between 0.1 and 10 bars. It will be possible to set a lower bound on the pressure with only the O_2 A band equivalent width and the 1.06 μm dimer equivalent width.

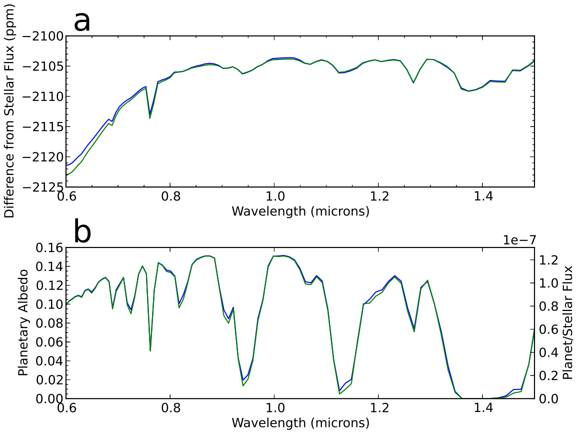

Figure 6.15: (**a**) Transit transmission spectra for the Earth (blue) and an isothermal atmosphere at 250 K with the same pressure-composition profiles (green). (**b**) Reflected spectra for an Earth analog with 2.0x PAL O_2 (blue) and an isothermal atmosphere at 250K with the same pressure-composition profiles (green). In both cases, the spectra for the calculated temperature-pressure profile and the isothermal profile are very similar, showing that the spectra are not strongly dependent on the temperature profile.

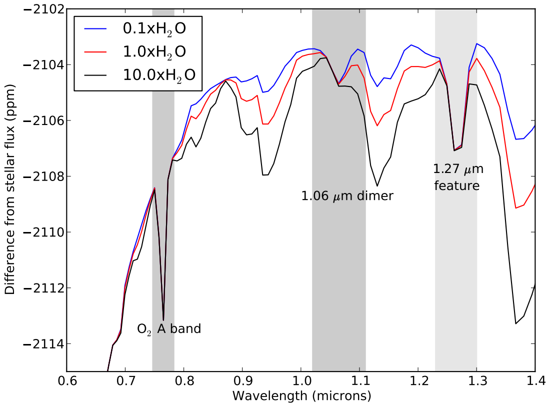

Figure 6.16: Transit transmission spectra of a 1.0 bar, 1.0x PAL O_2 Earth analog with H_2O concentrations varying from 0.1 to 10.0x PAL H_2O. While H_2O absorbs near the wings of the O_2 A band the ppm flux difference and the S/N do not change greatly as the H_2O concentration changes. The continuum near the 1.06 μm dimer feature is strongly affected by the increases in H_2O. However, the magnitude of the change in the ppm flux difference over the entire band and the S/N is less than 20% when comparing the 1.0x PAL H_2O case to either the 0.1 or 10.0x H_2O cases.

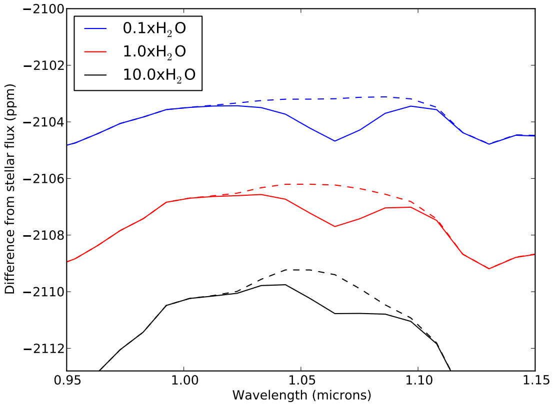

Figure 6.17: The 1.06 μm dimer feature in transit transmission with different amounts of H_2O. The spectra have been artificially offset for ease of viewing. The black dashed lines are spectra that do not include any O_2 dimer absorption and are included to help show the continuum flux level. The total ppm flux difference and S/N for the dimer band vary by less than 20% with respect to the 1.0xH_2O case.

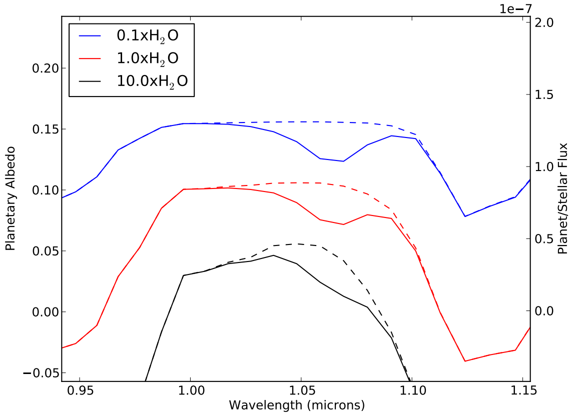

Figure 6.18: The 1.06 μm dimer feature in the direct beam reflected spectra with varying amounts of H_2O for an Earth analog with a 1.0 bar, 2.0x PAL O_2 atmosphere. There is an artificial offset for ease of viewing, and the black dashed lines are spectra that do not include any O_2 dimer absorption. As in transit transmission, the S/N of the dimer feature varies by less than 20% with respect to the 1.0x H_2O case. Additionally, the S/Ns for higher pressure cases should be less affected by changes in H_2O concentrations because of greater absorption within the dimer band.

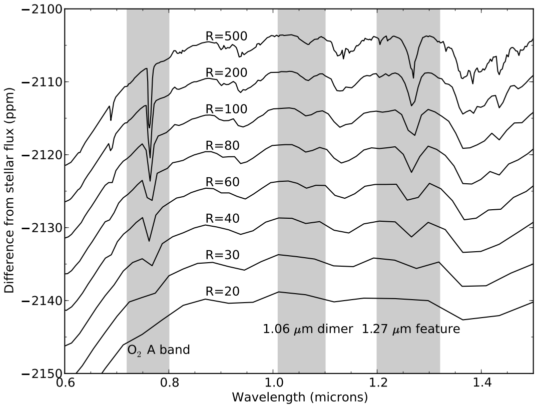

Figure 6.19: Transit transmission spectra for the 1.0 bar, 1.0x PAL O_2 case at various spectral resolving powers. The wavelengths for the O_2 A band, the 1.06 μm dimer band, and the 1.27 μm band are highlighted. An artificial offset has been added to the spectra for ease of viewing. At the lowest resolving powers, it is difficult to identify spectral features.

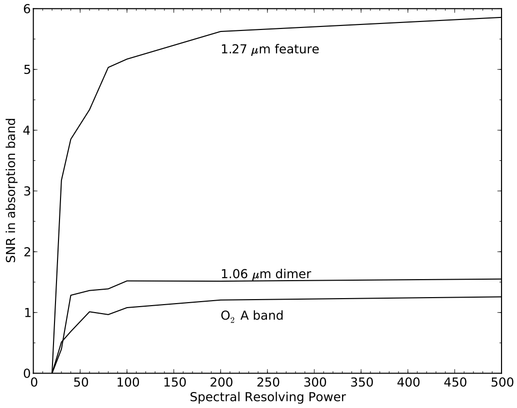

Figure 6.20: S/N ratios of absorption features for the spectra shown in Figure 6.19. The S/Ns decrease as resolving power decreases because the absorption bands can no longer be resolved from the continuum. For R=30 and R=20 it is very difficult to identify any of the O_2 spectral features.

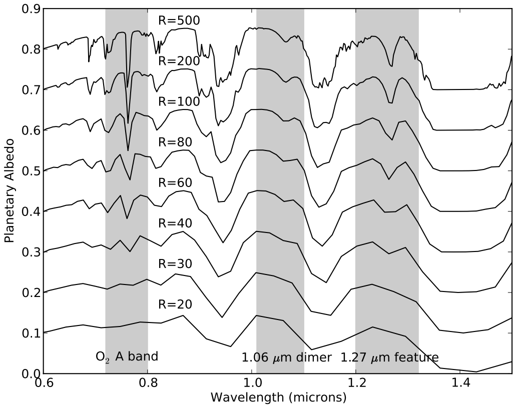

Figure 6.21: Direct imaging reflected spectra generated at spectral resolving powers from 500 to 20. The y-axis is the planetary albedo with an arbitrary offset added for ease of viewing. The O_2 A band, 1.06 μm dimer feature and 1.27 μm feature are highlighted. At resolving powers of R=30 and R=20 it is difficult to identify any O_2 absorption features.

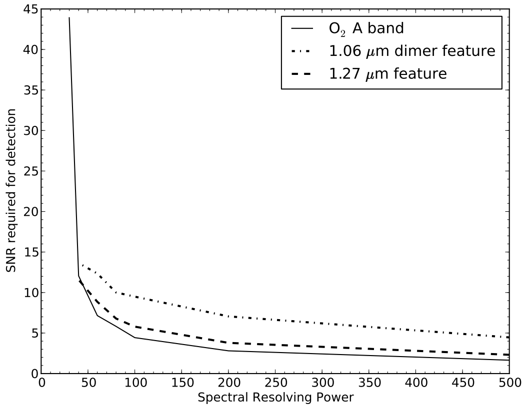

Figure 6.22: S/N ratios needed to detect the O_2 A band, 1.06 μm dimer feature and the 1.27 μm feature for direct imaging reflected spectra. As resolving power decreases, the required S/N to detect each feature increases because the continuum level decreases, resulting in a lower overall signal in the absorption band. Furthermore, at the lowest resolutions the absorption bands cannot be resolved. Thus, this decreases the measurable signal even more, leading to an increase in the required S/N.

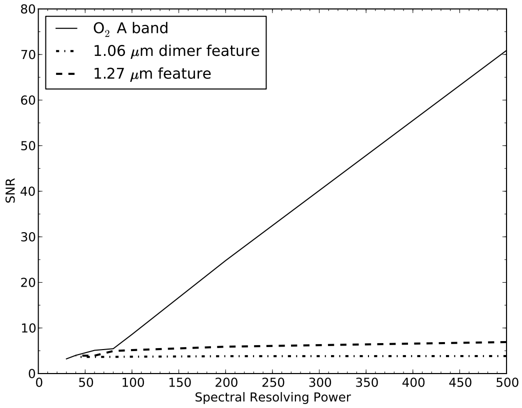

Figure 6.23: S/N ratios required to quantify the flux within 3σ in the center of the absorption band (defined as the lowest flux level) for the O_2 A band, 1.06 μm dimer feature and the 1.27 μm feature. The S/N required for this level of precision decreases as resolving power decreases because the flux is averaged over fewer wavelength bins, leading to an increase in the lowest flux. This decrease in required resolving power occurs for all three absorption features, though the trend is most apparent for the O_2 A band, as it has the narrowest spectral shape of the three features considered here.

Table 6.1: S/N ratios for the O_2 A band, the 1.06 μm dimer feature and the 1.27 μm feature for all the cases considered in both transit transmission and secondary eclipse. The calculations were done for an Earth analog orbiting an M5V star at a distance of 5 pc. The total integration time was assumed to be 10^6s, equal to the total amount of time spent in transit for this case over JWST's 5 year mission lifetime. The 1.06 μm dimer feature and the 1.27 μm feature could be detectable, allowing a lower limit for atmospheric pressure to be set.

Pressure	fO_2	Transit Transmission			Secondary Eclipse		
Bars	PAL	O_2 A band	O_2-O_2 1.06 μm	O_2 1.27 μm	O_2 A band	O_2-O_2 1.06 μm	O_2 1.27 μm
0.1	0.1	0.2	0.0	0.0	5.2e-04	0.0e+00	2.7e-03
0.1	0.5	0.5	0.0	0.9	1.2e-03	0.0e+00	3.4e-03
0.1	1.0	0.6	0.0	1.2	1.7e-03	0.0e+00	4.2e-03
0.1	2.0	0.8	0.0	1.5	2.4e-03	0.0e+00	5.5e-03
0.5	0.1	0.5	0.0	1.1	2.3e-03	0.0e+00	5.5e-03
0.5	0.5	0.8	0.0	2.5	5.0e-03	0.0e+00	1.2e-02
0.5	1.0	1.1	1.2	3.7	6.7e-03	0.0e+00	1.8e-02
0.5	2.0	1.1	2.3	5.1	8.5e-03	1.2e-02	2.7e-02
1.0	0.1	0.5	0.0	1.6	4.1e-03	0.0e+00	9.5e-03
1.0	0.5	0.8	0.5	3.9	7.8e-03	0.0e+00	2.6e-02
1.0	1.0	1.1	1.5	5.2	9.4e-03	1.3e-02	3.9e-02
1.0	2.0	1.1	3.4	7.5	1.1e-02	3.5e-02	6.3e-02
3.0	0.1	0.5	0.0	1.2	7.3e-03	0.0e+00	3.2e-02
3.0	0.5	0.8	0.6	3.5	1.0e-02	2.1e-02	8.4e-02
3.0	1.0	1.1	1.5	5.0	1.1e-02	6.2e-02	9.9e-02
3.0	2.0	1.1	3.5	7.2	1.2e-02	1.5e-01	1.2e-01
5.0	0.1	0.5	0.0	1.1	7.5e-03	0.0e+00	5.8e-02
5.0	0.5	0.8	0.6	3.3	9.6e-03	4.3e-02	1.1e-01
5.0	1.0	1.1	1.4	4.9	1.1e-02	1.2e-01	9.4e-02
5.0	2.0	1.1	3.3	7.2	1.2e-02	2.1e-01	1.1e-01
10.0	0.1	0.5	0.0	1.1	5.9e-03	0.0e+00	9.2e-02
10.0	0.5	0.8	0.7	3.4	7.8e-03	9.3e-02	6.1e-02
10.0	1.0	1.1	1.4	5.0	8.6e-03	1.7e-01	6.1e-02
10.0	2.0	1.1	3.4	7.4	9.0e-03	2.1e-01	5.0e-02

Table 6.2: S/N ratios for detection (S/N_D) and to obtain precision of 3σ in the center of the band (S/N_P) for the O_2 A band, the 1.06 μm dimer feature and the 1.27 μm feature at pressures ranging from 0.1 to 10.0 bars and O_2 concentrations ranging from 0.1 to 2.0 times PAL O_2 for direct imaging reflected spectra.

Pressure	fO_2	O_2 A band		1.06 μm dimer		1.27 μm feature	
Bars	PAL	S/N_D	S/N_P	S/N_D	S/N_P	S/N_D	S/N_P
0.1	0.1	>100	3.1	-	-	-	-
0.1	0.5	50.0	3.2	-	-	>100	3.0
0.1	1.0	35.0	5.4	-	-	>100	5.1
0.1	2.0	24.4	3.4	-	-	89.8	3.1
0.5	0.1	25.1	3.4	-	-	>100	3.1
0.5	0.5	11.4	3.9	-	-	38.8	3.2
0.5	1.0	8.6	7.3	-	-	23.8	5.6
0.5	2.0	6.8	5.0	30.9	3.2	14.3	3.7
1.0	0.1	13.4	3.8	-	-	62.0	3.1
1.0	0.5	7.1	4.8	-	-	16.4	3.6
1.0	1.0	5.8	9.1	29.0	5.4	9.9	6.9
1.0	2.0	5.0	6.1	9.6	3.7	5.9	5.4
3.0	0.1	6.2	5.3	-	-	12.8	3.8
3.0	0.5	4.4	6.9	16.5	3.4	4.3	7.2
3.0	1.0	3.9	13.2	4.9	8.1	2.9	26.7
3.0	2.0	3.5	9.4	1.9	18.9	1.7	>100
5.0	0.1	5.0	6.3	-	-	6.5	5.0
5.0	0.5	3.8	8.6	6.8	4.1	2.7	20.9
5.0	1.0	3.4	17.7	2.3	18.1	1.9	>100
5.0	2.0	3.0	15.2	1.3	>100	1.3	>100
10.0	0.1	4.1	8.1	-	-	3.0	13.7
10.0	0.5	3.0	15.2	2.3	10.4	1.8	>100
10.0	1.0	2.7	44.9	1.4	>100	1.2	>100
10.0	2.0	2.4	61.6	1.0	>100	1.0	>100

Chapter 7

BIOSIGNATURE AND HABITABILITY MARKERS IN TRANSIT TRANSMISSION SPECTROSCOPY: DETECTING VOLCANISM ON EXOPLANETS USING TRANSIENT SULFATE AEROSOLS

Volcanism is an important process for a habitable worlds, yet existing methods to characterize volcanism in an exoplanet atmosphere focus on searches for gases that are difficult to detect. In this chapter, I present a new method for detecting volcanic eruption on exoplanets using transient sulfate aerosol signals. On the Earth, explosive volcanic eruptions can inject SO_2 into the stratosphere, where it can photochemically react to form H_2SO_4 aerosols, which gradually fall out over time. This results in a relatively rapid increase in the effective absorbing radius of the planet across a broad range of wavelengths, followed by a gradual decrease in effective absorbing radius. Here I quantify this effect for Earth-like atmospheres and show that this could be detectable for nearby planets orbiting M dwarfs with JWST or E-ELT. I also examine potential false positives, the possible connection between transient sulfate aerosols and plate tectonics, and how a detection of transient sulfate aerosols can strengthen the case for biotic oxygen. Portions of this chapter have been submitted to *Astrobiology* in collaboration with J. Krissansen-Totton, M. Koehler and S. F. Sholes.

7.1 Introduction

Geologically active worlds are more favorable environments for the emergence and persistence of life than geologically dead worlds. On Earth, geological activity was likely important for both the genesis of life and its long-term maintenance. A *de novo* genesis of life appears to be reliant on chemical potential and redox gradients that were common in volcanic and hydrothermal settings during the Hadean and early Archean (Sleep *et al.*, 2011; Stüeken *et al.*, 2013). Subaqueous hydrothermal vents powered by serpentinization of oceanic crust generated broad pH gradients ($\sim$6 for seawater to 9-11 for venting fluids) providing geochemically free energy for nascent life on early Earth (Sleep *et al.*, 2011). Serpentinization also creates organic carbon molecules through Fischer-Tropsch-like reactions that may have been necessary for incipient biochemistry (Holm and Charlou, 2001; Stüeken *et al.*, 2013). Furthermore, modern life uses coupled redox pairs for electrochemical energy, and relies on "ion-tight" membranes and membrane enzymes to maintain disequilibrium (Mulkidjanian *et al.*, 2012). As the earliest organisms could not have had these complex membranes, it is thought that environmental redox gradients, such as those that can be found in hydrothermal systems, could have supported protocells (Mulkidjanian *et al.*, 2012; Stüeken *et al.*, 2013). Additionally, the overwhelming majority of electron donors and acceptors involved in early Earth ecosystems, and likely the origin of life, were sourced from subaerial and subaqueous volcanoes as well as hydrothermal systems (Canfield *et al.*, 2006) that may have been commonly associated with plate boundaries.

Geological activity may also help maintain long-term habitability by replenishing bioessential elements and by controlling climate stability. Nisbet and Sleep (2001) point out that if it were not for the perpetual supply of erodible rocks and steady introduction of volcanic cations, life would have slowly diminished due to a lack of bioessential elements. The long-term carbonate-silicate cycle, a product of plate tectonics, has regulated the concentration of CO_2 in Earth's atmosphere throughout geologic time (Walker *et al.*, 1981). Climate stability may also potentially be maintained in a stagnant lid regime (Pollack *et al.*, 1987b), but crucially, at least some volcanic outgassing is required to replenish the drawdown of CO_2 by silicate weathering and prevent the onset of a snowball.

Given the importance of geological activity for the origin and persistence of life, observational techniques capable of detecting volcanic activity could inform the habitability of terrestrial exoplanets. Geological activity may not be an absolute requirement for life in the same way that free energy and a liquid solvent are required; for instance, it is conceivable that the subsurface oceans of icy-moons sustain life from surface oxidants alone (McKay *et al.*, 2008). However extrasolar astrobiology is primarily focused on habitable environments that can be observed and characterized (Des Marais *et al.*, 2002), and realistically only large-biomass, high metabolism surface biospheres that persist for geologically significant timescales will be detectable on exoplanets. Geological activity is necessary for the genesis and maintenance of such biospheres. We propose that transient sulfate aerosols could be suggestive of volcanic activity. Thus the detection of transient sulfate aerosols would help inform habitability evaluations and identify promising candidates for follow-up observations.

Currently, there is limited understanding of how we might determine whether exoplanets have active volcanism. Identifying volcanically produced gases is one proposed method to infer active volcanism on an exoplanet. Volcanic gas emissions are primarily composed of H_2O, H_2, CO_2, CO, SO_2, and H_2S. Of these, only SO_2 and H_2S are known to be found in large concentrations almost exclusively as the result of volcanic activity. Jackson *et al.* (2008) suggested that highly tidally heated planets could have sulfur-rich atmospheres. This is similar to what is seen in the solar system, in which Jupiter's moon Io is tidally heated and erupts sulfur-bearing gases. For these planets, the detection of sulfur species (such as SO_2) could be indicative of active volcanism. Kaltenegger *et al.* (2010) used SO_2 as an atmospheric proxy for detecting moderate to high amounts of explosive volcanism on exoplanets. They found that SO_2 absorption from eruptions 100x larger than the 1991 Pinatubo eruption could be detectable (signal to noise ratio, S/N, >3) in primary (transit) or secondary eclipse with JWST for an exoplanet closer than 2.5 pc. Their results indicate that SO_2 will only be detectable as tracer for volcanism for very large, infrequent (once every >10,000 years) eruptions and only for planets orbiting the 6 closest stars, so the utility of SO_2 as a practical tracer for volcanism is limited. Furthermore, Hu *et al.* (2013) have examined the photochemistry of volcanically-produced gases over a range of atmospheric compositions and found that large surface fluxes of H_2S and SO_2 lead to the formation of sulfur-based aerosols rather than larger mixing ratios for either gas. Thus, it is unlikely that either H_2S or SO_2 would serve as a detectable proxy for volcanism.

We present a new method that relates the detection of temporal variations in stratospheric sulfate aerosols to active volcanism. On Earth, explosive volcanic eruptions (typically with a Volcanic Explosivity Index (VEI)>4) can inject SO_2 directly into the stratosphere, where it photochemically reacts with water to form sulfuric acid aerosols with lifetimes ranging from months to years. Stratospheric aerosols resulting from volcanism have been studied extensively in the Earth's atmosphere, typically with regards to their effect on climate forcing (Lacis *et al.*, 1992; Sato *et al.*, 1993), but here we examine their spectral effects. In the results section we show that these spectral effects would be detectable through observation of transiting terrestrial exoplanets. This work only demonstrates the feasibility this technique using Earth as a case study; we model transit transmission spectra for an exoplanet with the same mass, radius, bulk composition, atmospheric composition and time-averaged insolation as Earth. However, the technique should be applicable to a broad range of terrestrial planets and host stars (see Discussion). The Discussion section also considers the possible connections between transient stratospheric aerosols and plate tectonics.

7.2 Methods

We generated transit transmission spectra of the Earth to test the detectability of transient stratospheric sulfate aerosols as a sign of active volcanism. We used the model described in Chapter 2, but ignored the effect of forward scattering because this is predicted to have a small effect for planets in the habitable zone of any main sequence star (see Chapter 5). However, refraction was included in our calculations. We assumed Earth-like bulk composition, radius, mass and atmospheric composition. We placed the Earth-analog planets around a Sun-like star and an M5 star at the flux equivalent distance, which is the distance from the host star that the planet would receive the same bolometric flux as the Earth receives from the Sun. As sulfate aerosol abundance increases, the atmosphere becomes more opaque in transit transmission, resulting in higher effective absorbing radii. We used a radiative transfer model with standard pressure-temperature profiles and gas mixing ratio profiles, along with aerosol data retrieved from Earth-observing satellites, to generate the spectra. We also adopted different cloud schemes to cover a range of possible exoplanet cloud fractions and cloud altitudes. The effect of refraction was included for the spectra generated in this chapter, though the effect of forward scattering was not. As shown in Chapter 5, forward scattering in transit transmission has a negligible effect for planets in the habitable zone. Therefore, not including forward scattering in the models should not greatly impact the results presented below. Our model and model inputs are described below in greater detail.

We modeled the Earth using the tropical, mid-latitude and subarctic reference models at different seasons from McClatchey *et al.* (1972). We used the prescribed pressure-temperature profile, H_2O, and O_3 mixing ratio profiles and assumed that CO_2, N_2O, CO, CH_4, and O_2 are evenly mixed in all cases. We used the tropical atmosphere model for latitudes $-23^\circ < l < 23^\circ$, the mid-latitudes atmosphere for $-60^\circ < l < -23^\circ$ and $23^\circ < l < 60^\circ$, and the subarctic atmosphere for $-90^\circ < l < -60^\circ$ and $60^\circ < l < 90^\circ$.

We used data from the Stratospheric Aerosol and Gas Experiment (SAGE) II (McCormick, 1987) and Optical Spectrograph and Infrared Imager System (OSIRIS) (Llewellyn *et al.*, 2004) to model the aerosol optical depth over time. For background aerosol levels, we used an aerosol profile from McCormick *et al.* (1996) from 1979, which followed a period of low levels of volcanic activity and is therefore a reasonable approximation for background aerosol levels. We confirmed that this extinction profile matches background aerosol extinction profiles measured by SAGE II and OSIRIS. For small eruptions (total aerosol optical depth (AOD) $\sim <$ 10x background levels), the extinction profile roughly scales by the aerosol optical depth without any change in the shape of the vertical profile. Therefore, we assumed the same vertical aerosol profile in the stratosphere but scaled the extinction up by the factor of increase in AOD. For larger eruptions with AOD $>$ 10x background levels, we use the average aerosol vertical profiles retrieved by SAGE II and Osiris for each month and each latitude bin.

To model the extinction from aerosol particles we used the Bohren and Huffman (1983) Mie scattering code to calculate wavelength-dependent absorption and scattering. For small eruptions, we assumed the stratospheric aerosols were 75% H_2SO_4 particles with a lognormal size distribution with an effective radius of 0.2 μm (from SAGE data) and an effective variance of 0.07 μm^2 (Hansen and Travis, 1974), though we find our results are not strongly dependent on the effective variance. We used the Palmer and Williams (1975) optical constants for 75% H_2SO_4 solutions to generate the Mie scattering output. We also generated wavelength-dependent optical properties for larger effective radii, which are applicable to large eruptions like Pinatubo. Larger eruptions lead to larger particle sizes (English *et al.*, 2013), and for the Pinatubo eruption the maximum mean particle size is 0.6 μm.

For each month in the dataset, we generated a transmission spectrum for each of the six latitude bins. We averaged the aerosol optical depth over respective latitudinal bins (e.g. northern tropical latitudes) and generated a monthly spectrum over each bin using (a) the reference model atmosphere, (b) the retrieved aerosol extinction profile from SAGE II, and (c) an assumed cloud structure. We considered three cloud cases: (1) no clouds, so that it is possible to probe to the surface, (2) realistic clouds with an opaque cloud deck at 6 km with 100% cloud coverage, and an opaque cirrus cloud deck at 10 km with 25% cloud coverage, and (3) complete cloud coverage at the tropopause or at 10 km, whichever was greater. We include cases 1 and 3 to demonstrate the maximum possible effect of variations in cloud coverage on variations in the transit spectrum for an Earth-like atmosphere. For the realistic cloud coverage case, we adopted 100% cloud coverage at 6 km because even clouds that are considered optically thin in direct beam can be optically thick in transit transmission due to the increased path length in limb geometries. Other tropospheric aerosols, such as dust, pollution and products of biomass burning also contribute to tropospheric opacity and will generally be optically thick below 6 km (Winker *et al.*, 2013).

7.3 Results

We generated spectra for the Earth over time with realistic cloud coverage and aerosol loading as an analog for future exoplanet observations. Figure 7.1 shows spectra of the Earth for three different aerosol loadings: background aerosol levels, and levels corresponding to peak aerosol optical depth following the 1991 Mt. Pinatubo eruption and the 2009 Sarychev eruption with realistic clouds included for an Earth-analog planet orbiting an M5V star. Details about the eruptions can be found in Table 7.1. We chose Sarychev to represent a small eruption and Pinatubo to represent a large eruption because the Sarychev is one of the largest ‘small’ eruptions (with AOD$<$10x background levels at all latitudes) and Pinatubo is the large eruption best studied by Earth-observing satellites. These spectra show that the effects of volcanic eruptions on the Earth’s spectrum are significant. The Sarychev eruption leads to changes in the spectra predominantly between 0.4 and 1.35 μm, while the Pinatubo eruption leads to changes at all wavelengths. The difference in the wavelengths affected is because the average aerosol particle size was 0.5 μm for the Pinatubo eruption, as opposed to 0.2 μm for the Sarychev eruption. The Pinatubo eruption also led to larger changes in the spectrum because of the increased aerosol loading.

Figure 7.2 shows the mean effective absorbing radius over time for the periods of the

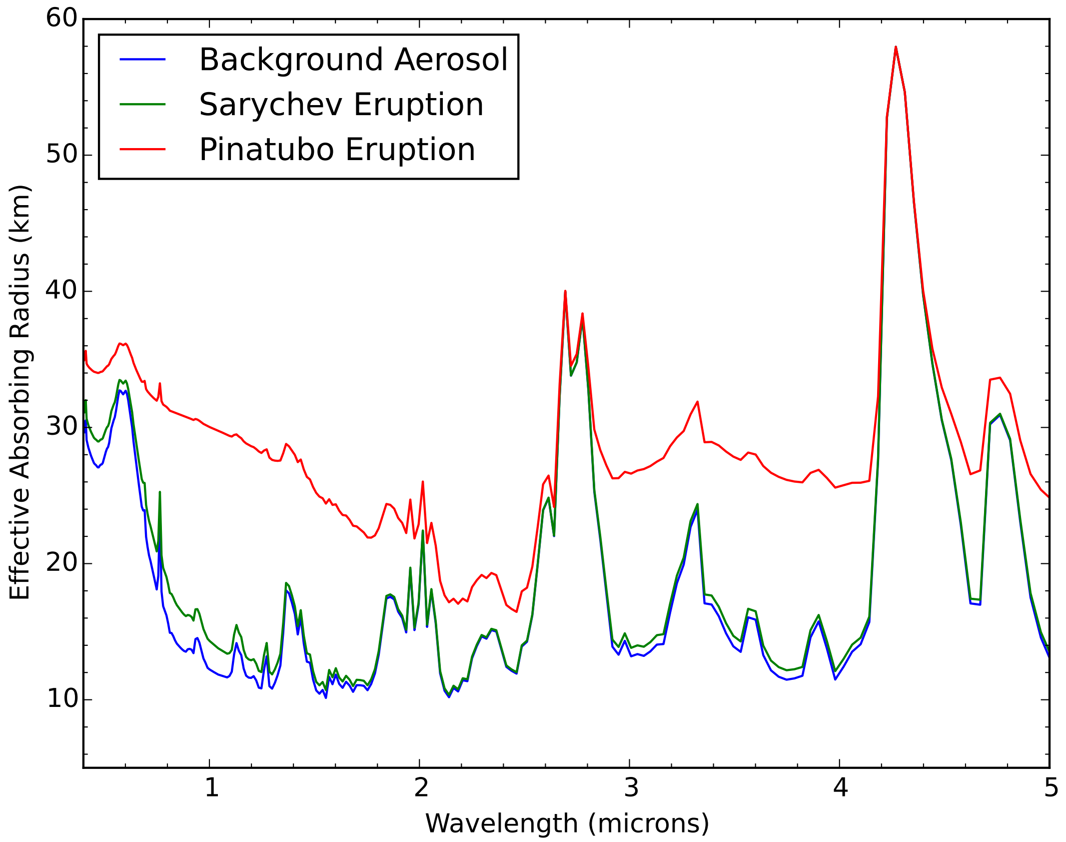

Figure 7.1: Spectra (in effective absorbing radius of the atmosphere) of the Earth during different amounts of aerosol loading: with background aerosol levels, after the 2009 Sarychev eruption and after the eruption of Mt. Pinatubo in 1991. The spectra are shown for the period after the eruption when the aerosol loading was greatest. While the effect of increased aerosol loading on the Earth's spectrum is small for the Sarychev eruption, it is large (>20 km) for the Pinatubo eruption. The wavelength cutoffs are 0.4 microns (at which noise levels increase for ground-based observations) and 5.0 microns (the longward cutoff for JWST NIRSPEC). If multiple transits can be binned over, we find that it may be possible to detect (S/N>3) a Pinatubo-sized eruption with JWST or a Sarychev-sized eruption with E-ELT for an Earth-analog planet orbiting an M5 star. A Pinatubo-sized eruption should be detectable with E-ELT with S/N>7 for both the Sun-like and M5V case, even without multiple transits binned over.

Table 7.1: Eruption Parameters

Eruption	Date	VEI	SO_2 (Tg)	Plume Height (km)
Krakatoa	Aug 1883	6	2.9 (Devine *et al.*, 1984)	$>$40 km (Self and Rampino, 1982)
Agung	Feb 1963	5	2.5-7 (Self and King, 1996)	$>$20 km (Self and King, 1996)
El Chichón	Mar-Apr 1982	5	8 (Thomas *et al.*, 1983)	$\sim$17 km (Varekamp *et al.*, 1984)
Pinatubo	Jun 1991	6	20 (Bluth *et al.*, 1992)	$>$40 km (Oswalt *et al.*, 1996)
Sarychev	Jun 2009	4	1.2 (Haywood *et al.*, 2010)	$\sim$14 km (SVERT[1])

Pinatubo eruption and for all eruptions post-2000 for the three different cloud schemes we modeled. This figure shows that the mean effective radius of the atmosphere (measured as the mean spectral value between 0.685 and 1.40 μm, or over the i and j bands) increases as the aerosol optical depth (normalized to background levels) increases. This is because for higher aerosol optical depths, the atmosphere becomes more opaque and is absorbing a great quantity of light. Figure 7.2 also shows the difference in effective absorbing radius between the different cloud schemes. The difference in effective absorbing radius from the realistic cloud case is 1.5-2 km for the two more extreme cases. In contrast, the changes in absorption for the Sarychev and Pinatubo eruptions are 1.5 and 10 km, respectively. While the change due to the Sarychev eruption is similar to a theoretical change in cloud coverage, it is unlikely that the global cloud coverage would change by 100%. The Pinatubo eruption is of sufficient magnitude to preclude any confusion with changes in cloud coverage, cloud height (up to the 10-15 km levels tested), or both.

Finally, we note that there is observational evidence to support our model results. Increased aerosol loading in Earth's atmosphere leads to darker and redder lunar eclipses (Keen, 1983). Transit transmission spectra of exoplanets probe geometries similar to those seen in lunar eclipse; the passage of sunlight through Earth's limb (and subsequent reflection from the moon) is analogous to the passage of light through an exoplanet's limb during

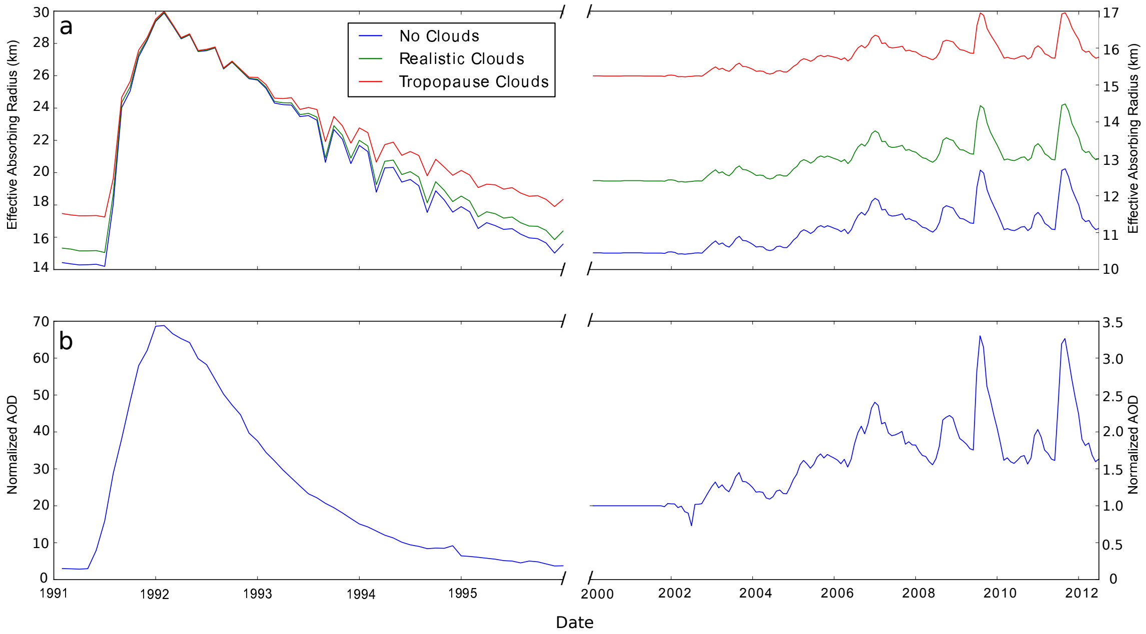

Figure 7.2: a) Mean effective radius for different cloud types and b) aerosol optical depth (normalized to background aerosol levels in early 2000's) over time. Note the different y-axis scales for the left and right hand sides. The mean effective radius of the atmosphere increases as aerosol optical depth increases. This figure also shows that the change in effective radius between different cloud schemes is smaller than the change due to volcanic eruptions for a large eruption like Pinatubo. The change due to a Sarychev-type eruption is roughly equal to 100% changes in cloud coverage between the realistic case and either of the end-member cases.

transit (Pallé *et al.*, 2009). Thus, increases in stratospheric aerosol concentration due to volcanism should lead to changes in the transit transmission spectrum of an exoplanet.

7.4 Observing Eruptions

7.4.1 Required Time Resolution

The lifetime of stratospheric aerosols in the Earth's atmosphere is on the order of months to years. For smaller eruptions, the spectral effect of the aerosols will only last a few months, meaning that detecting an eruption would require time resolution on the order of months. In transit transmission we can only observe the spectrum of a planet once every exoplanet year. This means that Earth-like planets orbiting Sun-like stars will likely not be good candidates for observing smaller eruptions. The best candidates will be potentially habitable planets orbiting smaller M dwarf stars, which can have periods that are <1 month. For larger eruptions, longer timescales could be appropriate. The effect of the Pinatubo eruption on the Earth's spectrum lasted for $\sim$4 years. This means that detecting large eruptions should be possible for habitable planets orbiting Sun-like or smaller stars.

7.4.2 Prospects for Detectability

We used the JWST and E-ELT ETC's to estimate the detectability of transient sulfate aerosols, following the methodology described in Chapter 2. We calculated the noise level obtainable with one transit for the case of a small (an analog Sarychev) eruption and a large (analog Pinatubo) eruption orbiting Sun-like stars and M5V stars at a distance of 10 pc. To estimate detectability of Earth-analog planets orbiting Sun-like stars, we used the given model stellar spectra (G2V Phoenix or Pickles models) and normalized the star's flux to have a V magnitude of 4.83. For estimating detectability for Earth-analog planets orbiting M5 stars, we used a Phoenix stellar model (Hauschildt *et al.*, 1999) with an effective temperature of 2800 K, a surface gravity of 10^5 cm s^{-2}, and a solar metallicity. We normalized the flux of the M5V star to 5.22E-14 erg/s/cm^2/Angstrom at 1 μm, which is equivalent to a flux of 174 mJy. The V magnitude of the M5 star is 14.4. The E-ELT ETC does not have an option for user-input spectra, so we calculated the estimated noise at each wavelength by converting the model stellar flux to mJy and running the ETC simulation. We assumed a transit duration of 13 hr and an orbital period of 1 year for the Sun-like case, and a transit duration of 1.58 hr and an orbital period of 11.5 days for the M5V case.

Small, Sarychev-sized eruptions may be at the threshold of detectability for E-ELT, but will not be detectable with JWST. The signal levels at 1 μm (with refraction included) for a small eruption for an Earth-like planet around a Sun-like star and an M5 star are 0.02 ppm and 0.74 ppm, respectively. However, the signal from stratospheric aerosols covers a very wide wavelength range. In Figure 7.2 we've averaged the change in effective radius over a wide wavelength range. For E-ELT, we selected 70 wavelength bins between 0.68 and 1.38 μm in which atmospheric transmission is fairly large, allowing for high-precision ground-based observations. Shortward of 0.68 μm, M dwarfs have very low flux levels (and therefore large noise levels), and longward of $\sim$1.35 μm, there is a strong water absorption band that severely limits ground-based observations. For JWST, we selected all wavelength bins between 0.6 μm and 5.0 μm, which covers the full wavelength range of the NIRSPEC instrument in single prism mode. Assuming photon-limited noise (which should be appropriate for the bright stars that are likely targets for transit transmission spectroscopy), integrating the S/N over multiple wavelengths should be possible. Roughly, if N wavelength bins are integrated over, the noise will decrease by a factor of $\sqrt{N}$ if the noise is photon-limited. The overall S/N for a small eruption is much less than 1 with JWST. The S/N is 1.3 for the Earth-Sun case and 0.9 for the Earth-M5 case for observations with E-ELT. For the M dwarf planet, because the orbital period is relatively short (11.5 days), it could be possible to average over 9 transits (a total of 3.25 months of time) to get to a S/N of $\sim$3, which could be enough for a detection. Nevertheless, the spectroscopic effects of the 2009 Sarychev eruption would be at the threshold of detectability of E-ELT.

A Pinatubo-style eruption should be detectable for an Earth-like planet at a distance of 10 pc, perhaps even with JWST. The S/N at the height of the Pinatubo eruption would be 2.1 and 1.8 with JWST and 12.1 and 7.1 with E-ELT for the Sun-like and M5 case, respectively, even without any transits co-added. The effect of a Pinatubo-magnitude eruption lasts for $\sim$4 years, so increasing S/N by co-adding transits should be feasible. For example, for an Earth-analog orbiting a Sun-like star, if the peak of the eruption was observed, the S/N for that 1 transit with JWST would be 2.1 If a second transit were observed one year later, the S/N for the second transit would be 1.2. The third and fourth transit would have S/Ns of 0.7 and 0.4, respectively. Integrating over all transits would yield a best case S/N of 2.6. For a ‘worst case’ scenario, in which the peak is not observed, the total S/N for the Earth-analog orbiting a Sun-like star would be $\sim$2.0. For an Earth-analog orbiting an M dwarf, multiple transits could potentially be observed each month, greatly increasing the S/N. There are over 130 potential transits for the M dwarf case over a 4 year period, and by integrating over all possible transit the total S/N with JWST for an Earth-analog orbiting an M5 star would be 11.8. Even if only one transit per month could be observed, the total S/N would be 7.3 with JWST. Similar binning over transits could be done with E-ELT observations as well. Therefore, if we observe an Earth-like exoplanet that is undergoing a Pinatubo-magnitude eruption we could detect the effects of that eruption with E-ELT and possibly JWST.

While JWST and E-ELT may be able to detect transient sulfate aerosols for planets within 10 pc, larger telescopes would be required to detect this effect for planets further away. There are 67 stars within 5 pc, of which 50 are M dwarfs and 10 are F, G, and K stars (Cantrell *et al.*, 2013). An Earth-analog orbiting a Sun-like star has a $\sim$0.5% probability of transiting, and an Earth-analog orbiting an M dwarf has a $\sim$2% probability of transiting, meaning there is likely only 1 potentially habitable transiting planet within 5 pc, if every star hosts a potentially habitable planet. Kopparapu *et al.* (2013) estimates a habitable zone (HZ) planet occurrence rater of near 0.5, which would result in an average of 0.5 potentially habitable planets within 5 pc. There are 322 main sequence stars out to 10 pc, of which 248 are M dwarfs (Henry *et al.*, 2006), increasing the number of potential transiting planets out to 10 pc to $\sim$8 (or 4 assuming 0.5 HZ planets per star). Thus, the applicability of the technique described here to JWST and E-ELT will likely be limited to a small number of targets. However, this method would be applicable to more stars than the Kaltenegger *et al.*

(2010) method, which, as previously stated, only works for the 6 closest stars (within 2.45 pc) for transit transmission observations, among which there is a very low probability of having even one transiting, potentially habitable planet. Furthermore, the Kaltenegger *et al.* (2010) calculations assume that it is possible for a large amount of SO_2 to build up in an Earth-like atmosphere, which has been shown to be implausible by Hu *et al.* (2013). They show that large abundances of SO_2 and H_2S lead to aerosol formation, and therefore these gases are not predicted to build up to detectable levels. However, the presence of an aerosol layer alone is not predictive of volcanism on an exoplanet. This leaves transient sulfate aerosols as the most detectable signature of exovolcanism.

This method will likely be more applicable to the next generation of ground and space-based telescopes after JWST and E-ELT. Within 30 pc, there would be $\sim$100 (4x3^3, accounting for increase in volume) potentially habitable targets, greatly increasing the likelihood of a detection of transient sulfate aerosols. However, a detection at a distance of 30 pc is most likely not feasible with JWST or E-ELT, meaning that this technique may be most applicable to future large aperture space and ground-based telescopes. Given that observations of a star at 30 pc collect 1/9th the light of a star at 10 pc, detecting transient sulfate aerosols for a planet at 30 pc would require a telescope with nearly an order of magnitude greater collecting area than the next generation of space- and ground-based telescopes.

7.5 Discussion

Our results show that explosive volcanic eruptions can lead to changes in the transit transmission spectrum of the Earth, and that these changes could be detectable on exoplanets with E-ELT, and potentially JWST. From what is seen in solar system observations, the most likely explanation for transient aerosol loadings is volcanism. There are processes both inside and outside the Solar system that can potentially mimic a transient rise in sulfate aerosols as observed in transit transmission spectra. Below we address potential false positives and false negatives. The connections between explosive eruption and both large transient sulfate aerosol loading in the stratosphere and plate boundaries on Earth are also discussed below. We also address the feasibility of using these aerosol signals in the presence of oxygen as an oxygenic biosignature.

7.5.1 Potential False Positives and False Negatives

Martian dust storms exhibit similar patterns of sharp increases in aerosol levels, followed by a gradual decrease with timescales ranging from months to years (Pollack *et al.*, 1979). Dust storms could thus cause a potential false positive for detecting changes in stratospheric sulfate aerosols. Silicate absorption features near 9.7 and 3.4 μm could be used to distinguish between a dust storm and an increase in sulfate aerosols (Grishko and Duley, 2002). Additionally, on Earth, dust storms do not reach the stratosphere at the level that sulfate aerosols do, so it may be that large planet-wide dust storms like those we see on Mars require a thin, low pressure atmosphere.

If silicate absorption features will be used to distinguish between dust storms and explosive eruptions, then silica ash ejected into the atmosphere during eruptions must be ruled out as a false negative. Generally, volcanic ash rapidly (within days) falls out of the atmosphere, and does not become as geographically dispersed as the associated H_2SO_4 aerosols (Prata and Kerkmann, 2007; Karagulian *et al.*, 2010; Schneider *et al.*, 2012). Therefore, the effect of ash on the spectrum should be minimal and short-lived and will not significantly alter the results. Even in the unlikely scenario of an observation being made immediately following an eruption, when ash levels are high, and even if the ash cloud were on the planet's terminator (a requirement for having an effect on the transit transmission spectrum), the geographical extent would be small, extending to a few degrees in latitude and longitude at most, meaning that its effect on the spectrum would be very small.

However, this rapid fallout does not include particles that are smaller than 1 μm (Schneider *et al.*, 2012). On Earth, these smaller particles (a very small percent of the total ejected ash) can accompany SO_2 into the stratosphere and have residence times that depend on particle size, shape, and density, as well as medium viscosity and turbulence (Fuchs, 1989). It is conceivable that an exoplanet with a different atmosphere and mineralogy than Earth could host an explosive eruption that causes optical and chemical changes in the stratosphere from both sulfate aerosols and volcanic ash, given an abnormally large amount of very small ash particles. If this is the case, it might still be possible to distinguish between dust storms and ash-laden explosive eruptions. A dust storm would exhibit roughly equal aerosol absorption and dust absorption, whereas a volcanic eruption will emit ash and SO_2, the latter of which will eventually form H_2SO_4. Therefore, the volcanic eruption should show a proportionally larger aerosols signal than dust absorption signal. Differentiating between the two would likely require spectral modeling of dust storms and high-ash volcanic eruptions over a suite of aerosol and dust particle sizes, abundances and injection altitudes.

Bolides can explode in an atmosphere or impact a planetary surface, and generate stratospheric sulfate aerosol signals that can mimic those created by explosive volcanic eruptions. For example, Gorkavyi *et al.* (2013) detected and traced an aerosol excess belt in the stratosphere following the Chelyabinsk meteor (18m diameter) impact in early 2013. This event was small in terms of changes in stratospheric aerosol levels as the aerosol belt was thin, and aerosols returned to background levels within a few months. Kring *et al.* (1996) demonstrate that carbonaceous chondrites containing up to 6% sulfur by weight, with diameters greater than 300 m, will generate vapor plumes that deposit amounts of sulfur in the stratosphere analogous to the 1883 Krakatau, 1963 Agung, and 1982 El Chichón eruptions (see Table 7.1 for details of each eruption). On Earth, these impacts are estimated to occur once every 10,000 years (Sigurdsson, 1990; Kring *et al.*, 1996). To estimate the relative frequency of such impacts and how they would compare to the frequency of explosive eruptions, it would require knowing parameters such as the age of the system, system dynamics, and initial reservoir of debris. Modeling of these parameters would be necessary to determine whether a transient aerosol signal is likely caused by an explosive volcanic eruption.

Planets for which sulfur-bearing species were injected at an altitude below optically-thick aerosol layers would likely be false negatives using this method. For example, explosive volcanism on Venus or Titan, if such existed, would most likely not significantly affect the global cloud and haze layers by a sufficient amount unless the sulfate aerosols were being produced high above the existing cloud and haze layers. Venus is optically thick in transit transmission to 90 km (Ehrenreich *et al.*, 2012; García Muñoz *et al.*, 2012), so a transient aerosols signal would require an injection of sulfur more than 90 km above the surface. Titan is optically thick above 100 km in transit transmission (Robinson *et al.*, 2014), and would face a similar problem as Venus. Overall, transient sulfate aerosols will likely only be detectable for eruptions for which the plume height is greater than both the tropopause height and the height of an optically thick cloud layer. On Earth, eruptions with plume heights greater than 10-15 km should lead to transient aerosols signals. The plume height for the Pinatubo eruption was 40 km, so Pinatubo-like eruptions could be detectable for planets with tropopause heights and cloud heights less than 40 km.

Venus may also present a false positive because there are temporal variations in the aerosol extinction whose cause is currently unknown. The globally-averaged extinction in solar and stellar occultations at an altitude of 80 km varied by nearly an order of magnitude in the optical and near infrared in between 2006 and 2010 (Wilquet *et al.*, 2012). A change in extinction of an order of magnitude would imply an increase in the vertical extent of the haze by 2.3 scale heights, which for the upper Venus atmosphere would be $\sim$10 km. Additionally, the cloud base altitude can vary by several km at high latitudes (Ignatiev *et al.*, 2009). The results from Ignatiev *et al.* (2009) and Wilquet *et al.* (2012) imply that the vertical extent of the clouds and hazes in Venus' atmosphere may vary by an amount similar to the difference between the two extreme cloud cases considered here: case 1 (no clouds) and case 3 (complete cloud coverage at the tropopause or 10 km, whichever is greater). Variations in cloud and haze extents at levels $<$10 km will produce spectral variations less than the $\sim$20 km differences seen in the Earth's spectrum following the Pinatubo eruption from Figure 7.1. Future spectral modeling of Venus' transit transmission spectrum could show if the transient sulfate aerosols in Venus' atmosphere would be detectable by future ground and space-based telescopes.

The stellar UV flux incident on the planet can lead to a false negative for UV quiet stars and a potential false positive for active, flaring stars. The formation of sulfate aerosols requires OH or O_2, which are typically formed via the photolysis of H_2O and CO_2, respectively, in the absence of biology. Photochemical simulations of aerosol formation for planets orbiting UV quiet stars show that aerosol formation can be decreased by orders of magnitude (Hu *et al.*, 2013). Thus, transient sulfate aerosols may be difficult to observe for planets orbiting stars with very low levels of UV flux. In contrast, it is possible that stellar flares or other events that temporarily increase the stellar UV flux can lead to a transient increase in aerosol optical depth. This would require an abundance of either H_2S or SO_2 in the planetary atmosphere, which would react with photochemically produced OH or O_2 after the flare to form sulfate aerosols. In this scenario, the star would have to have low levels of UV flux prior to the flare. To rule out such a case, one could look for evidence of a flare, which affect wavelengths beyond the UV (Kowalski *et al.*, 2013). Furthermore, a transient sulfate aerosol signal that was triggered by a flare would still provide evidence for a flux of sulfur compounds into the atmosphere, presumably from volcanism. Photochemical modeling of sulfate aerosol formation for different stellar types and different UV fluxes, while beyond the scope of this present work, should help determine if changes in the incident UV radiation on a planet can lead to transient sulfate aerosol events that are not caused by volcanism.

Stellar activity could be another potential false positive. Starspots are cooler and fainter than the rest of the stellar disk, and can therefore affect the stellar flux. Starspots can also vary between transits, creating the inter-transit variation that would be seen during a transient sulfate aerosols event. Unocculted starspots could increase the measured transit depth, and occulted starspots could decrease it. To avoid confusion with stellar activity such as starspots, a detection of transient sulfate aerosols would likely need to occur over multiple transits. The starspot pattern on a star typically leads to changes in the light curve that are sinusoidal (Queloz *et al.*, 2009), and would most likely not lead to the characteristic rapid rise and gradual decline in effective radius that we see for transient sulfate aerosols. Furthermore, if all wavelengths are not binned over, it may be possible to detect a decrease in spectral absorption features. As shown in Figure 7.1, absorption features can become considerably weaker during a transient sulfate aerosol event. The detectability of spectral absorption features may be less sensitive to stellar activity than a broadband flux difference, which could allow for discriminating between stellar activity and a transient aerosol event.

7.5.2 Aerosol Formation in Anoxic Atmospheres

While our calculations have been done for oxygen-rich, Earth-like atmospheres, sulfate aerosols form in anoxic atmospheres as well. Hu *et al.* (2013) modeled H_2SO_4 and S_8 aerosol formation in anoxic H_2, CO_2 and N_2-dominated atmospheres over a range of H_2S and SO_2 volcanic fluxes. They found that H_2 and CO_2-dominated atmospheres preferentially form S_8 and H_2SO_4 aerosols, respectively, across all H_2S and SO_2 flux levels. N_2-dominated atmospheres form H_2SO_4 if the ratio of H_2S to SO_2 gases emitted via volcanism is lower than three times the present day ratio. For atmospheres with even trace amounts of O_2 ($pO_2 > 10^{-5}$ present atmospheric level), H_2SO_4 preferentially forms over S_8 (Pavlov and Kasting, 2002; Zahnle *et al.*, 2006). Regardless, for any atmosphere with a surface sulfur flux, sulfur aerosols (either H_2SO_4 or S_8) are expected to form photochemically and fall out over an extended period of time, though more detailed photochemical modeling is needed to quantify the detectability and duration of volcanic events under different redox regimes. Therefore, this method should be applicable to oxidized and reduced atmospheres, as well as the oxic Earth-like atmospheres we have examined here.

7.5.3 Connection to plate tectonics

Transient sulfate aerosols in the lower stratosphere are derived from explosive volcanic eruptions that advect sulfur material through the troposphere, avoiding rapid fallout. On Earth, these explosive volcanic eruptions are normally the result of plate tectonics. The explosivity of an eruption is largely dependent on the silica and volatile (primarily H_2O and CO_2) content of the magma. On Earth, silicate and volatile-rich magmas are typically generated in subduction zones under continental and island-arc settings and therefore the resulting stratovolcanism is highly explosive. In contrast, eruptions not associated with subduction zones, such as hot spot volcanism, are typically less explosive due to the low silica and volatile content of the magma. Consequently, almost all explosive volcanic eruptions large enough to markedly increase stratospheric aerosol optical depth occur in subduction zone settings (as illustrated in Figure 7.3). Therefore these transient aerosol events may also be indicative of an active tectonic regime.

There have been numerous discussions of the planetary properties, namely observables such as mass and radius, required to initiate and sustain plate tectonics (Valencia *et al.*, 2007a,b; Valencia and O'Connell, 2009; O'Neill and Lenardic, 2007). However, Lenardic and Crowley (2012) show that the ability for a planet to enter into a tectonic regime depends primarily on the geological history of the planet. Multiple modes of tectonic regimes (e.g. mobile plates, stagnant lid, and episodic tectonics) can occupy the same parameter space making it difficult to predict whether these extrasolar planets will be favorable for plate tectonics if only the bulk physical properties are known (e.g. mass, radius, composition,

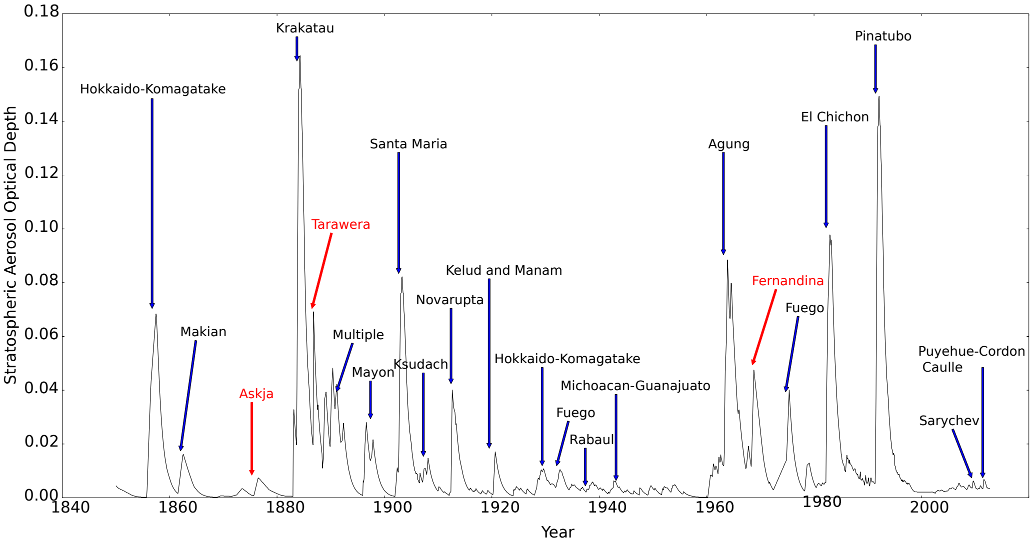

Figure 7.3: Globally averaged stratospheric aerosol optical depth for the last 160 years is plotted in black. Selected explosive eruptions (VEI of 4, 5 or 6) are denoted by arrows together with the optical depth excursions with which they coincide. Most of the named eruptions occurred at subduction zone settings; the three exceptions are highlighted in red. The 1886 Tarawera eruption was a rare basaltic Plinian eruption (Walker *et al.*, 1984), albeit associated with a back-arc basin (Lau-Harve-Taupo). The 1968 Fernandina eruption was associated with the Galapagos hotspot, although the tectonic setting is complicated by the intersection of the Nazca, Coscos and Pacific plate boundaries. The 1875 Askja eruption in Iceland also occurred at a complex tectonic setting (Geiger *et al.*, 2010). In general, we see that increased stratospheric aerosol optical depth is caused by eruptions in subduction zone settings, and even the few exceptions are not entirely disconnected from tectonic activity. Volcanic eruptions were obtained from the Smithsonian Institute Global Volcanism Program database (http://www.volcano.si.edu/) and stratospheric optical depth was obtained from NASA GISS (http://data.giss.nasa.gov/modelforce/strataer/).

etc.). Therefore, it is helpful to have an additional constraint on the probability of a planet having plate tectonics.

It is conceivable, however, that terrestrial exoplanets with differing bulk compositions or with large initial volatile reservoirs, could produce explosive volcanic eruptions that are not associated with plate tectonics. For instance there is compelling evidence for explosive volcanism on Mars despite there being no evidence for active, Earth-like plate tectonics (Mouginis-Mark *et al.*, 1982; Wilson and Head, 1994; Kerber *et al.*, 2012). On Mars, basaltic explosive eruptions are relatively common for two reasons. Firstly, Mars' lower gravity and low atmospheric pressure enhance gas exsolution and the fragmentation of magma during ascent to the surface, thereby leading to more explosive eruptions (Wilson and Head, 1994). Secondly, the interaction between subsurface water and magma increases magma volatile content and therefore eruption explosivity (Wilson and Head, 1994) . For exoplanets, surface gravity and atmospheric pressure (see Chapter 6) can potentially be constrained by remote observations. This could help to inform the likelihood that observed explosive volcanism is associated with plate tectonics. Although there is no way of remotely observing subsurface water content, it has been argued that on Mars there was a transition from explosive to effusive volcanism around 3.5 Ga attributed to declining subsurface water content (Robbins *et al.*, 2011).

Evidently, more work needs to be done on the influences of planetary composition and evolution on eruption explosivity. The future detection of transient sulfate aerosols in an exoplanet atmosphere must be carefully considered in the context of other observations before any tentative inference to plate tectonics can be made. Nevertheless, a detection of transient sulfate aerosols may be suggestive of plate tectonics for an Earth-sized exoplanet.

7.5.4 Sulfate-aerosols and oxygenic biosignatures

It has long been argued that the remote detection of atmospheric O_2 or O_3 in a terrestrial exoplanet's atmosphere would constitute a promising biosignature (Lippincott *et al.*, 1967; Walker, 1977; Angel *et al.*, 1986). In the absence of photosynthesis, Earth's steady-state O_2 column abundance would be orders of magnitude smaller than present atmospheric levels and likely not detectable remotely (Kasting, 1997). However, neither O_2 or O_3 are an unambiguous biosignature, as there are scenarios whereby abiotic oxygen could readily build up to detectable levels on Earth-like planets (Hu *et al.*, 2012; Domagal-Goldman *et al.*, 2014; Tian *et al.*, 2014; Wordsworth and Pierrehumbert, 2014). Some of these scenarios rely on low rates of volcanic outgassing. Hu *et al.* (2012) demonstrate that for very high CO_2 (1 bar) atmospheres, abiotic oxygen can only accumulate to detectable levels if there is an order of magnitude less volcanic outgassing than on the present-day Earth. Domagal-Goldman *et al.* (2014) show that for a wide variety of stellar types and CO_2-abundances, the column abundance of abiotic oxygen/ozone drops dramatically as the volcanic outgassing rate is increased. Because low levels of volcanic outgassing can aid in the formation of abiotic O_2 or O_3, the detection of transient sulfate aerosols could help resolve the ambiguity between biotic and abiotic sources of oxygen. A transient sulfate aerosol signal presumably implies a source flux of reduced volcanic gases into the observed exoplanet's atmosphere (exempting unlikely scenarios involving oxidizing volcanic gases, the outgassing of redox-neutral species such as SO_2 and H_2O will always be accompanied by outgassing of reduced species such as H_2S and H_2). For any given exoplanet, photochemical modeling of its atmosphere, stellar spectrum observations and careful consideration of stellar and orbital history will be required to evaluate how well the inference to biology is strengthened. Unfortunately it is unclear whether the oxygen source flux could be quantified by such modeling; the observation of a single episode of volcanism would not constrain the time integrated flux or redox-state of the planet's volcanic outgassing. Perhaps if the planet were observed continuously for several years and multiple volcanic episodes were detected this would put a lower bound on volcanic outgassing rates, and by extension a lower bound on the oxygen source flux.

Chapter 8

CONCLUSIONS

In the coming decades, transit transmission spectroscopy may be used to characterize Earth-like exoplanet atmospheres, providing the first opportunity to detect biosignatures and habitability markers on an exoplanet. Additionally, the increased precision required for characterizing Earth-sized planets will allow for more detailed characterization of larger planets. With the increases in observational capabilities coming in the near future, accurate models and an understanding of which physical effects will be detectable will be essential for guiding future observations and understanding the spectra and light curves that will be obtained.

In this work I have described the first model for transit transmission spectroscopy that includes the physical effects of both atmospheric refraction and forward scattering. The model uses a backwards Monte Carlo ray tracing module, coupled with an existing radiative transfer code (SMART), to generate exoplanet transmission spectra and simulate wavelength-dependent transit light curves. The model has been validated against satellite Earth-observing data from the ATMOS mission, ground-based observations of lunar eclipse spectra, and empirical and theoretical estimates of the Venus scattering footprint.

Refraction is an important effect that needs to be considered in transit transmission spectroscopy because it sets a maximum tangent pressure that can be probed, independent of atmospheric opacity (Misra *et al.*, 2014; Bétrémieux and Kaltenegger, 2014). The exact value of the maximum tangent pressure depends on the angular size of the host star (as seen by the exoplanet), the radius of the planet, and the temperature profile and composition of the planetary atmosphere. For an Earth-analog orbiting a Sun-like star, the maximum tangent pressure is 0.3 bars, which can limit the signal of spectral absorption features (compared to a cloud- and haze-free atmosphere without refraction) by an average of 60%. Consequently, the O_2 A band would require a factor of 6 greater integration time to be detectable, and detecting multiple H_2O bands in the near infrared would require a factor of 16 increase in integration time. However, for an Earth-analog orbiting an M5V star or later, the maximum tangent pressure is near 1.0 bars, meaning that almost the entire atmosphere could be probed. For these cases, the signals of spectral absorption features are reduced by only 10%, on average. This results in a minimal increase in integration time to detect spectral features, providing one reason why potentially habitable planets orbiting M dwarfs may be better targets for detecting absorption features with transit transmission than for planets orbiting Sun-like stars.

Forward scattering can increase the flux observed in transit transmission spectroscopy, relative to models that treat scattering as extinction. In general, I find that the effect of forward scattering is strong for close-in planets (R_*/a, or angular size of the star as seen by the exoplanet, $> 10^\circ$) and weaker for planets further away from their host star. In fact, for most cases, including potentially habitable planets orbiting main sequence stars, the effect of forward scattering is insignificant, and models that include only extinction from aerosols are appropriate for generating transit transmission spectra. However, forward scattering may need to be considered for future observations of hot Jupiters and terrestrial planets orbiting near the Roche limit of brown dwarfs. I examined the cases of the hot Jupiter Wasp-12 b and a Venus-analog orbiting near the Roche limit of an old brown dwarf and found that the maximum decrease in effective absorbing radius was roughly half a scale height. For Wasp-12 b, the data are best fit with small particle sizes that are not strongly forward scattering, but for particles with sizes >1 μm, the difference between the models with and without forward scattering can be as great as $\sim$50 ppm. The noise associated with current observations is too high to permit detections of signals less than 50 ppm, but for observations with future large-aperture space- and ground-based telescopes, including forward scattering may be important for accurately modeling scattering slopes and for retrieving atmospheric parameters of hot Jupiters which may have strongly forward scattering aerosols.

Refraction and forward scattering can also lead to changes in the transit light curves of exoplanets. Before ingress and after egress, light can be deflected into the beam to a distant observer by either of these processes, resulting in an increase in flux in the out-of-transit light curve. I calculated the detectability of refracted and scattered out-of-transit light. Refracted light is most detectable for clear sky (cloud- and haze-free) planets orbiting F, G, and K stars with equilibrium temperatures $<$600 K and for planets orbiting M dwarfs with equilibrium temperatures $<$400 K. This corresponds to values of R_*/a (the angular size of the star as seen by the exoplanet) $< 5^\circ$. In contrast, scattered light is most detectable for planets with highly forward scattering aerosols ($g \geq 0.8$) present in their atmospheres and with temperatures $>$1000 K for planets orbiting F, G, and K stars, and $>$700 K for planets orbiting M dwarfs ($R_*/a > 10^\circ$). This means that scattered light is most likely detectable for very close-in planets, such as hot Jupiters, and refracted light would be more detectable for planets orbiting further away from their host stars, which includes potentially habitable planets. Out-of-transit light could be detected in $<$10 hr of JWST time for Jupiter-sized planets and $<$10 hr of E-ELT time for Super-Earth/Mini-Neptune planets. Stellar activity could be a potential false positive for these signals, but looking for a repeatable signal that is seen both before and after the transit would aid in discriminating between stellar activity and refracted or scattered light. I find that a detection of refracted light would be indicative of a planet free of high-altitude clouds and hazes because out-of-transit refracted light is deflected at pressures greater than those at which high-altitude clouds and hazes typically form. Because refracted light can, in some cases, be detectable with less than a few hours of out-of-transit observing time, this method could be an economical way of determining if an exoplanet is haze-free and therefore a good target for extended follow-up observations. On the other hand, scattered light is only detectable for planets with highly forward scattering aerosols. Consequently, a detection of scattered light would strongly suggest that an exoplanet had aerosols in its atmosphere. Observations of out-of-transit scattered light could also be used to set an upper limit on the asymmetry parameter of the aerosols at a particular wavelength. This type of observation could allow constraints to be made on aerosol particle size and composition.

In addition to its utility as a diagnostic of haze-free atmospheres, refraction can be used to obtain altitude-dependent spectra of a transiting exoplanet because refraction results in different vertical regions of the atmosphere being sampled at different times during a transit (Misra *et al.*, 2014). Therefore, by differencing spectra over different time bins during the transit event, it is possible to isolate flux transmitted through specific altitudes in the atmosphere. Observations of altitude-dependent spectra in the solar system are used to retrieve vertical profiles for gas mixing ratios in exoplanet atmospheres (Smith and Hunten, 1990; Elliot and Olkin, 1996). For exoplanets, such observations could help identify gases that are concentrated in only one vertical region of the atmosphere. For example, on Earth, H_2O is primarily found in the troposphere due to the presence of a cold trap, at which H_2O condenses before reaching the stratosphere. A detection of abundant H_2O vapor in the stratosphere of an exoplanet would imply the planet did not have a cold trap, suggesting the planet is less likely to be habitable. Another application of this technique could be to confirm a biotic source of O_2. In some scenarios in which abiotic O_2 is produced, photochemically-formed O_2 is predicted to be found predominantly in the stratosphere, with low concentrations in the troposphere (Domagal-Goldman *et al.*, 2014). A detection of evenly-mixed O_2 may therefore aid in discriminating between a bioitic and an abioitic source of O_2. Obtaining altitude-dependent spectra of an Earth-like exoplanet at 10 pc would be challenging, but would provide information about the planet that cannot be obtained from a time-averaged transit transmission spectrum alone.

I also explored two signatures in transit transmission that could be novel biosignatures and habitability markers: spectral absorption features from dimer molecules and transient sulfate aerosols. Both of these signatures are very weak in the Earth's reflected spectrum, but the longer transit transmission path lengths could allow these signatures to be detectable with either JWST or E-ELT for an Earth-analog planet orbiting an M dwarf at a distance of 10 pc. Spectral absorption features from dimer molecules may provide a way to gauge atmospheric pressure on an exoplanet because absorption features from dimer molecules are more sensitive to density (and therefore pressure) than absorption from non-dimer molecules. I found that spectrally resolved observations of O_2 dimer absorption can be combined with observations of the absorption by O_2 vibration-rotation bands to provide independent constraints on the O_2 concentration and the surface or cloud-top pressure in oxygenated atmospheres for planets around M dwarfs, and with low levels of CO_2. Even if a precise estimate for the pressure is not possible, the presence of dimer absorption is indicative of pressures greater than $\simeq$0.5 bars in transmission spectroscopy, and greater than $\simeq$1 bars in reflected spectra. I showed that this method is feasible in the absence of clouds for oxygenated atmospheres, though in principle it could be applicable over a wide-range of atmospheric types because most molecules have dimer absorption features or other forms of interaction-induced absorption features (Richard *et al.*, 2012).

Transient sulfate aerosol loading in terrestrial exoplanet stratospheres may be detectable in transit transmission spectra using telescopes such as JWST and E-ELT. A detection of transient sulfate aerosols may suggest a geologically active exoplanet, since the transient signal requires explosive volcanism that can inject sulfur-bearing species into the stratosphere, where they can react to form aerosols with lifetimes of months to years. In certain circumstances, the detection of volcanism on an exoplanet would make that planet a more promising candidate for follow-up observations since geological activity is important for the origin and maintenance of life (Sleep *et al.*, 2011; Mulkidjanian *et al.*, 2012; Stüeken *et al.*, 2013). Transient sulfate aerosols in the presence of atmospheric abundant O_2 or O_3 would also constitute a more robust biosignature than O_2 or O_3 alone. In the absence of surface fluxes of reduced gases, O_2 and O_3 can potentially build up in an atmosphere even without the presence of life, making them ambiguous biosignatures. Therefore, the detection of volcanism would strongly suggest a source of oxygen-consuming reduced gases and would thus strengthen the case for biogenic oxygen.

The next steps in modeling transit transmission spectra will likely be to incorporate these features into a Monte Carlo Markov Chain retrieval model, as has been done by other groups for exoplanet studies (Madhusudhan *et al.*, 2011; Benneke and Seager, 2012; Line *et al.*, 2013). While many of these models exist today, none to date includes the effects of forward scattering and refraction. The in-transit effects of refraction and scattering could be implemented directly into the radiative transfer models that are included in these retrieval codes. The refraction component of the model runs quickly ($<$1 min), so adding it into a retrieval code would not greatly increase the computational time required. The scattering model is more computationally expensive, but considering that the range of parameter space in which scattering is expected to be important is relatively small (only for very close-in planets) it should only need to be included for a small fraction of planets. The effects of refraction and scattering on transit light curves, including obtaining altitude-dependent spectra, could be more complicated. However, transit light curve analysis is routinely being done, especially with Kepler data (Tingley, 2003; Moutou *et al.*, 2005). Similar analyses could be done to identify refracted or scattered light in a transit light curve or to obtain vertical sounding of an exoplanet atmosphere (Drake Deming, private communication). In addition to including the effects of refraction and scattering, adding dimer absorption into any retrieval model should be straightforward considering the availability of cross sectional data on dimer absorption and other forms of interaction-induced absorption (Richard *et al.*, 2012).

Following more detailed modeling efforts, the next step will be to try to detect the effects of refraction, forward scattering, and the predicted signals of dimer absorption and transient sulfate aerosols. These signals are most likely not detectable with current observational capabilities, but I find that they could be detectable in the near future with JWST and E-ELT. Before first light for these telescopes, the Transiting Exoplanet Survey Satellite (TESS) will survey the brightest and nearest stars and likely find favorable targets for characterization (Ricker *et al.*, 2014). TESS is expected to find 1000's of sub-Neptune-sized planets, including 100's of Super-Earth sized planets and up to 10's of Earth-sized planets in the habitable zones of M dwarfs (Deming *et al.*, 2009; Ricker *et al.*, 2014). For the planets that are Neptune-sized or larger, scattered and refracted light should be detectable in the out-of-transit light curves with JWST. The detection of refracted light could provide a way to quickly identify planets that are promising targets for follow-up observations, or could be used to confirm information regarding the presence of a high-altitude cloud or haze layer retrieved from the in-transit spectrum. Similarly, a detection and quantification of the amount of out-of-transit scattered light could confirm the presence of aerosols in an exoplanet atmosphere and be used as an additional constraint for retrieving particle sizes and compositions. Future work on dimer molecule absorption from H_2 or other molecules present in H_2-dominated atmospheres may allow pressure estimates to be made for these planets.

The majority of this work has focused on Earth-like planets, and it is possible that an Earth-sized planet in the habitable zone of a star could be characterized with JWST or E-ELT. As discussed in Chapters 3 and 6, JWST may be able to detect molecular absorption features, including dimer absorption features, in the spectra of Earth-analog exoplanet within 10 pc over the 5-year mission lifetime of JWST. E-ELT could be able to detect absorption features in the atmospheres of Earth-analogs in 10's of hours around F, G, and K stars (Hedelt *et al.*, 2013) and detect O_2 in $>$20 hrs (over a span of $>$2 years) for Earth-analogs orbiting M dwarfs at a distance of $\sim$10 pc (Rodler and López-Morales, 2014). I also show that E-ELT could be used to detect refracted and scattered light for Earth-sized planets in $<$10 hrs for a planet within 10 pc, and transient sulfate aerosols could also be detectable at a S/N$>$10. Therefore, if there are Earth-sized, habitable zone planets within 10 pc, the techniques described in this work could be used with E-ELT and perhaps JWST to characterize the planet.

As discussed in Chapter 7, there will likely be at least 1-2 potentially habitable planets within 10 pc, and no more than 4 if all stars host a habitable zone planet. Either JWST or E-ELT could be able to obtain a transit transmission spectrum of these worlds, providing the first opportunity to spectroscopically characterize a potentially Earth-like planet. Beyond 10 pc, the number of targets will increase, with up to 100 potentially habitable targets out 30 pc. The difficulty in characterizing planets at a distance of 30 pc is the reduced stellar flux $-$ a star at 30 pc is only 11% as bright as a star at 10 pc. JWST would almost certainly not be able to characterize Earth-like planets out to 30 pc, though E-ELT may be able to with 100-200 hours of observing time devoted to a single target, based on simple scaling relationships and previous results. Because of this, the impact of this work will be considerably broadened when the generation of telescopes after JWST and E-ELT is able to characterize planets out to 30 pc. To characterize a similar planet at a distance of 30 pc vs 10 pc, one would needed to have a collecting area nearly 10 times greater. Compared to JWST and E-ELT, this would require a space telescope with a diameter of 20 m and a ground-based telescope with a diameter over 100 m. There are currently no plans for telescopes this large, but so-called flux collector telescopes, in which image quality is sacrificed for large collecting area and thus higher S/N, could provide a solution (Snellen *et al.*, 2013). Once potentially habitable targets have been identified, the techniques described here could be used to first identify the most promising targets for extended observations, and then provide a very detailed characterization of the exoplanetary atmosphere. Identifying the best targets could be done by looking for out-of-transit refracted light and transient sulfate aerosols. A detection of refracted light would strongly suggest a cloud- and haze-free atmosphere in which molecular absorption features could be more easily detected. A transient sulfate aerosol signal would suggest a geologically active planet, which is important for the origin of life and maintaining a habitable environment. Once a promising target has been identified, the target could be observed over an extended period of time, in which molecular absorption features, including dimer features, could be identified. The inclusion of refraction (and potentially scattering) would allow for a more accurate characterization of the molecular abundances in the atmosphere. Dimer features could provide constraints on the atmospheric pressure, which is another factor that influences the habitability of an exoplanet. Lastly, the spectrum could reveal biosignatures, such as O_2, O_3, O_2 dimer absorption, or CH_4. In addition, transient sulfate aerosols could providing supporting evidence for biogenic O_2 or O_3 since volcanism typically emits oxygen-consuming reduced gases into an atmosphere. Refraction-induced vertical sounding could be used to obtain altitude-dependent spectra of the atmosphere, which, while challenging, would provide information about the exoplanet that could not be acquired in any other way. Thus, the suite of techniques I’ve developed here could provide a very detailed view of a potentially habitable exoplanet atmosphere.

BIBLIOGRAPHY

Acarreta, J. R., J. F. de Haan, and P. Stammes, 2004, Journal of Geophysical Research (Atmospheres) **109**, D05204.

Ackerman, A. S., and M. S. Marley, 2001, ApJ **556**, 872.

Agol, E., 2011, ApJ **731**, L31.

Andreeshchev, A., and J. Scalo, 2004, in *Bioastronomy 2002: Life Among the Stars*, edited by R. Norris and F. Stootman, volume 213 of *IAU Symposium*, p. 115.

Angel, J. R. P., A. Y. S. Cheng, and N. J. Woolf, 1986, Nature **322**, 341.

Anglada-Escudé, G., P. Arriagada, S. S. Vogt, E. J. Rivera, R. P. Butler, J. D. Crane, S. A. Shectman, I. B. Thompson, D. Minniti, N. Haghighipour, B. D. Carter, C. G. Tinney, *et al.*, 2012, ApJ **751**, L16.

Baines, K. H., R. W. Carlson, and L. W. Kamp, 2002, Icarus **159**, 74.

Baldridge, A., S. Hook, C. Grove, and G. Rivera, 2009, Remote Sensing of Environment **113**(4), 711 , ISSN 0034-4257, URL `http://www.sciencedirect.com/science/article/pii/S0034425708003441`.

Barnes, R., and R. Heller, 2013, Astrobiology **13**, 279.

Barton, I. J., and J. C. Scott, 1986, Appl. Opt. **25**, 3502.

Baum, W. A., and A. D. Code, 1953, AJ **58**, 108.

Bean, J. L., E. Miller-Ricci Kempton, and D. Homeier, 2010, Nature **468**, 669.

Bellucci, A., B. Sicardy, P. Drossart, P. Rannou, P. D. Nicholson, M. Hedman, K. H. Baines, and B. Burrati, 2009, Icarus **201**, 198.

Belu, A. R., F. Selsis, J.-C. Morales, I. Ribas, C. Cossou, and H. Rauer, 2011, A&A **525**, A83.

Belu, A. R., F. Selsis, S. N. Raymond, E. Pallé, R. Street, D. K. Sahu, K. von Braun, E. Bolmont, P. Figueira, G. C. Anupama, and I. Ribas, 2013, ApJ **768**, 125.

Benneke, B., and S. Seager, 2012, ApJ **753**, 100.

Benneke, B., and S. Seager, 2013, ApJ **778**, 153.

Bétrémieux, Y., and L. Kaltenegger, 2014, ApJ **791**, 7.

Bezard, B., C. de Bergh, D. Crisp, and J.-P. Maillard, 1990, Nature **345**, 508.

Bluth, G. J. S., S. D. Doiron, C. C. Schnetzler, A. J. Krueger, and L. S. Walter, 1992, Geophys. Res. Lett. **19**, 151.

Bohren, C. F., and D. R. Huffman, 1983, *Absorption and scattering of light by small particles*.

Bolmont, E., S. N. Raymond, and J. Leconte, 2011, A&A **535**, A94.

Borucki, W. J., E. Agol, F. Fressin, L. Kaltenegger, J. Rowe, H. Isaacson, D. Fischer, N. Batalha, J. J. Lissauer, G. W. Marcy, D. Fabrycky, J.-M. Désert, *et al.*, 2013, Science **340**, 587.

Borucki, W. J., D. G. Koch, G. Basri, N. Batalha, T. M. Brown, S. T. Bryson, D. Caldwell, J. Christensen-Dalsgaard, W. D. Cochran, E. DeVore, E. W. Dunham, T. N. Gautier, III, *et al.*, 2011, ApJ **736**, 19.

Bourassa, A. E., D. A. Degenstein, B. J. Elash, and E. J. Llewellyn, 2010, Journal of Geophysical Research (Atmospheres) **115**, D00L03.

Brown, M. E., J. E. Roberts, and E. L. Schaller, 2010, Icarus **205**, 571.

Brown, T. M., 2001, ApJ **553**, 1006.

Canfield, D. E., M. T. Rosing, and C. Bjerrum, 2006, Philosophical Transactions of the Royal Society B: Biological Sciences **361**(1474), 1819, URL `http://rstb.royalsocietypublishing.org/content/361/1474/1819.abstract`.

Cantrell, J. R., T. J. Henry, and R. J. White, 2013, AJ **146**, 99.

Carey, S., J. Ingalls, J. Hora, J. Surace, W. Glaccum, P. Lowrance, J. Krick, D. Cole, S. Laine, C. Engelke, S. Price, R. Bohlin, *et al.*, 2012, in *Society of Photo-Optical Instrumentation Engineers (SPIE) Conference Series*, volume 8442 of *Society of Photo-Optical Instrumentation Engineers (SPIE) Conference Series*.

Catling, D., V. Meadows, T. D. Robinson, and D. Crisp, 2012, in *AbSciCon 2012*, Astrobiology Science Conference Abstracts.

Catling, D. C., M. W. Claire, K. J. Zahnle, R. C. Quinn, B. C. Clark, M. H. Hecht, and S. Kounaves, 2010, Journal of Geophysical Research (Planets) **115**, E00E11.

Chamberlain, S., J. Bailey, D. Crisp, and V. Meadows, 2013, Icarus **222**, 364.

Chamberlain, S. A., J. A. Bailey, and D. Crisp, 2006, PASA **23**, 119.

Charbonneau, D., T. M. Brown, R. W. Noyes, and R. L. Gilliland, 2002, ApJ **568**, 377.

Charlson, R. J., S. E. Schwartz, J. M. Hales, R. D. Cess, J. A. Coakley, Jr., J. E. Hansen, and D. J. Hofmann, 1992, Science **255**, 423.

Clark, R. N., G. A. Swayze, R. Wise, E. Livo, T. Hoefen, R. Kokaly, and S. J. Sutley, 2007, Digital Data Series, U.S. Geological Survey **231**.

Clough, S. A., M. J. Iacono, and J.-L. Moncet, 1992, J. Geophys. Res. **97**, 15761.

Cockell, C. S., A. Léger, M. Fridlund, T. M. Herbst, L. Kaltenegger, O. Absil, C. Beichman, W. Benz, M. Blanc, A. Brack, A. Chelli, L. Colangeli, *et al.*, 2009, Astrobiology **9**, 1.

Cowan, N. B., P. Machalek, B. Croll, L. M. Shekhtman, A. Burrows, D. Deming, T. Greene, and J. L. Hora, 2012, ApJ **747**, 82.

Crisp, D., 1986, Icarus **67**, 484.

Crisp, D., 1997, Geophys. Res. Lett. **24**, 571.

Crisp, D., B. M. Fisher, C. O'Dell, C. Frankenberg, R. Basilio, H. Bösch, L. R. Brown, R. Castano, B. Connor, N. M. Deutscher, A. Eldering, D. Griffith, *et al.*, 2012, Atmospheric Measurement Techniques **5**, 687.

Croll, B., S. Rappaport, J. DeVore, R. L. Gilliland, J. R. Crepp, A. W. Howard, K. M. Star, E. Chiang, A. M. Levine, J. M. Jenkins, L. Albert, A. S. Bonomo, *et al.*, 2014, ApJ **786**, 100.

Crow, C. A., L. A. McFadden, T. Robinson, V. S. Meadows, T. A. Livengood, T. Hewagama, R. K. Barry, L. D. Deming, C. M. Lisse, and D. Wellnitz, 2011, ApJ **729**, 130.

de Kok, R. J., and D. M. Stam, 2012, Icarus **221**, 517.

Deming, D., S. Seager, J. Winn, E. Miller-Ricci, M. Clampin, D. Lindler, T. Greene, D. Charbonneau, G. Laughlin, G. Ricker, D. Latham, and K. Ennico, 2009, PASP **121**, 952.

Deming, D., A. Wilkins, P. McCullough, A. Burrows, J. J. Fortney, E. Agol, I. Dobbs-Dixon, N. Madhusudhan, N. Crouzet, J.-M. Desert, R. L. Gilliland, K. Haynes, *et al.*, 2013, ApJ **774**, 95.

Des Marais, D. J., M. O. Harwit, K. W. Jucks, J. F. Kasting, D. N. C. Lin, J. I. Lunine, J. Schneider, S. Seager, W. A. Traub, and N. J. Woolf, 2002, Astrobiology **2**, 153.

Des Marais, D. J., J. A. Nuth, III., L. J. Allamandola, A. P. Boss, J. D. Farmer, T. M. Hoehler, B. M. Jakosky, V. S. Meadows, A. Pohorille, B. Runnegar, and A. M. Spormann, 2008, Astrobiology **8**, 715.

Devine, J. D., H. Sigurdsson, A. N. Davis, and S. Self, 1984, J. Geophys. Res. **89**, 6309.

Domagal-Goldman, S. D., V. S. Meadows, M. W. Claire, and J. F. Kasting, 2011, Astrobiology **11**, 419.

Domagal-Goldman, S. D., A. Segura, M. W. Claire, T. D. Robinson, and V. S. Meadows, 2014, ArXiv e-prints `1407.2622`.

Ehrenreich, D., A. Vidal-Madjar, T. Widemann, G. Gronoff, P. Tanga, M. Barthélemy, J. Lilensten, A. Lecavelier Des Etangs, and L. Arnold, 2012, A&A **537**, L2.

Elliot, J. L., and C. B. Olkin, 1996, Annual Review of Earth and Planetary Sciences **24**, 89.

English, J. M., O. B. Toon, and M. J. Mills, 2013, Journal of Geophysical Research (Atmospheres) **118**, 1880.

Evans, N., V. S. Meadows, and S. D. Domagal-Goldman, 2011, in *American Astronomical Society Meeting Abstracts #217*, volume 43 of *Bulletin of the American Astronomical Society*, p. 343.09.

Feulner, G., 2012, Reviews of Geophysics **50**, RG2006.

Forget, F., A. Spiga, B. Dolla, S. Vinatier, R. Melchiorri, P. Drossart, A. Gendrin, J.-P. Bibring, Y. Langevin, and B. Gondet, 2007, Journal of Geophysical Research (Planets) **112**, E08S15.

Fortney, J. J., 2005, MNRAS **364**, 649.

Fraine, J., D. Deming, B. Benneke, H. Knutson, A. Jordán, N. Espinoza, N. Madhusudhan, A. Wilkins, and K. Todorov, 2014, Nature **513**, 526.

Fridlund, C. V. M., 2000, in *Darwin and Astronomy : the Infrared Space Interferometer*, edited by B. Schürmann, volume 451 of *ESA Special Publication*, p. 11.

Fuchs, N. A., 1989, *The Mechanics of Aerosols* (Dover).

García Muñoz, A., and F. P. Mills, 2012, A&A **547**, A22.

García Muñoz, A., M. R. Zapatero Osorio, R. Barrena, P. Montañés-Rodríguez, E. L. Martín, and E. Pallé, 2012, ApJ **755**, 103.

Gardner, J. P., J. C. Mather, M. Clampin, R. Doyon, M. A. Greenhouse, H. B. Hammel, J. B. Hutchings, P. Jakobsen, S. J. Lilly, K. S. Long, J. I. Lunine, M. J. McCaughrean, *et al.*, 2006, Space Sci. Rev. **123**, 485.

Geiger, S., M. Lupi, R. Carey, T. Thordarson, and B. F. Houghton, 2010, AGU Fall Meeting Abstracts , A5.

Gilmozzi, R., and J. Spyromilio, 2007, The Messenger **127**, 11.

Gorkavyi, N. N., T. A. Taidakova, E. A. Provornikova, I. N. Gorkavyi, and M. M. Akhmetvaleev, 2013, Solar System Research **47**, 275.

Gray, L. D., 1966, Icarus **5**, 390.

Greenblatt, G. D., J. J. Orlando, J. B. Burkholder, and A. R. Ravishankara, 1990, J. Geophys. Res. **95**, 18577.

Grillmair, C. J., A. Burrows, D. Charbonneau, L. Armus, J. Stauffer, V. Meadows, J. van Cleve, K. von Braun, and D. Levine, 2008, Nature **456**, 767.

Grishko, V. I., and W. W. Duley, 2002, ApJ **568**, L131.

Gronoff, G., J. Lilensten, C. Simon, M. Barthélemy, F. Leblanc, and O. Dutuit, 2008, A&A **482**, 1015.

Gunson, M. R., C. B. Farmer, R. H. Norton, R. Zander, and C. P. Rinsland, 1990, J. Geophys. Res. **95**, 13867.

Hansen, J. E., and L. D. Travis, 1974, Space Sci. Rev. **16**, 527.

Hashimoto, G. L., and T. Imamura, 2001, Icarus **154**, 239.

Hauschildt, P. H., F. Allard, and E. Baron, 1999, ApJ **512**, 377.

Haywood, J. M., A. Jones, L. Clarisse, A. Bourassa, J. Barnes, P. Telford, N. Bellouin, O. Boucher, P. Agnew, C. Clerbaux, P. Coheur, D. Degenstein, *et al.*, 2010, Journal of Geophysical Research (Atmospheres) **115**, D21212.

Hedelt, P., P. von Paris, M. Godolt, S. Gebauer, J. L. Grenfell, H. Rauer, F. Schreier, F. Selsis, and T. Trautmann, 2013, A&A **553**, A9.

Henry, T. J., W. C. Jao, J. P. Subasavage, T. D. Beaulieu, P. A. Ianna, E. Costa, and R. A. Méndez, 2006, AJ **132**, 2360.

Henyey, L. G., and J. L. Greenstein, 1941, ApJ **93**, 70.

Holm, N. G., and J. L. Charlou, 2001, Earth and Planetary Science Letters **191**, 1.

Howe, A. R., and A. S. Burrows, 2012, ApJ **756**, 176.

Hu, R., S. Seager, and W. Bains, 2012, ApJ **761**, 166.

Hu, R., S. Seager, and W. Bains, 2013, ApJ **769**, 6.

Hubbard, W. B., J. J. Fortney, J. I. Lunine, A. Burrows, D. Sudarsky, and P. Pinto, 2001, ApJ **560**, 413.

Hui, L., and S. Seager, 2002, ApJ **572**, 540.

Ignatiev, N. I., D. V. Titov, G. Piccioni, P. Drossart, W. J. Markiewicz, V. Cottini, T. Roatsch, M. Almeida, and N. Manoel, 2009, Journal of Geophysical Research (Planets) **114**, E00B43.

Irion, F. W., M. R. Gunson, G. C. Toon, A. Y. Chang, A. Eldering, E. Mahieu, G. L. Manney, H. A. Michelsen, E. J. Moyer, M. J. Newchurch, G. B. Osterman, C. P. Rinsland, *et al.*, 2002, Appl. Opt. **41**, 6968.

Jackson, B., R. Barnes, and R. Greenberg, 2008, MNRAS **391**, 237.

Kaltenegger, L., W. G. Henning, and D. D. Sasselov, 2010, AJ **140**, 1370.

Kaltenegger, L., and W. A. Traub, 2009, ApJ **698**, 519.

Kaplan, L. D., G. Münch, and H. Spinrad, 1964, ApJ **139**, 1.

Karagulian, F., L. Clarisse, C. Clerbaux, A. J. Prata, D. Hurtmans, and P. F. Coheur, 2010, Journal of Geophysical Research (Atmospheres) **115**, D00L02.

Kasting, J. F., 1988, Icarus **74**, 472.

Kasting, J. F., 1997, Origins of Life and Evolution of the Biosphere **27**, 291.

Kasting, J. F., and W. A. Traub, 2010, URL `http://sites.nationalacademies.org/BPA/BPA_050603#planetarysystems`.

Kasting, J. F., D. P. Whitmire, and R. T. Reynolds, 1993, Icarus **101**, 108.

Kawahara, H., T. Matsuo, M. Takami, Y. Fujii, T. Kotani, N. Murakami, M. Tamura, and O. Guyon, 2012, ApJ **758**, 13.

Keen, R. A., 1983, Science **222**, 1011.

Kerber, L., J. W. Head, J. B. Madeleine, F. Forget, and L. Wilson, 2012, Icarus **219**, 358.

Kieffer, H. H., T. Z. Martin, A. R. Peterfreund, B. M. Jakosky, E. D. Miner, and F. D. Palluconi, 1977, J. Geophys. Res. **82**, 4249.

Knutson, H. A., B. Benneke, D. Deming, and D. Homeier, 2014a, Nature **505**, 66.

Knutson, H. A., D. Charbonneau, L. E. Allen, A. Burrows, and S. T. Megeath, 2008, ApJ **673**, 526.

Knutson, H. A., D. Dragomir, L. Kreidberg, E. M.-R. Kempton, P. R. McCullough, J. J. Fortney, J. L. Bean, M. Gillon, D. Homeier, and A. W. Howard, 2014b, ArXiv e-prints `1403.4602`.

Köhler, J., M. Melf, W. Posselt, W. Holota, and M. te Plate, 2005, in *Optical Design and Engineering II*, edited by L. Mazuray and R. Wartmann, volume 5962 of *Society of Photo-Optical Instrumentation Engineers (SPIE) Conference Series*, pp. 563–574.

Koike, C., C. Kaito, T. Yamamoto, H. Shibai, S. Kimura, and H. Suto, 1995, Icarus **114**, 203.

Kopparapu, R. K., R. Ramirez, J. F. Kasting, V. Eymet, T. D. Robinson, S. Mahadevan, R. C. Terrien, S. Domagal-Goldman, V. Meadows, and R. Deshpande, 2013, ApJ **765**, 131.

Kowalski, A. F., S. L. Hawley, J. P. Wisniewski, R. A. Osten, E. J. Hilton, J. A. Holtzman, S. J. Schmidt, and J. R. A. Davenport, 2013, ApJS **207**, 15.

Kreidberg, L., J. L. Bean, J.-M. Désert, B. Benneke, D. Deming, K. B. Stevenson, S. Seager, Z. Berta-Thompson, A. Seifahrt, and D. Homeier, 2014, Nature **505**, 69.

Kring, D. A., H. J. Melosh, and D. M. Hunten, 1996, Earth and Planetary Science Letters **140**, 201.

Kump, L. R., 2008, Nature **451**, 277.

Kurucz, R. L., 1979, ApJS **40**, 1.

Lacis, A., J. Hansen, and M. Sato, 1992, Geophys. Res. Lett. **19**, 1607.

Lafferty, W. J., A. M. Solodov, A. Weber, W. B. Olson, and J.-M. Hartmann, 1996, Appl. Opt. **35**, 5911.

Lafreniere, D., R. Doyon, FGS/NIRISS, NIRCam, MIRI, and NIRSpec Science Teams, 2013, in *American Astronomical Society Meeting Abstracts #221*, volume 221 of *American Astronomical Society Meeting Abstracts*, p. 135.06.

Lawson, P. R., O. Absil, R. L. Akeson, J. Bally, R. K. Barry, C. A. Beichman, A. J. Booth, P. Bordé, J. Breckinridge, D. Cole, V. Coudé du Foresto, W. C. Danchi, *et al.*, 2009, in *astro2010: The Astronomy and Astrophysics Decadal Survey*, volume 2010 of *ArXiv Astrophysics e-prints*, p. 53.

Lenardic, A., and J. W. Crowley, 2012, ApJ **755**, 132.

Levine, M., D. Lisman, S. Shaklan, J. Kasting, W. Traub, J. Alexander, R. Angel, C. Blaurock, M. Brown, R. Brown, C. Burrows, M. Clampin, *et al.*, 2009, ArXiv e-prints `0911.3200`.

Line, M. R., H. Knutson, A. S. Wolf, and Y. L. Yung, 2014, ApJ **783**, 70.

Line, M. R., A. S. Wolf, X. Zhang, H. Knutson, J. A. Kammer, E. Ellison, P. Deroo, D. Crisp, and Y. L. Yung, 2013, ApJ **775**, 137.

Lippincott, E. R., R. V. Eck, M. O. Dayhoff, and C. Sagan, 1967, ApJ **147**, 753.

Llewellyn, E., N. D. Lloyd, D. A. Degenstein, R. L. Gattinger, S. V. Petelina, A. E. Bourassa, J. T. Wiensz, E. V. Ivanov, I. C. McDade, B. H. Solheim, J. C. McConnell, C. S. Haley, *et al.*, 2004, Canadian Journal of Physics **82**, 411.

Loeb, A., and D. Maoz, 2013, MNRAS **432**, L11.

Lovelock, J. E., 1965, Nature **207**, 568.

Lunine, J. I., 1993, ARA&A **31**, 217.

Madhusudhan, N., J. Harrington, K. B. Stevenson, S. Nymeyer, C. J. Campo, P. J. Wheatley, D. Deming, J. Blecic, R. A. Hardy, N. B. Lust, D. R. Anderson, A. Collier-Cameron, *et al.*, 2011, Nature **469**, 64.

Marley, M. S., A. S. Ackerman, J. N. Cuzzi, and D. Kitzmann, 2013, *Clouds and Hazes in Exoplanet Atmospheres*, pp. 367–391.

Maté, B., C. Lugez, G. T. Fraser, and W. J. Lafferty, 1999, J. Geophys. Res. **104**, 30585.

Mayor, M., and D. Queloz, 1995, Nature **378**, 355.

McClatchey, R. A., R. W. Fenn, J. E. A. Selby, and J. S. Volz, F. E. andGaring, 1972, *Optical Properties of the Atmosphere (Third Edition).*, Technical Report, Air Force Cambridge Research Labs.

McCormick, M. P., 1987, Advances in Space Research **7**, 219.

McCormick, M. P., P. H. Wang, and M. C. Pitts, 1996, Advances in Space Research **18**, 155.

McKay, C. P., Porco Carolyn C., T. Altheide, W. L. Davis, and T. A. Kral, 2008, Astrobiology **8**, 909.

McQuillan, A., S. Aigrain, and T. Mazeh, 2013, MNRAS **432**, 1203.

Meadows, V. S., and D. Crisp, 1996, J. Geophys. Res. **101**, 4595.

Minnis, P., E. F. Harrison, L. L. Stowe, G. G. Gibson, F. M. Denn, D. R. Doelling, and W. L. Smith, Jr., 1993, Science **259**, 1411.

Misra, A., V. Meadows, and D. Crisp, 2014, ApJ **792**, 61.

Mitchell, R. M., and D. M. O'Brien, 1987, Journal of Atmospheric Sciences **44**, 1981.

Montmessin, F., J.-L. Bertaux, E. Quémerais, O. Korablev, P. Rannou, F. Forget, S. Perrier, D. Fussen, S. Lebonnois, A. Rébérac, and E. Dimarellis, 2006, Icarus **183**, 403.

Moroz, V. I., 2002, Planet. Space Sci. **50**, 287.

Mouginis-Mark, P. J., J. W. Head, III, and L. Wilson, 1982, J. Geophys. Res. **87**, 9890.

Moutou, C., F. Pont, P. Barge, S. Aigrain, M. Auvergne, D. Blouin, R. Cautain, A. R. Erikson, V. Guis, P. Guterman, M. Irwin, A. F. Lanza, *et al.*, 2005, A&A **437**, 355.

Mulkidjanian, A. Y., A. Y. Bychkov, D. V. Dibrova, M. Y. Galperin, and E. V. Koonin, 2012, Proceedings of the National Academy of Science **109**.

Nielsen, M. B., L. Gizon, H. Schunker, and C. Karoff, 2013, A&A **557**, L10.

Nisbet, E. G., and N. H. Sleep, 2001, Nature **409**, 1083.

O'Neill, C., and A. Lenardic, 2007, Geophys. Res. Lett. **34**, L19204.

Oswalt, J. S., W. Nicholes, and O. J. F., 1996, *Meteorological observations of the 1991 Mount Pinatubo eruption* (University of Washington Press, Seattle and Philippine Institution of Volcanology and Seismology, Quezon City), pp. 625–636.

Pallé, E., M. R. Zapatero Osorio, R. Barrena, P. Montañés-Rodríguez, and E. L. Martín, 2009, Nature **459**, 814.

Palmer, K. F., and D. Williams, 1975, Appl. Opt. **14**, 208.

Pasachoff, J. M., G. Schneider, and T. Widemann, 2011, AJ **141**, 112.

Pavlov, A. A., and J. F. Kasting, 2002, Astrobiology **2**, 27.

Pierrehumbert, R. T., 2010, *Principles of Planetary Climate*.

Pollack, J. B., D. S. Colburn, F. M. Flasar, R. Kahn, C. E. Carlston, and D. G. Pidek, 1979, J. Geophys. Res. **84**, 2929.

Pollack, J. B., J. F. Kasting, S. M. Richardson, and K. Poliakoff, 1987a, Icarus **71**, 203.

Pollack, J. B., K. Rages, S. K. Pope, M. G. Tomasko, and P. N. Romani, 1987b, J. Geophys. Res. **92**, 15037.

Pont, F., H. Knutson, R. L. Gilliland, C. Moutou, and D. Charbonneau, 2008, MNRAS **385**, 109.

Postman, M., T. Brown, A. Koekemoer, M. Giavalisco, S. Unwin, W. Traub, D. Calzetti, W. Oegerle, M. Shull, S. Kilston, and H. P. Stahl, 2008, in *Society of Photo-Optical Instrumentation Engineers (SPIE) Conference Series*, volume 7010 of *Society of Photo-Optical Instrumentation Engineers (SPIE) Conference Series*, p. 21.

Postman, M., T. Brown, K. Sembach, M. Giavalisco, W. Traub, K. Stapelfeldt, D. Calzetti, W. Oegerle, R. Michael Rich, H. Phillip Stahl, J. Tumlinson, M. Mountain, *et al.*, 2012, Optical Engineering **51**(1), 011007.

Prata, A. J., and J. Kerkmann, 2007, Geophys. Res. Lett. **34**, L05813.

Queloz, D., F. Bouchy, C. Moutou, A. Hatzes, G. Hébrard, R. Alonso, M. Auvergne, A. Baglin, M. Barbieri, P. Barge, W. Benz, P. Bordé, *et al.*, 2009, A&A **506**, 303.

Quintana, E. V., T. Barclay, S. N. Raymond, J. F. Rowe, E. Bolmont, D. A. Caldwell, S. B. Howell, S. R. Kane, D. Huber, J. R. Crepp, J. J. Lissauer, D. R. Ciardi, *et al.*, 2014, Science **344**, 277.

Rappaport, S., A. Levine, E. Chiang, I. El Mellah, J. Jenkins, B. Kalomeni, E. S. Kite, M. Kotson, L. Nelson, L. Rousseau-Nepton, and K. Tran, 2012, ApJ **752**, 1.

Rauer, H., S. Gebauer, P. V. Paris, J. Cabrera, M. Godolt, J. L. Grenfell, A. Belu, F. Selsis, P. Hedelt, and F. Schreier, 2011, A&A **529**, A8.

Reid, I. N., and S. L. Hawley, 2005, *New light on dark stars : red dwarfs, low-mass stars, brown dwarfs*.

Richard, C., I. E. Gordon, L. S. Rothman, M. Abel, L. Frommhold, M. Gustafsson, J.-M. Hartmann, C. Hermans, W. J. Lafferty, G. S. Orton, K. M. Smith, and H. Tran, 2012, J. Quant. Spec. Radiat. Transf. **113**, 1276.

Ricker, G. R., J. N. Winn, R. Vanderspek, D. W. Latham, G. Á. Bakos, J. L. Bean, Z. K. Berta-Thompson, T. M. Brown, L. Buchhave, N. R. Butler, R. P. Butler, W. J. Chaplin, *et al.*, 2014, in *Society of Photo-Optical Instrumentation Engineers (SPIE) Conference Series*, volume 9143 of *Society of Photo-Optical Instrumentation Engineers (SPIE) Conference Series*, p. 20, `1406.0151`.

Robbins, S. J., G. D. Achille, and B. M. Hynek, 2011, Icarus **211**, 1179.

Robinson, T. D., and D. C. Catling, 2014, Nature Geoscience **7**, 12.

Robinson, T. D., L. Maltagliati, M. S. Marley, and J. J. Fortney, 2014, Proceedings of the National Academy of Science **111**, 9042.

Robinson, T. D., V. S. Meadows, D. Crisp, D. Deming, M. F. A'Hearn, D. Charbonneau, T. A. Livengood, S. Seager, R. K. Barry, T. Hearty, T. Hewagama, C. M. Lisse, *et al.*, 2011, Astrobiology **11**, 393.

Rodgers, C. D., 1976, Reviews of Geophysics and Space Physics **14**, 609.

Rodler, F., and M. López-Morales, 2014, ApJ **781**, 54.

Rogers, L. A., 2014, ArXiv e-prints `1407.4457`.

Rothman, L. S., I. E. Gordon, Y. Babikov, A. Barbe, D. Chris Benner, P. F. Bernath, M. Birk, L. Bizzocchi, V. Boudon, L. R. Brown, A. Campargue, K. Chance, *et al.*, 2013, J. Quant. Spec. Radiat. Transf. **130**, 4.

Rothman, L. S., I. E. Gordon, A. Barbe, D. C. Benner, P. F. Bernath, M. Birk, V. Boudon, L. R. Brown, A. Campargue, J.-P. Champion, K. Chance, L. H. Coudert, *et al.*, 2009, J. Quant. Spec. Radiat. Transf. **110**, 533.

Sagan, C., and G. Mullen, 1972, Science **177**, 52.

Sato, M., J. E. Hansen, M. P. McCormick, and J. B. Pollack, 1993, J. Geophys. Res. **98**, 22987.

Schneider, D. J., K. L. Wallace, and L. G. Mastin, 2012, AGU Fall Meeting Abstracts , H4.

Seager, S., and D. D. Sasselov, 2000, ApJ **537**, 916.

Segura, A., J. F. Kasting, V. Meadows, M. Cohen, J. Scalo, D. Crisp, R. A. H. Butler, and G. Tinetti, 2005, Astrobiology **5**, 706.

Segura, A., V. S. Meadows, J. F. Kasting, D. Crisp, and M. Cohen, 2007, A&A **472**, 665.

Self, S., and A. J. King, 1996, Bulletin of Volcanology **58**, 263.

Self, S., and M. R. Rampino, 1982, Journal of Volcanology and Geothermal Research **13**, 379.

Selsis, F., J. F. Kasting, B. Levrard, J. Paillet, I. Ribas, and X. Delfosse, 2007, A&A **476**, 1373.

Sidis, O., and R. Sari, 2010, ApJ **720**, 904.

Sigurdsson, H., 1990, Global and Planetary Change **3**, 277.

Sing, D. K., A. Lecavelier des Etangs, J. J. Fortney, A. S. Burrows, F. Pont, H. R. Wakeford, G. E. Ballester, N. Nikolov, G. W. Henry, S. Aigrain, D. Deming, T. M. Evans, *et al.*, 2013, MNRAS **436**, 2956.

Sing, D. K., F. Pont, S. Aigrain, D. Charbonneau, J.-M. Désert, N. Gibson, R. Gilliland, W. Hayek, G. Henry, H. Knutson, A. Lecavelier Des Etangs, T. Mazeh, *et al.*, 2011, MNRAS **416**, 1443.

Sioris, C. E., C. D. Boone, P. F. Bernath, J. Zou, C. T. McElroy, and C. A. McLinden, 2010, Journal of Geophysical Research (Atmospheres) **115**, D00L14.

Slanina, Z., F. Uhlk, W. B. D. Almeida, and A. Hinchliffe, 1994, Thermochimica Acta **231**(0), 55 , ISSN 0040-6031, URL `http://www.sciencedirect.com/science/article/pii/0040603194800073`.

Sleep, N. H., D. K. Bird, and E. C. Pope, 2011, Philosophical Transactions of the Royal Society B: Biological Sciences **366**(1580), 2857, URL `http://rstb.royalsocietypublishing.org/content/366/1580/2857.abstract`.

Smith, B. A., L. Soderblom, R. F. Beebe, J. M. Boyce, G. Briggs, A. Bunker, S. A. Collins, C. Hansen, T. V. Johnson, J. L. Mitchell, R. J. Terrile, M. H. Carr, *et al.*, 1981, Science **212**, 163.

Smith, G. R., and D. M. Hunten, 1990, Reviews of Geophysics **28**, 117.

Smrekar, S. E., E. R. Stofan, N. Mueller, A. Treiman, L. Elkins-Tanton, J. Helbert, G. Piccioni, and P. Drossart, 2010, Science **328**, 605.

Snellen, I. A. G., R. J. de Kok, R. le Poole, M. Brogi, and J. Birkby, 2013, ApJ **764**, 182.

Spergel, D., N. Gehrels, J. Breckinridge, M. Donahue, A. Dressler, B. S. Gaudi, T. Greene, O. Guyon, C. Hirata, J. Kalirai, N. J. Kasdin, W. Moos, *et al.*, 2013, ArXiv e-prints `1305.5422`.

Spiga, A., F. Forget, B. Dolla, S. Vinatier, R. Melchiorri, P. Drossart, A. Gendrin, J.-P. Bibring, Y. Langevin, and B. Gondet, 2007, Journal of Geophysical Research (Planets) **112**, E08S16.

Stevenson, K. B., J. L. Bean, A. Seifahrt, J.-M. Désert, N. Madhusudhan, M. Bergmann, L. Kreidberg, and D. Homeier, 2014, AJ **147**, 161.

Stüeken, E. E., R. E. Anderson, J. S. Bowman, W. J. Brazelton, J. Colangelo-Lillis, A. D. Goldman, S. M. Som, and J. A. Baross, 2013, Geobiology **11**(2), 101, ISSN 1472-4669, URL `http://dx.doi.org/10.1111/gbi.12025`.

Thomas, G. E., B. M. Jakosky, R. A. West, and R. W. Sanders, 1983, Geophys. Res. Lett. **10**, 997.

Tian, F., K. France, J. L. Linsky, P. J. D. Mauas, and M. C. Vieytes, 2014, Earth and Planetary Science Letters **385**, 22.

Tingley, B., 2003, A&A **408**, L5.

Tyler, G. L., V. R. Eshleman, J. D. Anderson, G. S. Levy, G. F. Lindal, G. E. Wood, and T. A. Croft, 1982, Science **215**, 553.

Uhlk, F., Z. Slanina, and A. Hinchliffe, 1993, Thermochimica Acta **228**(0), 9 , ISSN 0040-6031, URL `http://www.sciencedirect.com/science/article/pii/004060319380268F`.

Vahidinia, S., J. N. Cuzzi, M. Marley, and J. Fortney, 2014, ApJ **789**, L11.

Valencia, D., and R. J. O’Connell, 2009, Earth and Planetary Science Letters **286**, 492.

Valencia, D., R. J. O’Connell, and D. D. Sasselov, 2007a, ApJ **670**, L45.

Valencia, D., D. D. Sasselov, and R. J. O’Connell, 2007b, ApJ **665**, 1413.

van der Werf, S. Y., 2008, Appl. Opt. **47**, 153.

Varekamp, J. C., J. F. Luhr, and K. L. Prestegaard, 1984, Journal of Volcanology and Geothermal Research **23**, 39.

Vidal-Madjar, A., A. Lecavelier des Etangs, J.-M. Désert, G. E. Ballester, R. Ferlet, G. Hébrard, and M. Mayor, 2003, Nature **422**, 143.

Wakeford, H. R., D. K. Sing, D. Deming, N. P. Gibson, J. J. Fortney, A. S. Burrows, G. Ballester, N. Nikolov, S. Aigrain, G. Henry, H. Knutson, A. Lecavelier des Etangs, *et al.*, 2013, MNRAS **435**, 3481.

Walker, G. P. L., S. Self, and L. Wilson, 1984, Journal of Volcanology and Geothermal Research **21**, 61.

Walker, J. C. G., 1977, *Evolution of the atmosphere*.

Walker, J. C. G., P. B. Hays, and J. F. Kasting, 1981, J. Geophys. Res. **86**, 9776.

Weiss, L. M., and G. W. Marcy, 2014, ApJ **783**, L6.

West, R. A., D. F. Strobel, and M. G. Tomasko, 1986, Icarus **65**, 161.

Wilquet, V., R. Drummond, A. Mahieux, S. Robert, A. C. Vandaele, and J.-L. Bertaux, 2012, Icarus **217**, 875.

Wilson, L., and J. W. Head, III, 1994, Reviews of Geophysics **32**, 221.

Winker, D. M., J. L. Tackett, B. J. Getzewich, Z. Liu, M. A. Vaughan, and R. R. Rogers, 2013, Atmospheric Chemistry & Physics **13**, 3345.

Winn, J. N., 2011, *Exoplanet Transits and Occultations*, pp. 55–77.

Wolszczan, A., and D. A. Frail, 1992, Nature **355**, 145.

Wordsworth, R., and R. Pierrehumbert, 2014, ApJ **785**, L20.

Wordsworth, R. D., F. Forget, F. Selsis, J.-B. Madeleine, E. Millour, and V. Eymet, 2010, A&A **522**, A22.

Wright, J. T., O. Fakhouri, G. W. Marcy, E. Han, Y. Feng, J. A. Johnson, A. W. Howard, D. A. Fischer, J. A. Valenti, J. Anderson, and N. Piskunov, 2011, PASP **123**, 412.

Yang, J., G. Boué, D. C. Fabrycky, and D. S. Abbot, 2014, ApJ **787**, L2.

Young, A. T., 1973, Icarus **18**, 564.

Zahnle, K., M. Claire, and D. Catling, 2006, Geobiology **4**(4), 271, ISSN 1472-4669, URL `http://dx.doi.org/10.1111/j.1472-4669.2006.00085.x`.

Zerkle, A. L., M. W. Claire, S. D. Domagal-Goldman, J. Farquhar, and S. W. Poulton, 2012, Nature Geoscience **5**, 359.

Zombeck, M. V., 1990, *Handbook of space astronomy and astrophysics*.

Appendix A

REFRACTION DERIVATION

Refraction is a consequence of Fermat's principle, which states that the path taken between two points by a ray of light is the path that can be traversed in the minimum time. Application of Fermat's principle results in Snell's Law, from which the physics of atmospheric refraction can be derived. Snell's Law states that as a photon passes from a material with an index of refraction n_a to another material with index of refraction n_b, the two respective angles of incidence θ_a and θ_b are related by the following equation:

$$n_a \sin\theta_a = n_b \sin\theta_b \tag{A.1}$$

Figure A.1 shows an example of how Fermat's principle leads to Snell's Law. Let a photon travel from point A to B via point P, which is a point on the boundary between two materials with different indices of refraction. Let point A be defined as (a_1, a_2) and point B as (b_1, b_2). Let P be at $(x, 0)$. Because P is somewhere on the boundary between the two materials, its y value is fixed at 0 and we want to solve for its x value. Points A and B are in materials with indices of refraction n_a and n_b, respectively. The total time it takes for the photon to travel from A to B is:

$$t = \frac{n_a}{c}\sqrt{(x-a_1)^2 + a_2^2} + \frac{n_b}{c}\sqrt{(b_1-x)^2 + b_2^2} \tag{A.2}$$

The path the photon takes will minimize t, so I can solve for the path by taking the derivative of t with respect to x and setting it equal to 0:

$$\frac{dt}{dx} = 0 = \frac{n_a}{c}\frac{x-a_1}{\sqrt{(x-a_1)^2 + a_2^2}} - \frac{n_b}{c}\frac{b_1-x}{\sqrt{(b_1-x)^2 + b_2^2}} \tag{A.3}$$

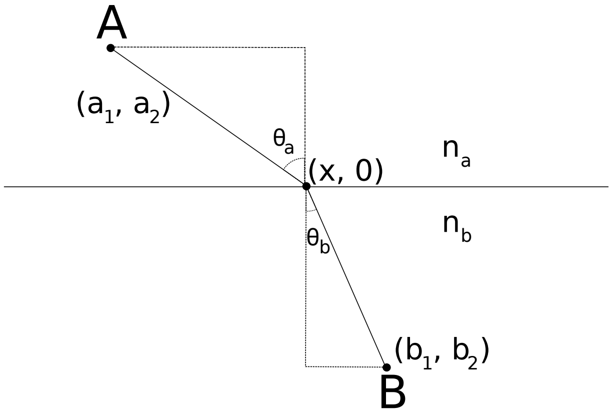

Figure A.1: Diagram of a ray traveling between two points that lie in materials with indices of refraction n_a and n_b. According to Fermat's principle, the photon will take the path that minimzes the travel time. Solving for the minimum travel time reveals Snell's Law, which states that $n_a \sin\theta_a = n_b \sin\theta_b$.

From Figure A.1, $\sin\theta_a$ and $\sin\theta_b$ are:

$$\sin\theta_a = \frac{x - a_1}{\sqrt{(x-a_1)^2 + a_2^2}} \tag{A.4}$$

$$\sin\theta_b = \frac{b_1 - x}{\sqrt{(b_1-x)^2 + b_2^2}} \tag{A.5}$$

The sine terms match two of the terms of the time derivative equation, which now simplifies to:

$$n_a \sin\theta_a = n_b \sin\theta_b \tag{A.6}$$

which is Snell's Law.

Snell's Law can be used to demonstrate the existence of the refractive invariant, which is required for the refraction portion of the ray tracing model. First, consider a path through an atmosphere that does not include refraction, as shown in Figure A.2. At some point P, the photon has an apparent zenith angle z. The minimum tangent altitude the photon will reach is $r\sin z$, where r is the distance of the photon from the center of the planet. This

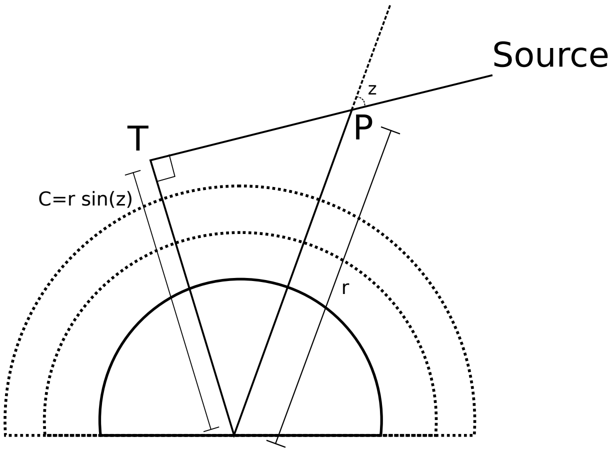

Figure A.2: Ray tracing without refraction. For a photon traveling from some source with a tangent point T, at every point P the tangent altitude can be expressed by $r\sin z$, where r is the distance from P to the center of the planet and z is the local zenith angle.

relationship holds for all values of r and z along the path, so that $r\sin z = C$, where C is a constant.

Now consider an atmosphere with a finite number of layers with different indices of refraction. As the photon travels through the atmosphere, it's path will be refracted as it reaches the boundaries between atmospheric layers. Let the points at which the photon crosses the boundaries be P_1, P_2, ..., at distances from the planetary center r_1, r_2, ... and with indices of refraction in the layers below the boundaries being n_1, n_2, ... The index of refraction outside of the atmosphere is equal to 1 for a vacuum. Let the zenith angles above and below the boundaries be z_{11}, z_{12}, z_{21}, z_{22}.... This scenario is illustrated in Figure A.3. At boundary point P1, when the photon first reaches the atmosphere, applying Snell's Law gives us:

$$\sin z_{11} = n_1 \sin z_{12} \tag{A.7}$$

Multiplying by r_1:

$$r_1 \sin z_{11} = r_1 n_1 \sin z_{12} \tag{A.8}$$

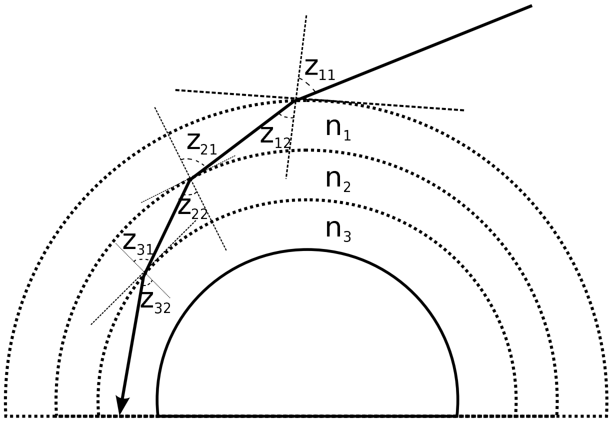

Figure A.3: Ray tracing with refraction. In an atmosphere with three layers with indices of refraction n_1, n_2, and n_3, there are 3 refractions as the photon passes through to the bottom layer of the atmosphere. After each refraction, $nr\sin z$ is constant. This quantity is known as the refractive invariant.

$r_1 \sin z_{11}$ is equal to a constant C, as shown above. So we're left with

$$r_1 n_1 \sin z_{12} = C \tag{A.9}$$

At boundary point P2, a similar application of Snell's Law and multiplying by r_2 results in:

$$n_1 \sin z_{21} = n_2 \sin z_{22} \tag{A.10}$$

$$r_2 n_1 \sin z_{21} = r_2 n_2 \sin z_{22} \tag{A.11}$$

Based on the principle that $r \sin z$ is constant along any straight line path,

$$r_2 \sin z_{21} = r_1 \sin z_{12} \tag{A.12}$$

Substituting this back into Equation A.11:

$$r_1 n_1 \sin z_{12} = r_2 n_2 \sin z_{22} \tag{A.13}$$

$$C = r_2 n_2 \sin z_{22} = r_1 n_1 \sin z_{12} \tag{A.14}$$

This shows that the quantity $r_i n_i \sin z_{i,2}$ is constant for any layer i for each refractive path. Hence it is called the refractive invariant. The pattern shown above for two applications of Snell's Law can be repeated ad infinitum to show that this relationship holds for the entire path.

Knowing that $rn \sin z$ is constant I can now derive the equations that govern refraction in a planetary atmosphere. The geometry of the path is shown in Figure A.4. The calculation of refractive paths is done as a path integral, as this choice of parameter removes any singularities in the calculation (van der Werf, 2008). The variables of interest are the altitude h, the zenith angle z and its complement β, the polar angle ϕ, and the path length s, which is the integration variable. From the geometry described in Figure A.4, using basic trigonometry the differential change in h assuming a small $d\phi$ is:

$$dh = \sin\beta ds = \cos z ds \tag{A.15}$$

To determine the change in ϕ, start with $\sin d\phi$:

$$\sin d\phi = \frac{\sqrt{ds^2 - dh^2}}{R_0 + h} \tag{A.16}$$

$$\sin d\phi = \frac{ds\sqrt{1 - \sin\beta^2}}{R_0 + h} \tag{A.17}$$

$$\sin d\phi = \frac{ds\cos\beta}{R_0 + h} = \frac{ds\sin z}{R_0 + h} \tag{A.18}$$

For an infinitesimally small change in path length, $d\phi$ is small and under the small angle approximation for sine:

$$d\phi = \frac{\cos\beta}{R_0 + h} ds = \frac{\sin z}{R_0 + h} ds \tag{A.19}$$

The last equation needed is for β. In the absence of refraction, the slope of the photon path with respect to the planetary center would be constant and equal to $\tan(\pi/2$ - z - $\phi)$, or $\tan(\beta$ - $\phi)$. For a constant slope, $d\beta = d\phi$. However, refraction will change the slope of the photon path by introducing a curvature term in the equation for $d\beta$. Mathematically,

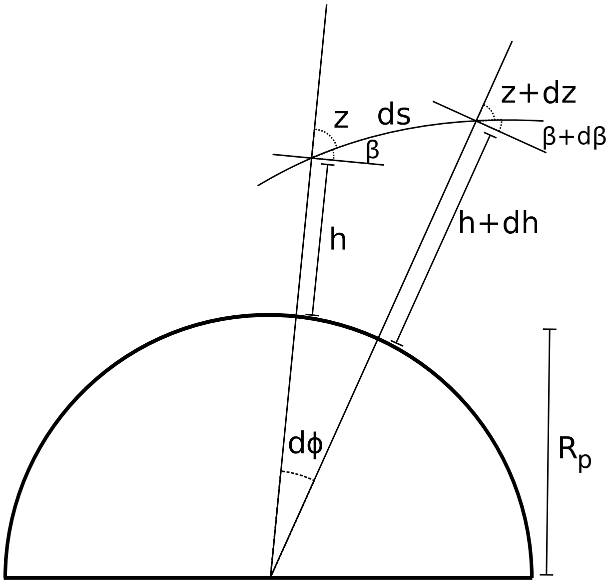

Figure A.4: Ray segment along a refractive path with physical quantities labeled. The polar angle is ϕ, R_p is the planetary radius. *h* is the altitude above the surface, *z* is the local zenith angle and β is it complement. At each step in the ray tracing model, I calculate changes in ϕ, *h*, and β as the path is refracted.

curvature is the change in the slope of the tangent line of a curve, and is written as $\frac{1}{r}$. The complete expression for $d\beta$ is then:

$$d\beta = \left(\frac{\cos\beta}{R_0+h} + \frac{1}{r}\right) ds \tag{A.20}$$

Lastly, it is useful to track an additional variable, ε, which is $d\beta - d\phi$ and is the cumulative effect of refraction on the ray's path.

$$d\varepsilon = d\beta - d\phi = \frac{1}{r} ds \tag{A.21}$$

The curvature term can be derived from the refractive invariant, $nr\sin z$, or $n(R_0 + h)\cos\beta$ when written in terms of R_0, h and β. The derivative of the refractive invariant with respect to the path length can be used to find an expression for the curvature:

$$\frac{d}{ds}(n(R_0+h)\cos\beta) = 0 \tag{A.22}$$

$$\frac{dn}{ds}(R_0+h)\cos\beta + n\frac{dh}{ds}\cos\beta - n(R_0+h)\sin\beta\frac{d\beta}{ds} = 0 \tag{A.23}$$

$\frac{dn}{ds}$ can be written in terms of $\frac{dn}{dh}$ times $\frac{dh}{ds}$, of which the latter is known. The derivative $\frac{d\beta}{ds}$ is also known, so Equation A.23 now becomes:

$$\frac{dn}{dh}\sin\beta(R_0+h)\cos\beta + n\sin\beta\cos\beta - n(R_0+h)\sin\beta(\frac{\cos\beta}{(R_0+h)} + \frac{1}{r}) = 0 \tag{A.24}$$

$$\frac{dn}{dh}\sin\beta(R_0+h)\cos\beta + n\sin\beta\cos\beta - n\sin\beta\cos\beta = n(R_0+h)\frac{1}{r}\sin\beta \tag{A.25}$$

$$\frac{dn}{dh}\sin\beta(R_0+h)\cos\beta = n(R_0+h)\frac{1}{r}\sin\beta \tag{A.26}$$

$$\frac{1}{r} = \frac{1}{n}\frac{dn}{dh}\cos\beta \tag{A.27}$$